



THE HONG KONG
POLYTECHNIC UNIVERSITY

香港理工大學

Pao Yue-kong Library

包玉剛圖書館

Copyright Undertaking

This thesis is protected by copyright, with all rights reserved.

By reading and using the thesis, the reader understands and agrees to the following terms:

1. The reader will abide by the rules and legal ordinances governing copyright regarding the use of the thesis.
2. The reader will use the thesis for the purpose of research or private study only and not for distribution or further reproduction or any other purpose.
3. The reader agrees to indemnify and hold the University harmless from and against any loss, damage, cost, liability or expenses arising from copyright infringement or unauthorized usage.

IMPORTANT

If you have reasons to believe that any materials in this thesis are deemed not suitable to be distributed in this form, or a copyright owner having difficulty with the material being included in our database, please contact lbsys@polyu.edu.hk providing details. The Library will look into your claim and consider taking remedial action upon receipt of the written requests.

**ROOM TEMPERATURE METHANE GAS
SENSING PROPERTIES BASED ON
GRAPHENE RELATED MATERIALS**

LAM KING CHEONG

Ph.D

THE HONG KONG POLYTECHNIC UNIVERSITY

2018

THE HONG KONG POLYTECHNIC UNIVERSITY
DEPARTMENT OF MECHANICAL ENGINEERING

ROOM TEMPERATURE METHANE GAS
SENSING PROPERTIES BASED ON
GRAPHENE RELATED MATERIALS

LAM KING CHEONG

**A thesis submitted in partial fulfilment of the requirements for the
degree of Doctor of Philosophy**

May 2017

CERTIFICATE OF ORIGINALITY

I hereby declare that this thesis is my own work and that, to the best of my knowledge and belief, it reproduces no material previously published or written, nor material that has been accepted for the award of any other degree or diploma, except where due acknowledgement has been made in the text.



Lam King Cheong

May 2017

Abstract

Tin dioxide (SnO_2) is non-toxic, low cost, n-typed with wide band-gap ($E_g = 3.6$ eV) semi-conductor, have been reported to have high sensitivity and fast response to a number of gases due to the oxygen vacancies on surface after annealing which serves as active sites for gaseous interaction. One dimensional metal oxide nanofibers are promising material in gas sensing due to the high surface area and porosity, which is most efficient in transducing gaseous interactions to electrical signal by directional carrier transport. However, metal oxide gas sensors have drawbacks such as high operating temperature and high power consumption. To improve the conductivity of metal oxides, additive materials such as reduced graphene oxide (RGO) have recently been explored for their advantages of high sensitivity, fast response and good conductivity in gas sensing. The hybridisation of RGO with metal oxides such as SnO_2 has been reported to greatly increase the gas sensitivity by p-n junction effect at much lower operating temperatures.

However most operating temperatures of the sensors reported were still higher than room temperature, hence there is still large potential in developing room temperature gas sensing materials with high sensitivity. The objective of this thesis is to investigate room temperature methane gas sensors based on graphene related materials fabricated by drop-drying and electrospinning methods.

The first room temperature methane gas sensor was fabricated by a facile drop-drying method from chemical synthesis which incorporate tin dioxide with graphene oxide in situ reduced by four different reducing agents such as

D-glucose, sodium borohydride, L-ascorbic acid and hydrazine hydrate. It was found that the reducing power of the reducing agents were in ascending order of D-glucose, sodium borohydride, L-ascorbic acid and hydrazine hydrate.

It was found that the methane gas sensitivities of RGO reduced by glucose and ascorbic acid were higher than those by sodium borohydride and hydrazine hydrate due to the residues of glucose/glucono delta-lactone and dehydroascorbic acid, respectively, on the RGO surface, which enlarged the space charge layer and thus improved the response.

The resistances of all the heterostructures with SnO₂ increased due to p-n junction effect. It was found that the sensitivities of the heterostructures of RGO by ascorbic acid and glucose with SnO₂ were the two highest among. The sensitivity of the heterostructure of RGO by ascorbic acid with SnO₂ was found the highest of 76% at 10000 ppm methane concentration at room temperature. The sensitivity of this sensor was not saturated and increased up to 241% at 80000 ppm.

The sensitivity of the heterostructure of RGO by ascorbic acid with SnO₂ was higher than that by glucose which could be due to the synergistic effect between dehydroascorbic acid and SnO₂ deduced from density functional theory calculations. The synergistic effect between dehydroascorbic acid and SnO₂ could be due to the greater charge transfer induced via orbital hybridisation at the carbonyl groups of dehydroascorbic acid, and the more favourable adsorption site atop the in-plane oxygen on SnO₂ surface.

The second room temperature methane gas sensor was fabricated by a less facile electrospinning method to produce PVA/SnO₂/GO nanofiber, and followed by carbonization under N₂ at different temperatures. The optimal concentration of the pure PVA precursor solution was found at 5 wt% in order to produce PVA nanofibers of uniform and beadless structure with small diameter.

PVA/SnO₂/GO nanofibers with different GO concentrations were successfully fabricated at 5 wt% PVA concentration by electrospinning. The nanofibers were uniform, smooth and beadless with smaller diameters as GO content increased. The formation of thinner fiber with more GO content indicating the effect of conductivity was more significant than viscosity with more GO content.

The resistances of the composite nanofiber of PVA/SnO₂/GO were successfully decreased by increasing carbonization temperature and GO content while retaining high sensitivity towards methane measured at room temperature. Increasing carbonization temperature would increase relative amount of conductive amorphous carbon produced after carbonization which decreases resistance. While increasing the content of the comparatively more conductive GO would also decrease resistance.

The sensitivities of the composite nanofiber of PVA/SnO₂/GO without GO content was determined the lowest which could be due to the thin-skinned layer of amorphous carbon which cover the surface of the core-shell nanofiber structure as the carbon skin layer had shielded SnO₂ from contacting with gases for interaction

and also minimized the p-n junction effect by decreasing the contact boundary between the p-typed amorphous carbon and the n-typed SnO₂.

The addition of GO in the composite nanofiber completely changed the core-shell structure to porous structures which benefit gaseous interaction by increasing the p-n junction effect and decreasing the shielding effect from the amorphous carbon layer. The sensitivity of the composite nanofiber PVA/SnO₂/GO with GO content of 5 wt% with respect to PVA in precursor solution was found to have the highest sensitivity of 60.5% at carbonization temperature of 550°C towards methane of 1%. The gas sensor was not saturated at high concentration of methane from 6000-10000 ppm which is useful in application of high concentration environment.

Publications Arising from the Thesis

I. Refereed Journals

1. K.C. Lam, B.L. Huang, S.-Q. Shi, "*Room-temperature methane gas sensing properties based on in situ reduced graphene oxide incorporated with tin dioxide*", J. Mater. Chem. A., **5**, 11131-11142 (2017).
2. K.C. Lam, K.S. Lo, W.W.F. Leung, S.-Q. Shi, "*Room-temperature methane sensing with carbonization of Poly(vinyl) alcohol/Tin dioxide/Graphene oxide nanofiber by electrospinning*", Sensors & Actuators: B. Chemical, under review.

II. Conference Papers

1. K.C. Lam, S.Q. Shi, *Methane gas sensor based on L-ascorbic acid-reduced graphene oxide incorporated with tin oxide*, at International Conference GM-2016 "Graphene and related Materials: Properties and Applications", Paestum (SA), Italy, May 23-27, 2016.
2. K.C. Lam, B.L. Huang, S.Q. Shi, *Room temperature methane gas sensor based on in-situ reduced graphene oxide incorporated with tin dioxide*, at The 21st Annual Conference of HKSTAM 2017, The 13th Jiangsu – Hong Kong Forum on Mechanics and Its Application, Hong Kong SAR, April 8-9, 2017.

III. Patents

1. K.C. Lam, B.L. Huang, S.Q. Shi, "*Room temperature methane gas sensor*" was filed to US Provisional Patent and Trademark Office on August 15, 2017 (Application No. 62545964).

Acknowledgements

First of all, I would like to express my most sincere thanks to my chief-supervisor, Prof. Shi San Qiang, who brought me to this interesting and promising research field. Without his valuable guidance, insightful suggestions, encouragement, and patience, this work would not be completed.

I would also like to express my sincere thanks to Dr. Bolong Huang of ABCT department, for his valuable guidance, advices and discussions in this study.

I would like to acknowledge with gratitude the financial support of The Hong Kong Polytechnic University for a PhD scholarship and a research project (1-99QP).

I would like to thank Dr. Curtis Ng and Mr. Benny Leung for their great help in laboratory works. Also, I would like to thank all my friends, Mr. Kenneth Lo, Dr. Liu Yang, Ms. Yolanda Li, Mr. Stephen Sun, Mr. Austin Jemeno and others who gave me selfless and great help during those years.

Table of Contents

Certificate of Originality	I
Abstract	II
Publications Arising from the Thesis	VI
Acknowledgements	VII
Table of Contents	VIII
List of Figures	XIII
List of Tables	XVIII
CHAPTER 1 INTRODUCTION	1
1.1 Background	1
1.2 Methodologies	6
1.3 Thesis outline	7
References	9
CHAPTER 2 LITERATURE REVIEW	14
2.1 Synthesis and characterization of Graphene	14
2.1.1 Synthesis and characterization of graphene by top-down approach	15
2.1.1.1 Synthesis and characterization of graphene oxide (GO)	16
2.1.1.2 Synthesis and characterization of reduced graphene oxide (RGO)	19
2.1.1.2.1 Reduction methods	20
2.1.1.2.1.1 Thermal reduction	20
2.1.1.2.1.2 Microwave and photo reduction	21
2.1.1.2.1.3 Chemical reduction	21
2.1.1.2.1.4 Electrochemical reduction	23

2.1.1.2.1.5	Solvothermal reduction	23
2.1.1.2.1.6	Multistep reduction	24
2.1.1.2.2	Reduction mechanism	24
2.1.1.2.2.1	Reduction with defects repaired	25
2.1.1.2.2.2	Reduction with defects formed	26
2.1.1.2.3	Dispersibility of RGO	26
2.1.1.2.4	Characterization of RGO by top-down approach	27
2.1.2	Synthesis and characterization of graphene by bottom-up approach	29
2.1.2.1	Synthesis of graphene by bottom-up approach	29
2.2	Synthesis and characterization of tin dioxide	31
2.2.1	Synthesize of tin dioxide	31
2.2.1.1	Sol-gel method	32
2.2.1.2	Hydrothermal process	32
2.2.1.3	Chemical vapor deposition (CVD)	33
2.2.1.4	Physical vapor deposition (PVD)	33
2.2.1.5	Electrospinning	34
2.2.2	Characterization of tin dioxide	35
2.3	Synthesis of heterostructure of graphene and tin dioxide	37
2.4	Electrospinning	39
2.4.1	Background	39
2.4.2	Fiber formation process	42
2.4.2.1	Jet initiation	43
2.4.2.2	Bending instability	44
2.4.3	Fiber morphology control and parameters	47
2.4.3.1	Applied voltage	47
2.4.3.2	Nozzle-collector distance	48
2.4.3.3	Relative humidity	49
2.4.3.4	Solution concentration	49
2.4.3.5	Solution conductivity	49
2.4.3.6	Volatility of solvent	50
2.5	Gas sensing mechanism	50
2.5.1	Formation of Space charge layer	50
2.5.2	Factors affecting sensitivity	53
2.5.2.1	Grain boundary barrier effect (Schottky barrier effect)	53
2.5.2.2	p-n junction effect	54
2.5.2.3	Grain size effect	54

2.5.2.4	Additive effect	56
2.5.2.4.1	Chemical additive effect	56
2.5.2.4.2	Electronic additive effect	57
2.5.2.5	Porosity effect	58
2.5.2.5.1	Intrinsic void	58
2.5.2.5.2	Chemical pore	58
2.5.2.5.3	Thermal crack/pore	58
2.6	Summary	59
	References	61
CHAPTER 3	SYNTHESIS AND CHARACTERIZATION OF HETEROSTRUCTURES OF REDUCED GRAPHENE OXIDE/TIN DIOXIDE BY DROP-DRYING METHOD	78
3.1	Introduction	78
3.2	Experimental	81
3.2.1	Materials	81
3.2.2	Preparation of GO	82
3.2.3	Preparation of RGO-SnO ₂	83
3.3	Results and discussion	84
3.3.1	SEM analysis	84
3.3.2	Raman analysis	86
3.3.3	FTIR analysis	88
3.3.4	XRD analysis	90
3.4	Conclusion	92
	References	94
CHAPTER 4	SYNTHESIS AND CHARACTERIZATION OF POLYVINYL ALCOHOL/TIN DIOXIDE/GRAPHENE OXIDE NANOFIBER BY ELECTROSPINNING METHOD	99
4.1	Introduction	99
4.2	Experimental	103
4.2.1	Materials	103
4.2.2	Preparation of PVA nanofiber	104
4.2.3	Preparation of GO	104

4.2.4	Preparation of PVA/SnO ₂ /GO nanofiber	105
4.3	Results and discussion	106
4.3.1	SEM analysis of pure PVA nanofiber	106
4.3.2	SEM analysis of PVA/SnO ₂ /GO composite nanofiber	110
4.3.3	TEM analysis	113
4.3.4	TGA analysis	116
4.3.5	Raman analysis	118
4.3.6	XRD analysis	120
4.3.7	FTIR analysis	122
4.4	Conclusion	123
	References	127
 CHAPTER 5 GAS SENSING MEASUREMENT		 138
5.1	Gas testing chamber	138
5.2	Gas sensing measurement	140
5.2.1	Methane gas sensor by drop-drying method	140
5.2.1.1	Resistance measurement	140
5.2.1.2	Sensitivity measurement	142
5.2.2	Methane gas sensor by electrospinning method	148
5.2.2.1	Resistance measurement	148
5.2.2.2	Sensitivity measurement	150
5.3	Conclusion	158
	References	161
 CHAPTER 6 DENSITY FUNCTIONAL THEORY CALCULATIONS (DFT+U) ANALYSIS		 166
6.1	Introduction	166
6.2	DHA-SnO ₂ system	170
6.2.1	Model 1 (dissociated adsorption)	171
6.2.2	Model 2 (undissociated adsorption)	173
6.3	Glucose-SnO ₂ system	175
6.3.1	Model 3 (un-oxidised glucose-SnO ₂)	176
6.3.2	Model 4 (glucono delta-lactone-SnO ₂)	178
6.4	Conclusion	179
	References	182

CHAPTER 7	CONCLUSIONS	185
7.1	Methane gas sensor from drop-drying method	185
7.2	Methane gas sensor from electrospinning method	187
7.3	Future works and improvements	188
7.3.1	Improvement of understanding the sensing mechanisms	189
7.3.2	Improvement of sensitivity with other additives	190
7.3.3	Improvement by using different fabrication methods	191
7.3.4	Improvement of selectivity for different gases	192

List of Figures

Figure 2.1	GO structure with oxygen functional groups.	17
Figure 2.2	Reduction of GO to RGO.	19
Figure 2.3	Typical structures of RGO showing the distortion and void space within the graphitic plane.	20
Figure 2.4	Raman spectrum of graphite, GO and RGO.	28
Figure 2.5	Processes involved during graphene synthesis in a CVD process.	30
Figure 2.6	The operation of electrospinning.	40
Figure 2.7	The operation of needless electrospinning.	42
Figure 2.8	Images taken around the period of jet initiation.	44
Figure 2.9	Bending instability during electrospinning.	46
Figure 2.10	Spiral loop formation by curvature in the jet.	46
Figure 2.11	The multiple field technique.	48
Figure 2.12	A schematic diagram showing the receptor function, transducer function and the space charge layer (electron depleted layer).	51
Figure 2.13	A schematic diagram showing the formation of space charge layer upon oxygen adsorption on SnO ₂ surface.	52
Figure 2.14	A schematic diagram showing the conductive path of charge carriers in bulk region varied due to different Schottky barriers at boundaries.	54

Figure 2.15	A schematic diagram of the grain size effect.	56
Figure 3.1	Schematic diagram for preparation of RGO-SnO ₂ composite.	83
Figure 3.2	SEM images of homostructures (a) GO, (b) R(G), (c) R(B), (d) R(A), (e) R(H) and heterostructures (f) GO-SnO ₂ , (g) R(G)-SnO ₂ , (h) R(B)-SnO ₂ , (i) R(A)-SnO ₂ and (j) R(H)-SnO ₂ .	86
Figure 3.3	Raman spectra of GO, R(G), R(B), R(A) and R(H).	87
Figure 3.4	FTIR spectra of GO, R(G), R(B), R(A) and R(H).	89
Figure 3.5	XRD spectra of (a) GO, R(G), R(B), R(A) and R(H); (b) GO- SnO ₂ , R(G)- SnO ₂ , R(B)- SnO ₂ , R(A)- SnO ₂ and R(H)- SnO ₂ .	92
Figure 4.1	Schematic diagram of needleless electrospinning.	102
Figure 4.2	SEM images of (a) 2wt%, (b) 3wt%, (c) 4wt%, (d) 5wt%, (e) 6wt%, (f) 7wt% and (g) 8wt% PVA.	108
Figure 4.3	Fiber diameter distribution of (a) 2wt%, (b) 3wt%, (c) 4wt%, (d) 5wt%, (e) 6wt%, (f) 7wt% and (g) 8wt% PVA .	109
Figure 4.4	SEM images of (a) N0, (b) N1, (c) N2, (d) N2 (before carbonization), (e) N3 and (f) N4.	112
Figure 4.5	Fiber diameter distribution of (a) N0, (b) N1, (c) N2, (d) N2 (before carbonization), (e) N3 and (f) N4.	113
Figure 4.6	Representative TEM images of (a) N0, (b) N1 and (c) N3. HRTEM images of (d) N0, (e) N1 and (f) N3.	116
Figure 4.7	(a) TGA and (b) DTG spectra of the composite nanofibers.	118

Figure 4.8	Raman spectra of the composite nanofibers of PVA/SnO ₂ /GO with different GO contents (a) before carbonization and (b) after carbonization.	120
Figure 4.9	XRD spectra of the composite nanofibers of PVA/SnO ₂ /GO before and after carbonization at different temperatures.	122
Figure 4.10	FTIR spectra of the composite nanofibers of PVA/SnO ₂ /GO before and after carbonization at different temperatures.	123
Figure 5.1	A schematic diagram of a prototype electrodes design.	139
Figure 5.2	A schematic diagram of a homemade gas testing chamber and equipment setup.	139
Figure 5.3	Resistance of GO, R(G), R(B), R(A), R(H) and their heterostructures with SnO ₂ at room temperature.	142
Figure 5.4	Sensitivity of GO, R(G), R(B), R(A), R(H) and their heterostructures with SnO ₂ towards methane (1%) at room temperature.	144
Figure 5.5	Sensitivity against time plot of (a) GO, R(G), R(B), R(A) and R(H); (b) GO-SnO ₂ , R(G)-SnO ₂ , R(B)-SnO ₂ , R(A)-SnO ₂ and R(H)-SnO ₂ towards methane (1%) at room temperature.	146
Figure 5.6	(a) Resistance against time plot at different methane concentration and (b) sensitivity against methane concentration of R(A)-SnO ₂	147
Figure 5.7	Resistances of the composite nanofibers PVA/SnO ₂ /GO with different GO contents carbonized at different temperatures.	149

Figure 5.8	Sensitivities of the composite nanofibers PVA/SnO ₂ /GO with different GO contents carbonized at different temperatures towards methane (1%).	151
Figure 5.9	Representative resistance against time plots of the composite nanofibers PVA/SnO ₂ /GO at different carbonization temperatures towards methane (1%).	152
Figure 5.10	Representative resistance against time plots of the composite nanofibers PVA/SnO ₂ /GO with different GO contents at carbonization temperature of 550°C towards methane (1%).	153
Figure 5.11	Sensitivities of the composite nanofibers PVA/SnO ₂ /GO with different GO contents after carbonization at 550 °C towards methane (1%).	155
Figure 5.12	Sensitivities of the composite nanofiber of N3 after carbonization at 550 °C towards methane at different concentrations.	156
Figure 5.13	Resistance against time plot of the composite nanofiber of N3 after carbonization at 550 °C towards methane at different concentrations.	157
Figure 6.1	(110) plane of SnO ₂ surface.	168
Figure 6.2	Dehydroascorbic acid (DHA) and delocalisation of the three carbonyl groups with an electron donor.	171
Figure 6.3	(a) HOMO (blue), (b) LUMO (green) and (c) DOS plot of DHA in model 1 (dissociated adsorption).	173
Figure 6.4	(a) HOMO (blue), (b) LUMO (green) and (c) DOS plot of DHA in model 2 (undissociated adsorption)	175

Figure 6.5	(a) D-glucose (ring form) and (b) glucono delta lactone	176
Figure 6.6	(a) HOMO (blue), (b) LUMO (green) and (c) DOS plot of glucose in model 3 (un-oxidised glucose-SnO ₂).	177
Figure 6.7	(a) HOMO (blue), (b) LUMO (green) and (c) DOS plot of glucono delta lactone in model 4 (glucono delta lactone-SnO ₂).	179

List of Tables

Table 2.1	A comparison of chemical and electronic additive effects towards a gas analyte.	57
Table 5.1	Recent reports on room temperature methane sensors.	158

Chapter 1

Introduction

1.1 Background

Gas sensors are chemical sensors that consist of active chemicals which transduce the response to specific gases into modulations of signals such as resistance change, frequency change and voltage change. Since there are harmful, inflammable and toxic gases in atmosphere which are hazardous to human health, safety, environmental preservation and medical diagnosis. Therefore gas sensors development is certainly an appealing market in great demand. Among the various harmful or inflammable gases, methane gas is the main component of fuel gas which is odourless, highly volatile and explosive, which receives much attention in pipeline accidents. The low explosion limit of methane has been determined as 4.7 % in air [1]. Most works of methane gas sensors are mostly based on semiconductor metal oxide which operates at high temperatures (150-350 °C) [2–6]. Hence efforts are continually made to develop methane gas sensor at low temperature which is also the aim of this project.

Gas sensors could be divided into four types: (1) Semiconductor type which transduces the response of chemical interactions between the gas analytes with the sensing chemicals such as semiconductors to resistance change. (2) Optical type which uses a light emitting source, a filter, a photodetector and a

fiber optic coated with a sensing element which transduces the response in light of the gas analytes to detected emission of fluorescence or phosphorescence. (3) Electrochemical type which consists of a sensing electrode, a reference electrode and a counter electrode in an electrolyte. The gas analytes adsorbed on the sensing electrode cause the change in potential difference. (4) Acoustic wave type which consists of a sensitive film attached on a piezoelectric substrate which responds the gas analytes to give a specific Rayleigh resonant frequency. Among all types of gas sensors, semiconducting type is intensively studied and market appealing due to its low cost, simple and facile manufacturing, fast response and stability which is also the focus of this project.

The first semiconductor gas sensor was reported in 1962 by Seiyama et al. [7] to detect inflammable gases by zinc oxide. In the same year, Taguchi employed tin dioxide gas sensor with a gas leakage alarm system to apply for a patent [8]. Later, the semiconductor gas sensor emerged as an effective and reliable safety device in prevention of gaseous accidents. Among metal oxide semiconductor gas sensors, tin dioxide gas sensor has been intensively studied due to the advantages of high gas sensitivity, stability and fast response. Tin dioxide (SnO_2) is non-toxic, low cost, easily accessible, n-typed with wide band-gap ($E_g = 3.6 \text{ eV}$) semi-conductor, have been reported to have high sensitivity and fast response to a number of gases due to the oxygen vacancies on surface after annealing which serves as active sites for gaseous interaction [9–13]. Besides metal oxide thin film sensing materials, one dimensional metal oxide nanofibers are promising material in gas sensing due to high surface area and porosity, which is most efficient in transducing gaseous interactions to electrical signal by

directional carrier transport [4,5,14–17].

Indeed, oxygens on surface of tin dioxide are easily annealed to oxygen molecules which leave electrons at these vacancy sites at high temperature. The electrons released at these oxygen vacancy sites would then contribute to bulk negative charge carriers which increase conductivity. However, oxygens in air would later adsorb on these oxygen vacancy sites as O^- and capture electrons on surface to form a space charge layer. At this stage, a receptor function in terms of the sensitive space charge layer of the tin dioxide gas sensor is established. When gas analytes in environment interact with those adsorbed oxygens on surface to change the space charge layer, a transducer function is established in terms of electrical signal such as resistance or conductivity measurement. Sensitivity of gas sensor to a particular gas is generally defined as the percentage change of resistance of the sensor under the flow of the gas at a certain concentration to pure air.

However, metal oxide gas sensor has numerous drawbacks such as insulating at room temperature which requires high operating temperature and power consumption. The high operating temperature also results in short life and shift in resistance. However owing to the simplicity and low cost in manufacturing process, metal oxide semiconductor is still under development for improving the sensitivities, selectivity and response time by incorporation with additive materials. On the other hand, the substitutes for metal oxides such as polymers, carbon nanotubes and graphene have been searched for their advantages of room temperature operation, higher sensitivity and faster response.

Besides metal oxides, polymer gas sensors are also gaining importance due to their low cost, easy processing and room temperature operation [18,19]. However, the structures of polymers are usually porous such that the high surface-to-volume ratio results in larger sensitivity, but the response time is very slow. Moreover the polymer structures are far less stable than metal oxide such that structure refining at high temperature is difficult. Carbon nanotube (CNT) was discovered in 1993 by Ijima [20]. Both the single and multi-walled structures have been intensively studied due to the extremely high specific surface area ($\sim 1000 \text{ m}^2/\text{g}$), good thermal and electric conductivities and mechanical strength. The high surface area is attributed to the long thin hollow cores, which renders it a promising material for gas sensing of high sensitivity and room temperature operation [21,22]. However, the long thin hollow structures also limit the escape of the gases which results in slow response and incomplete recovery signal.

On the other hand, as a frontier material, graphene is a highly interested research topic in material science as applications of solar cell and gas sensor due to its superior electrochemical properties [23–30]. Graphene is a two-dimensional and single-layer sheet of sp^2 hybridized carbon atoms with zero bandgap energy which demonstrates superior electrical conductance. It demonstrates ambipolar effect and hence the type of charge carriers can be tuned by adjusting gate voltage. Besides, graphene can be considered as an ideal electrode material because of its large surface area, superior electrical conductance and fast electron transfer rate. The specific surface area of graphene is $\sim 2600 \text{ m}^2/\text{g}$ which is even larger (about twice) than that of CNT. Moreover, the widely open structure renders it to have a faster response than CNT.

However, the pristine form of graphene has been reported to have low gas sensitivity due to the lack of energetically favourable sites, such as defects or functional groups, to interact with gases [30]. Recently, graphene derivative such as graphene oxide (GO) and reduced graphene oxide (RGO) have become an interesting research with significant potential in applications of sensors, batteries and biomedical engineering due to the oxygen functional groups [25,27,28,31–33]. GO consists of few layers of graphite oxide which is usually produced by chemical oxidation of graphite with exfoliation process [34]. Meanwhile, the abundant oxygen functional groups of hydroxyl, epoxy, carbonyl and carboxylic groups on basal planes or edges could serve as active sites for chemical interactions in gas sensors. However, the defects and functional groups on GO also destroy the continuity of the ballistic transport of charge carriers on the graphitic plane [35]. Hence, GO is poorly conductive, which restrains its electrical applications. The reduction of GO to RGO could be achieved by thermal reduction, microwave and UV irradiation, laser interference reduction and chemical reduction [33], which are been reported to improve conductivity without significant loss of sensitivity by the residual oxygenated groups after reduction.

The hybridisation of RGO with metal oxides such as SnO₂ has been reported to greatly increase the gas sensitivity by p-n junction effect at much lower operating temperatures [5,6,36–39] due to the high conductivity of RGO. However most operating temperatures of the sensors reported were still higher than room temperature, hence there is still large potential in developing room temperature gas sensing materials with high sensitivity. In addition to inducing good responsiveness, the addition of SnO₂ is far more economical than the use of

noble transition metals such as Pd or Pt [40,4,16]. Hence, sensors based on heterostructures of RGO and SnO₂ are expected to have stronger and faster gas responses.

1.2 Methodologies

As mentioned above, metal oxides gas sensors have high operating temperature which makes it awkward to be a portable and miniaturized electronic device. Hence the aim of this project is to synthesize graphene based gas sensors which could operate at room temperature with high sensitivities and fast response to methane. The fabrications of the gas sensors were achieved by drop-drying and electrospinning method as discussed below.

Firstly GO was prepared using the modified Hummers method [34] which oxidized graphite flake by concentrated sulphuric acid, sodium nitrate and potassium permanganate. The GO obtained was reduced in situ by four reducing agents such as D-glucose, sodium borohydride, L-ascorbic acid and hydrazine hydrate in separate experiments. The RGOs obtained were mixed with SnO₂ and a small amount of polyvinyl alcohol (PVA) was added as a binder and homogeniser to disperse the SnO₂ crystallites uniformly. Gas sensors were fabricated by drop-drying the composite suspensions onto glass substrates with gentle heating to evaporate the solvent.

Secondly, a composite nanofiber of PVA/SnO₂/GO gas sensor was synthesized by electrospinning method. The precursor solution was prepared by

mixing polyvinyl alcohol (PVA), $\text{SnCl}_2 \cdot 2\text{H}_2\text{O}$ and GO with different concentrations. Then the precursor solution was electrospun to composite nanofibers using roller electrospinning unit. The as-spun composite nanofibers of different GO concentrations were carbonized in N_2 at different temperatures. The gas sensors fabricated respectively by drop-drying and electrospinning method were characterized by SEM, TEM, TGA, Raman, XRD and FTIR. While the electrical resistance and sensitivity measurements were carried out inside a home-made gas testing chamber.

1.3 Thesis outline

The thesis delivers the research program of the investigation of room temperature methane gas sensing properties based on graphene related materials with a brief theoretical calculation of the sensing mechanisms. The thesis also includes the relevant literature review during the course of study. The thesis outline could be organized as follows:

In chapter 2, the previous works of gas sensing materials, fabrication methods and sensing mechanisms were discussed.

In chapter 3, the synthesis and characterization of thick film gas sensors of the homostructures of GO and RGO, and their heterostructures with SnO_2 by drop-drying method were discussed. In addition, the compositions of the RGOs and reducing powers of different reducing agents used were compared.

In chapter 4, the synthesis and characterization of PVA/ SnO_2 /GO

composite nanofibers gas sensors with different GO contents by electrospinning method were discussed. In addition, the structures and compositions of the composite nanofibers with different GO contents and carbonization temperatures were compared.

In chapter 5, the electrical resistance and sensitivity measurements of the gas sensors of RGO-SnO₂ by drop-drying method and the composite nanofiber of PVA/SnO₂/GO by electrospinning method were discussed. In addition, the relationship between resistance and gas sensitivity with reduction levels and compositions in the gas sensors of RGO-SnO₂ by drop-drying method were presented. While the relationship between resistance and gas sensitivity with different GO contents and carbonization temperatures in the composite nanofiber of PVA/SnO₂/GO by electrospinning method were also discussed.

In chapter 6, a brief discussion on theoretical calculations by density functional theory of the sensing mechanisms of the gas sensor of RGO-SnO₂ by drop-drying method is presented.

In chapter 7, the main findings and contributions of the thesis were concluded.

References:

- [1] A. Takahashi, Y. Urano, K. Tokuhashi, H. Nagai, M. Kaise, S. Kondo, Fusing ignition of various metal wires for explosion limits measurement of methane/air mixture, *J. Loss Prev. Process Ind.* 11 (1998) 353–360.
- [2] Z.K. Horastani, S.M. Sayedi, M.H. Sheikhi, Effect of single wall carbon nanotube additive on electrical conductivity and methane sensitivity of SnO₂, *Sens. Actuators B Chem.* 202 (2014) 461–468.
- [3] Q. Qi, T. Zhang, L. Liu, X. Zheng, Synthesis and toluene sensing properties of SnO₂ nanofibers, *Sens. Actuators B Chem.* 137 (2009) 471–475.
doi:10.1016/j.snb.2008.11.042.
- [4] J.-K. Choi, I.-S. Hwang, S.-J. Kim, J.-S. Park, S.-S. Park, U. Jeong, Y.C. Kang, J.-H. Lee, Design of selective gas sensors using electrospun Pd-doped SnO₂ hollow nanofibers, *Sens. Actuators B Chem.* 150 (2010) 191–199.
doi:10.1016/j.snb.2010.07.013.
- [5] S.-J. Choi, B.-H. Jang, S.-J. Lee, B.K. Min, A. Rothschild, I.-D. Kim, Selective Detection of Acetone and Hydrogen Sulfide for the Diagnosis of Diabetes and Halitosis Using SnO₂ Nanofibers Functionalized with Reduced Graphene Oxide Nanosheets, *ACS Appl. Mater. Interfaces.* 6 (2014) 2588–2597. doi:10.1021/am405088q.
- [6] R.K. Mishra, S.B. Upadhyay, A. Kushwaha, T.-H. Kim, G. Murali, R. Verma, M. Srivastava, J. Singh, P.P. Sahay, S. Hee Lee, SnO₂ quantum dots decorated on RGO: a superior sensitive, selective and reproducible performance for a H₂ and LPG sensor, *Nanoscale.* 7 (2015) 11971–11979.
doi:10.1039/C5NR02837J.

-
- [7] T. Seiyama, S. Kagawa, Study on a Detector for Gaseous Components Using Semiconductive Thin Films., *Anal. Chem.* 38 (1966) 1069–1073.
- [8] N. Taguchi, Published patent application in Japan, S37-47677 Oct. (1962).
- [9] J.F. McAleer, P.T. Moseley, J.O. Norris, D.E. Williams, Tin dioxide gas sensors. Part 1.—Aspects of the surface chemistry revealed by electrical conductance variations, *J. Chem. Soc. Faraday Trans. 1 Phys. Chem. Condens. Phases.* 83 (1987) 1323–1346.
- [10] J.F. McAleer, P.T. Moseley, J.O. Norris, D.E. Williams, B.C. Tofield, Tin dioxide gas sensors. Part 2.—The role of surface additives, *J. Chem. Soc. Faraday Trans. 1 Phys. Chem. Condens. Phases.* 84 (1988) 441–457.
- [11] J. Watson, The tin oxide gas sensor and its applications, *Sens. Actuators.* 5 (1984) 29–42.
- [12] J. Oviedo, M.J. Gillan, Energetics and structure of stoichiometric SnO₂ surfaces studied by first-principles calculations, *Surf. Sci.* 463 (2000) 93–101.
- [13] V. Lantto, T.T. Rantala, T.S. Rantala, Atomistic understanding of semiconductor gas sensors, *J. Eur. Ceram. Soc.* 21 (2001) 1961–1965.
- [14] J.-H. Lee, A. Katoch, S.-W. Choi, J.-H. Kim, H.W. Kim, S.S. Kim, Extraordinary improvement of gas-sensing performances in SnO₂ nanofibers due to creation of local p–n heterojunctions by loading reduced graphene oxide nanosheets, *ACS Appl. Mater. Interfaces.* 7 (2015) 3101–3109.
- [15] Y. Zhang, X. He, J. Li, Z. Miao, F. Huang, Fabrication and ethanol-sensing properties of micro gas sensor based on electrospun SnO₂ nanofibers, *Sens. Actuators B Chem.* 132 (2008) 67–73. doi:10.1016/j.snb.2008.01.006.

- [16] D.-J. Yang, I. Kamienchick, D.Y. Youn, A. Rothschild, I.-D. Kim, Ultrasensitive and Highly Selective Gas Sensors Based on Electrospun SnO₂ Nanofibers Modified by Pd Loading, *Adv. Funct. Mater.* 20 (2010) 4258–4264. doi:10.1002/adfm.201001251.
- [17] Z. Wang, Z. Li, J. Sun, H. Zhang, W. Wang, W. Zheng, C. Wang, Improved Hydrogen Monitoring Properties Based on p-NiO/n-SnO₂ Heterojunction Composite Nanofibers, *J. Phys. Chem. C.* 114 (2010) 6100–6105. doi:10.1021/jp9100202.
- [18] B. Adhikari, S. Majumdar, Polymers in sensor applications, *Prog. Polym. Sci.* 29 (2004) 699–766.
- [19] U. Lange, N.V. Roznyatovskaya, V.M. Mirsky, Conducting polymers in chemical sensors and arrays, *Anal. Chim. Acta.* 614 (2008) 1–26.
- [20] S. Iijima, T. Ichihashi, Single-shell carbon nanotubes of 1-nm diameter, *Nature.* 363 (1993) 603–605.
- [21] C.B. Jacobs, M.J. Peairs, B.J. Venton, Review: Carbon nanotube based electrochemical sensors for biomolecules, *Anal. Chim. Acta.* 662 (2010) 105–127.
- [22] H. Qian, E.S. Greenhalgh, M.S. Shaffer, A. Bismarck, Carbon nanotube-based hierarchical composites: a review, *J. Mater. Chem.* 20 (2010) 4751–4762.
- [23] M.J. Allen, V.C. Tung, R.B. Kaner, Honeycomb Carbon: A Review of Graphene, *Chem. Rev.* 110 (2010) 132–145. doi:10.1021/cr900070d.
- [24] E.V. Iski, E.N. Yitamben, L. Gao, N.P. Guisinger, Graphene at the Atomic-Scale: Synthesis, Characterization, and Modification, *Adv. Funct. Mater.* 23 (2013) 2554–2564. doi:10.1002/adfm.201203421.

- [25] D. Chen, H. Zhang, Y. Liu, J. Li, Graphene and its derivatives for the development of solar cells, photoelectrochemical, and photocatalytic applications, *Energy Environ. Sci.* 6 (2013) 1362. doi:10.1039/c3ee23586f.
- [26] T. Gan, S. Hu, Electrochemical sensors based on graphene materials, *Microchim. Acta.* 175 (2011) 1.
- [27] Y. Shao, J. Wang, H. Wu, J. Liu, I.A. Aksay, Y. Lin, Graphene Based Electrochemical Sensors and Biosensors: A Review, *Electroanalysis.* 22 (2010) 1027–1036. doi:10.1002/elan.200900571.
- [28] S. Wu, Q. He, C. Tan, Y. Wang, H. Zhang, Graphene-Based Electrochemical Sensors, *Small.* 9 (2013) 1160–1172.
- [29] F. Yavari, N. Koratkar, Graphene-Based Chemical Sensors, *J. Phys. Chem. Lett.* 3 (2012) 1746–1753. doi:10.1021/jz300358t.
- [30] W. Yuan, G. Shi, Graphene-based gas sensors, *J. Mater. Chem. A.* 1 (2013) 10078. doi:10.1039/c3ta11774j.
- [31] D. Chen, H. Feng, J. Li, Graphene oxide: preparation, functionalization, and electrochemical applications, *Chem. Rev.* 112 (2012) 6027–6053.
- [32] S. Prezioso, F. Perrozzi, L. Giancaterini, C. Cantalini, E. Treossi, V. Palermo, M. Nardone, S. Santucci, L. Ottaviano, Graphene Oxide as a Practical Solution to High Sensitivity Gas Sensing, *J. Phys. Chem. C.* 117 (2013) 10683–10690. doi:10.1021/jp3085759.
- [33] S. Pei, H.-M. Cheng, The reduction of graphene oxide, *Carbon.* 50 (2012) 3210–3228.
- [34] W.S. Hummers Jr, R.E. Offeman, Preparation of graphitic oxide, *J. Am. Chem. Soc.* 80 (1958) 1339–1339.

- [35] F. Schedin, A.K. Geim, S.V. Morozov, E.W. Hill, P. Blake, M.I. Katsnelson, K.S. Novoselov, Detection of individual gas molecules adsorbed on graphene, *Nat. Mater.* 6 (2007) 652–655.
- [36] J.-H. Lee, A. Katoch, S.-W. Choi, J.-H. Kim, H.W. Kim, S.S. Kim, Extraordinary Improvement of Gas-Sensing Performances in SnO₂ Nanofibers Due to Creation of Local *p* – *n* Heterojunctions by Loading Reduced Graphene Oxide Nanosheets, *ACS Appl. Mater. Interfaces.* 7 (2015) 3101–3109. doi:10.1021/am5071656.
- [37] P.A. Russo, N. Donato, S.G. Leonardi, S. Baek, D.E. Conte, G. Neri, N. Pinna, Room-Temperature Hydrogen Sensing with Heteronanostructures Based on Reduced Graphene Oxide and Tin Oxide, *Angew. Chem. Int. Ed.* 51 (2012) 11053–11057. doi:10.1002/anie.201204373.
- [38] Z. Wang, C. Zhao, T. Han, Y. Zhang, S. Liu, T. Fei, G. Lu, T. Zhang, High-performance reduced graphene oxide-based room-temperature NO₂ sensors: A combined surface modification of SnO₂ nanoparticles and nitrogen doping approach, *Sens. Actuators B Chem.* 242 (2017) 269–279. doi:10.1016/j.snb.2016.10.101.
- [39] S. Mao, S. Cui, G. Lu, K. Yu, Z. Wen, J. Chen, Tuning gas-sensing properties of reduced graphene oxide using tin oxide nanocrystals, *J. Mater. Chem.* 22 (2012) 11009. doi:10.1039/c2jm30378g.
- [40] N. Yamazoe, New approaches for improving semiconductor gas sensors, *Sens. Actuators B Chem.* 5 (1991) 7–19.

Chapter 2

Literature review

2.1 Synthesis and characterization of Graphene

Graphene is a two-dimensional (2D) and single-layer sheet of sp^2 hybridized carbon atoms. It is a semiconductor with zero bandgap energy which demonstrates super electrical conductance, large surface area and fast electron transfer rate [1–7]. Few layers or monolayer graphene is mostly synthesized by the top-down approach or the bottom-up approach. The top-down approach starts from chemical oxidation of graphene to graphene oxide (GO) by some strong oxidizing agents such as potassium permanganate or sodium dichromate, and finally reduced to reduced graphene oxide (RGO) by reducing agents such as hydrazine or ammonium hydroxide [8,9]. While the bottom-up approach is usually achieved by chemical vapor deposition (CVD) such that graphene is directly grown on a catalyst substrate copper or nickel by passing carbon source gases like methane (CH_4) or carbon dioxide (CO_2) at a specific temperature and gas flow rate. The as-prepared graphene would be transferred to a substrate such as glass by etching the back side of the catalyst copper or nickel [10–13].

In comparison, the top-down approach has the advantages of low cost,

simple and easy accessibility over the bottom-up approach. However, it has been well demonstrated that redox reactions in top-down approach could introduce defects such as oxygen functional groups, voids and distortion of the basal network [8]. Moreover, the agglomerations of the reduced form RGO result in bulk and large grains due to the strong delocalized π - π interactions between the stacked layers prevent the formation of few-layered graphene. In contrast, CVD method in bottom-up approach could synthesize few layers of clean and pristine graphene network without defects [1,3,13]. However there are problems for CVD method such as the difficulties in transferring the graphene from the metal catalyst onto a substrate due to the delicacy of the few-layered graphene which is easily disrupted or damaged from the transfer process. Moreover, defects would be introduced such as impurities or ruptures of the network would be resulted from the transfer process. Both methods have advantages and disadvantages, and it is interesting to investigate the properties of graphene from both methods in gas sensing behaviours.

2.1.1 Synthesis and characterization of graphene by top-down approach

It has been mentioned above that the synthesis of graphene by top-down approach has the disadvantages of introducing defects such as oxygen functional groups, voids and distortion in the basal network. However it is reported that the pristine graphene has low sensitivities to gas sensing due to the lack of high energy binding sites such as functional groups in metal oxides or polymers [7]. Therefore, it is expected that the defects of graphene synthesized by top-down approach could be

a merit in gas sensing on the contrary.

2.1.1.1 Synthesis and characterization of graphene oxide (GO)

The oxidation derivative of graphene is graphene oxide (GO), which is a popular starting material in hybridization of graphene with metal oxides or polymers due to its good dispersibility in both water and organic solvents. GO is mostly obtained from the modified Hummers' method [14], in which small graphite flakes (~1000 mesh) are firstly mixed with concentrated sulfuric acid and sodium nitrate with magnetic stirring for one hour. Then adding strong oxidizing agent potassium permanganate to the suspension with vigorous stirring for 2 hour. During stirring, small bubbles evolve and effervescence occurs. After that the suspension becomes a slurry paste which is brownish in color. Then D.I. water is added slowly to the paste, exothermic reaction occurs and temperature increases to about 90°C. Keep stirring and further adding icy water to the hot suspension until temperature drops to 30°C and no effervescence is observed. Finally, the suspension is treated with hydrogen peroxide to remove the excess permanganate ion. The adding of sulfuric acid and sodium nitrate to graphite is to introduce some oxygen functional groups in the basal plane of graphite such that the oxygen functional groups between the graphitic layers could induce electrostatic repulsions that the adjacent layers move apart and water molecules could be dissolved in between. Therefore the graphite flake expands to expanded graphite (EG) so that the permanganate ions could penetrate through the layers and oxidize the EG to GO. Moreover, the introduction of oxygen functional groups in the basal plane would destroy the delocalized sp^2 bonds which decrease

the π - π interactions and decrease aggregations. This is the reason why GO could be well dispersed in water or organic solvents.

In order to explain the structure of GO, Lerf et al. [15] proposed a model based on ^{13}C and ^1H NMR. It is believed that the oxygen functional groups added on the graphitic layer would be in terms of the hydroxyl group (-OH), epoxy group (-C-O-C-) and the carboxyl group (-COOH). The hydroxyl and epoxy groups would be added either inside the basal plane or at the edge. While the carboxyl group would be added at the edge of the plane. Later Szabo et al. [16] proposed one more oxygen functional group the carbonyl group (C=O) exists either inside the basal plane or at the edge. Recently Wei et al. [17] propose the five- and six-membered ring lactols were added on the edge of the basal plane. The model of the structure of GO could be depicted in Figure 2.1.

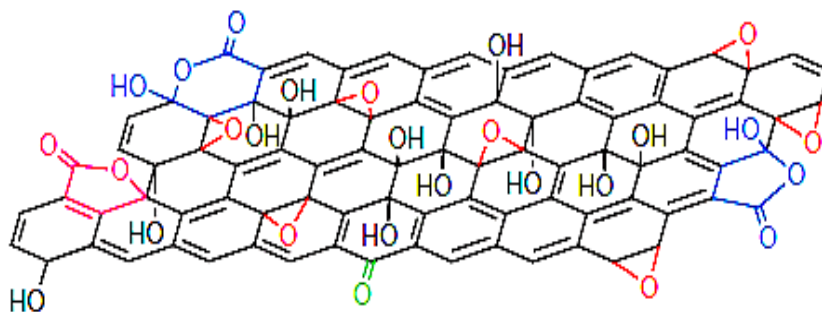


Figure 2.1 GO structure with oxygen functional groups. (Figure from reference [17])

As GO has very high resistance due to the p-type oxygen functional groups in the graphitic layers which draw electrons from the polyaromatic network towards the oxygen which lowers the conductivity. GO usually has resistances in the range of 10^6 to $10^9 \Omega$ which renders it difficult to be resistive measurable in

gas sensing. Incorporation of metal particles or amino acids are hoped to improve conductivity and sensitivity. Metal particles could donate electrons back to the graphitic network which increases conductivity. On the other hand, it also provides high energy binding sites with the gas analytes which increases sensitivity. On the other hand, GO incorporating with amino acids could introduce the alkyl groups or nitrogen functional groups like (=NH) or (-NH₂) which are electron donating such that electrons could be returned back to the graphitic network so as to increase conductivity. Sensitivity also increases due to the incorporation of nitrogen functional groups which provide high energy binding sites for the gases to be tested. Actually reports on gas sensors based on pure GO or hybridization of GO with additive materials are rare due to the insulating property of GO [15,18]. Therefore GO is usually accepted as the precursor material for further synthesis to its next derivative, the reduced graphene oxide (RGO) which has a far better conductivity to be measured. Actually, there are many efforts of gas sensors reported on reducing the p-type GO to the less p-type RGO. However, the oxidation level of GO is nonstoichiometric which depends on methods and chemical reagents, hence it is interesting to directly synthesize a partially oxidized graphene oxide (GO) which has a measurable conductivity with good dispersibility in most solvents and water. Moreover, partially reduced GO has much more oxygen functional groups than RGO so that it is believed to have higher sensitivity than RGO due to the high energy binding sites of the oxygen functional groups.

2.1.1.2 Synthesis and characterization of reduced graphene oxide (RGO)

Since GO has very high resistance that is usually out of measurable range, it is mostly reduced to RGO to obtain a better conductivity for sensor applications. Nowadays, it is well documented on reduction of GO [8], they are (1) Thermal reduction [19,20], (2) Microwave [21,22] and photoreduction [23,24], (3) Chemical reduction [25–31], (4) Electrochemical reduction [32–35], (5) Solvothermal reduction [36–38] and (6) Multistep reduction [39–42]. The models of the structure of RGO could be depicted in Figure 2.2 and 2.3.

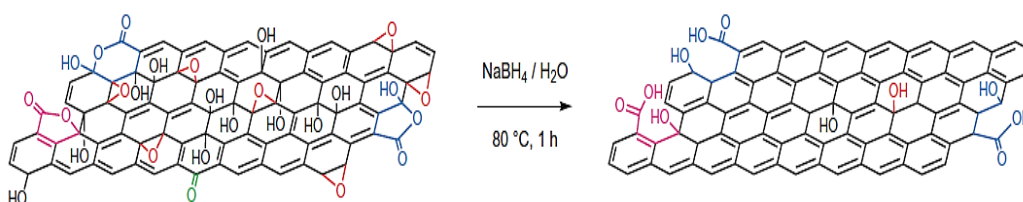
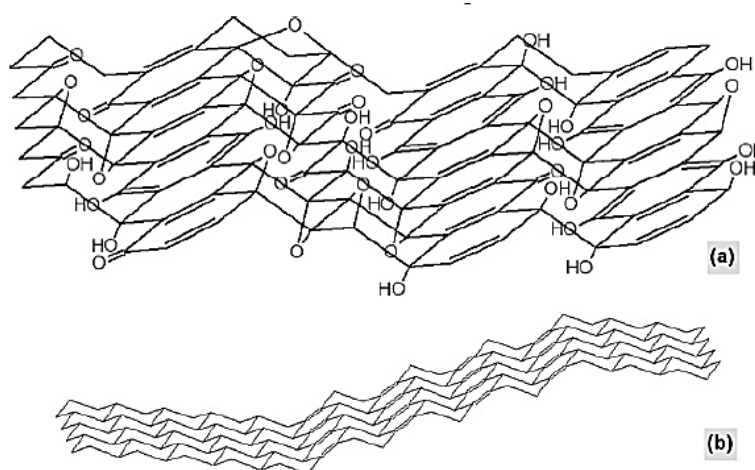


Figure 2.2 Reduction of GO to RGO. (Figure from reference [17])



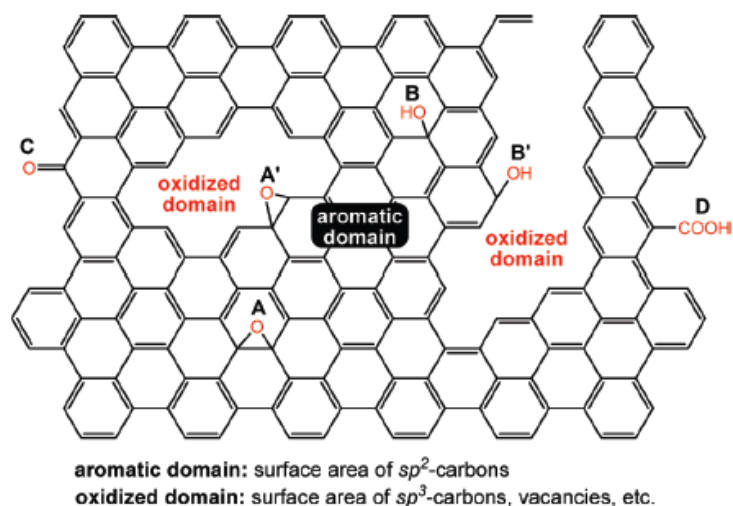


Figure 2.3 Typical structures of RGO showing the distortion and void space within the graphitic plane. (Figure from reference [16,43])

2.1.1.2.1 Reduction methods

2.1.1.2.1.1 Thermal reduction

When GO is dried and prepared in the form of solid (film or powder), it is reduced by heat treatment known as thermal annealing. In the process, GO is heated to high temperature in the range from 300°C to 1000°C [19,20]. During the process, it would be exfoliated such that H_2O , CO or CO_2 gases would be evolved. The mechanisms behind the annealing is to create a large pressure difference of the evolved gases between the stacked layers and the surrounding atmospheric pressure. Exfoliation occurs when the interlayer pressure is large enough to push against the stacked layers and overcome the weak van der waals force that connects the stacked layers. The exfoliated sheets of GO after the annealing process are known as reduced graphene oxide (RGO). Therefore the annealing process not only exfoliates but also reduces the oxygen functional groups of the GO. However, the exfoliated graphene sheets produced by this method are usually

small and wrinkled due to the decomposition of the oxygen functional groups. The decomposition process also removes the carbon atoms to give off CO or CO₂ gases which split and distort the graphene sheets and left the defective sites with vacancies [8,17]. In thermal annealing, the level of reduction depends on temperature and atmospheric pressure [8,43]. Actually a higher temperature with vacuum environment would result in a higher level of reduction. Therefore, thermal annealing is easy to control and fast to process, so this method is used in the mass production of graphene.

2.1.1.2.1.2 Microwave and photo reduction

Besides thermal heating, some other heating methods have been tried to reduce GO including microwave irradiation [21,22] and photo-irradiation [23,24]. Microwave irradiation has the advantages of heating the sample uniformly and rapidly over thermal annealing. Besides microwave, other photo source have been used to reduce GO in flash reduction and laser irradiation. Flash reduction is carried out by exposing the GO film to a camera xenon lamp at a close distance (2mm to 1 cm) [23]. Higher level of reduction would be resulted from a closer distance of illumination. The flash irradiation could provide 9 times the thermal energy needed to heat the GO film has been reported. Further increasing the irradiation power and intensity could improve the level of reduction as the case in laser irradiation [24].

2.1.1.2.1.3 Chemical reduction

The above two methods are solid phase reduction. If GO dispersed in solvent is reduced by chemical reducing agents at room temperature or at elevated

temperature is known as chemical reduction. There are numerous reducing agents have been reported on the reduction of GO such as hydrazine (N_2H_4) [30,31], sodium borohydride (NaBH_4) [29], ascorbic acid (vitamin C) [25], hydroiodic acid (HI) [28,44], benzyl alcohol [45] and sodium hydroxide (NaOH) [46]. Among all of them, reducing agents like hydrazine, sodium borohydride and ascorbic acid are strong to reduce GO and a high level of reduction could be obtained. While alcohols and sodium hydroxide are mild reducing agents on GO. However, another problem concerning RGO is the dispersibility in the solvents. Hydrazine is strong and fast in reducing GO, but the final reduced form RGO results in heavy agglomeration that hardly disperse in most solvents. Moreover, hydrazine is toxic and pungent smell evolved when processing. Sodium borohydrate (NaBH_4) is also a strong reducing agent but it is found that the reducing rate is too low that results from the fact that NaBH_4 is slowly hydrolyzed by water. Recently ascorbic acid (vitamin C) has been reported as a strong reducing agent for GO which is non-toxic and environmental friendly with better dispersibility than hydrazine, and faster reducing rate than NaBH_4 . On the other hand, Pei et al. [28] and Moon et al. [44] has reported that hydroiodic acid (HI) is another strong reducing agent for GO. The reduction of GO by HI results in an even higher reduction level than hydrazine with better tensile strength. Chemical reduction of GO is simple, easy and low-cost which is popular in industrial and research application, but there are some problems like the incorporation of impurities like nitrogen functional group hydrazone when reducing GO by hydrazine [30,31]. Moreover, the reduction by chemical reagents cannot completely recover the pristine graphene structure. For example, most reducing agents could easily remove the carbonyl and carboxyl groups, but the tertiary

alcohol group is hardly removed. Therefore multistep reduction would be carried out to further remove the tertiary alcohol group.

2.1.1.2.1.4 Electrochemical reduction

Electrochemical reduction of GO can be carried out by connecting a prepared GO film with an inert electrode opposite in a buffer solution. Reduction of GO occurs by electron exchange between GO and the electrode by cyclic voltammetric scanning of the electrochemical cell in the range of 0 to -1 V [32–35]. The reduction level and conductivity of GO by electrochemical reduction could be as high as using chemical reagents like hydrazine or ascorbic acid. Moreover, the advantage of electrochemical reduction over chemical reduction is making no use of dangerous chemicals such as hydrazine and hydroiodic acid. Besides, the reduction level by this method could be accurately and easily controlled by the voltage of the cell.

2.1.1.2.1.5 Solvothermal reduction

Solvothermal process involves the use of a solvent to react with the GO confined in a sealed stainless-steel autoclave at a supercritical condition [36–38,47]. Solvent such as N, N-dimethylformamide has been reported to reduce GO with the addition of a small amount of hydrazine at 180 °C for 12 h [47], the reduction level is as high as the chemical reduction but the conductivity of the RGO is lower. Another solvent which is well known for synthesis of nanoparticle of metal oxide is supercritical water (SCW). The use of water as solvent in solvothermal process is known as hydrothermal process. It has been found that using SCW to reduce GO results in good reduction level especially in removing the reluctant

alcohol group to alkene.

2.1.1.2.1.6 Multistep reduction

The reduction processes mentioned above are carried in one step. To further improve the reduction level and conductivity of RGO, multistep reduction involves the combination of the above reduction methods has been proposed. The usual multistep reduction includes chemical reduction followed by thermal annealing [39–42]. It is found that using hydrazine to reduce GO followed by 200 °C thermal annealing has better conductivity and reduction level than one step annealing at 550 °C. As most chemical reducing reagents could not remove all the oxygen functional groups, therefore it is reported that using NaBH₄, then treating with concentrated sulfuric acid and finally annealed in Ar/H₂ at 1100 °C results in much higher reduction level and conductivity than any one step reduction method.

2.1.1.2.2 Reduction mechanism

We know that GO has extensive incorporation with oxygen functional groups either in the basal plane or at the edge. Through reduction methods like chemical reducing and thermal annealing, most of the oxygen functional groups are removed. However, there are few efforts reported on the reduction mechanism of GO due to the complexity of the chemical reactions and the progressively structural change of the RGO during the process. Generally, the defects of RGO could be categorized into two types, i.e. the vacancies and distortion from the sp² planar structure of the pristine graphene. Furthermore, the defects of RGO would either become repaired or worse than before during the reduction process. The

reduction level could be examined through the C/O ratio (the area ratio of C(1s) peak to O(1s) peak) by XPS measurement. If most oxygen functional groups are eliminated, then O(1s) peak area would be decreased and the C/O ratio would be increased. Hence an increase of C/O ratio implies a better reduction level. While the defect level could be examined through the I_D/I_G ratio (the intensity ratio of D band (1353 cm^{-1}) to G band (1580 cm^{-1})) in Raman spectroscopy [48]. Actually, D band corresponds to the vibrations of the disordered out-of-plane sp^3 carbon atoms while G band corresponds to the vibrations of the planar sp^2 carbon atoms. Therefore in graphene characterization, D band refers to defect while G band refers to the pristine graphene (G) network. Keep this rule in mind, I_D/I_G ratio decreases implies defective sites are lower. However, due to the lack of efficient and direct means to monitor the reduction mechanism, most of the efforts are based on computer simulations and few efforts are based on experimental analysis.

2.1.1.2.2.1 Reduction with defects repaired

By density functional theory (DFT) calculation, it has been found that annealing GO at 700°C , all carboxyl, epoxy and hydroxyl groups could be removed in vacuum, while the carbonyl groups could only be removed at temperature as high as 1730°C [8,17]. Moreover, the hydroxyl groups inside the basal plane have lower binding energy that is unstable and more prone to be eliminated than the hydroxyl groups at the edge which is more stable. Another explanation is based on chemical reduction, the epoxy group is much easier to be reduced than the hydroxyl group by hydrazine [8,49]. Based on the explanations, the epoxide opening reacts with hydrazine to form an aminoaziridine, then thermal elimination

of the di-imide to form the sp^2 alkene. The structural distortion of GO is caused by the cross linked structure by the out-of-plane sp^3 cyclohexane chair with the planar sp^2 honeycomb hexagons. Since all carbon atoms bonded with the oxygen functional groups are tetrahedral sp^3 , the removal of these functional groups could recover the planar sp^2 hexagonal structure. Besides, reduce GO by chemical vapor deposition (CVD) is well known for its synthesis of pristine graphene thin film structure. By CVD, it has been found that the defective vacancies in GO could be repaired by using ethylene vapor as carbon source.

2.1.1.2.2 Reduction with defects formed

By simulation methods, it has been found that crowded functional groups close to each other could interact with each other to benefit desorption [8,17,43]. While the removal of carbon atoms are more probable to occur at sites where hydroxyl and epoxy groups are at close proximity. Similarly, if GO with a higher oxygen content is reduced by thermal annealing, it is more likely to form defects with vacancies due to removal of carbon atoms as CO or CO₂ gases evolved [7,8].

2.1.1.2.3 Dispersibility of RGO

After the reduction process, most of the oxygen functional groups are eliminated, only some of them still remain inside the basal plane or at the edge. The oxygen functional groups are repelling from each other and account for the ease of exfoliation of GO such that the repelling force is large enough to overcome the weak van der waals force and the strong π - π interlayer interactions. If most of the oxygen functional groups are eliminated, then the strong π - π interlayer interactions dominate and agglomeration of the stacked layers of RGO occurs

which also lowers the dispersibility in most solvents. Hence in comparing the dispersibility, GO is good in most solvents but RGO is very selective on the solvent used. It has been found that dimethyl formamide (DMF) is good in dispersing RGO, and the resulting colloidal suspension could be easily dispersed in various polar solvent like water, dimethylsulphoxide, N, N-dimethylacetamide and N-methylpyrrolidone. However it precipitated quickly in non-polar solvents such as cyclohexanone, CH₃CN, tetrahydrofuran, ethanol, toluene, o-dichlorobenzene, and dichloromethane [44]. Furthermore, it is reported that reducing GO by sodium hydroxide or potassium hydroxide produce good reduction level with good dispersibility of the reduced GO in alkaline condition [46]. It suggests that the alkaline condition could benefit the repelling interlayer force which lowers the effect of agglomeration. Recently, PVP is also reported as a good dispersing solving for RGO [50].

2.1.1.2.4 Characterization of RGO by top-down approach

The differentiation of graphite, GO and RGO would be typically analyzed by Raman spectrum as shown Figure 2.4. The characteristic vibrational D and G bands at $\sim 1,360$ and $\sim 1,590$ cm⁻¹, respectively could be observed in GO and RGO. However, in graphite, only G band could be observed. The D band, representing a 'defect' signal, typically corresponds to the breathing-mode vibrations of the out-of-plane sp³ carbon. The presence of a D band requires a breaking of the symmetry of the aromatic ring, as occurs in the sp³ chair form of the ring or at edge sites. Hence, pristine graphite does not display this band. The G band, representing a pristine 'graphitic' signal, corresponds to the stretching-mode vibrations of the in-plane sp² carbon. Actually, the intensity ratio of I_D/I_G could be

used to study the reduction level and to differentiate the graphene family. Higher I_D/I_G ratio indicated a higher defect level as observed in RGO case while a lower I_D/I_G ratio indicated a lower defect level as observed in GO. The increase in the D band signal relative to the G band in RGO is due to edge sites around the newly formed multiple sp^2 domains accompanying the removal of oxygen functional groups [9,51,52]. The edge sites around the newly formed sp^2 domains would induce asymmetric breathing-mode vibration which increases D band signal while the formation of multiple sp^2 domains broadens the signal of G band which increases the ratio of I_D/I_G .

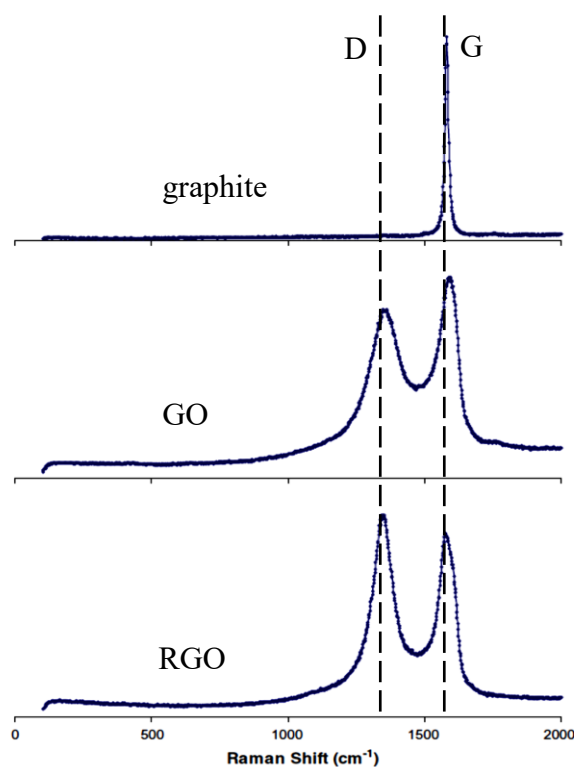


Figure 2.4 Raman spectrum of graphite, GO and RGO. (Figure from reference [9])

2.1.2 Synthesis and characterization of graphene by bottom-up approach

2.1.2.1 Synthesis of graphene by bottom-up approach

The synthesis of graphene from top-down approach inherits the disadvantages of introduction of defects such as impurities, voids and distortion from the planar structure. Moreover the agglomerations of the final reduced form RGO render it difficult to control the thickness or number of layers. Actually, the synthesis of large area with high-quality graphene is very important for the manufacturing of electronic devices and there is no doubt that the bottom-up approach from chemical vapor deposition (CVD) is the promising method for this.

Synthesis of graphene by typical CVD methods are well documented [10–13] and the process is shown in Figure 2.5. Firstly, a metallic catalyst such as copper foil would be loaded into a quartz tube, which would be annealed at very high temperature (~ 1000 °C) in vacuum for degassing. During the process, hydrogen gas would be passed at low rate and pressure to remove the oxide layer on the copper foil. After annealing at 1000 °C for 15 min, a carbon source such as methane gas (CH_4) would be passed to the tube for the growth of graphene on copper foil. Keep hydrogen flow and high temperature (~ 1000 °C) throughout the whole growth process for about 10 min. After the growth process, the as-grown graphene is allowed to cool to room temperature with stop flowing methane gas but still keeping the flow of hydrogen at very low rate until temperature cools down to (600 °C). The as-grown graphene would then be transferred to a glass substrate by spin coating a layer of poly(methyl) methacrylate (PMMA) on

graphene as a protection layer during the transfer process. Then etch the copper foil on the back side by etchants such as iron (III) chloride for 1 h. Finally the colourless thin film of PMMA/graphene would be transferred to a glass substrate carefully. After that, the unwanted layer of PMMA would be stripped away by acetone or chloroform.

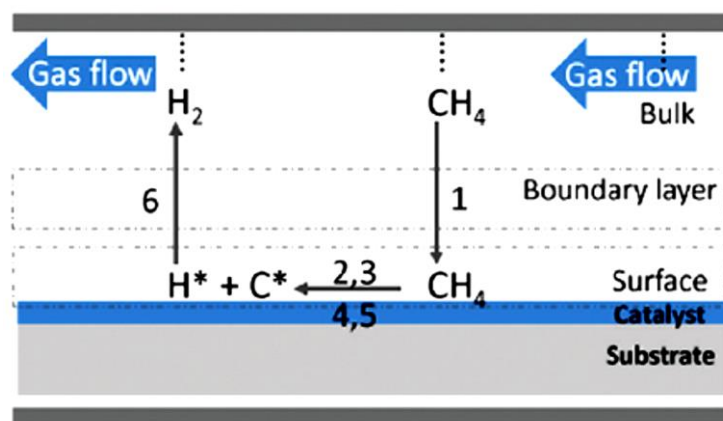


Figure 2.5 Processes involved during graphene synthesis in a CVD process.

(Figure from reference [54])

Actually the growth mechanism of graphene on copper catalyst has been intensively investigated [12,53,54]. When hydrogen and methane gases are flowed into the chamber, the growth mechanism could be processed through a six-step catalytic process: (1) diffusion of the gases through the boundary layer, (2) adsorption of the gases on Cu surface, (3) decomposition of hydrocarbons to form active carbon species, (4) aggregation of the carbon atoms on Cu surface to form graphene lattice, (5) desorption of inactive species (molecular hydrogen) from the surface, and (6) diffusion away of molecular hydrogen from the surface to the gas bulk flow. The catalytic reaction of transition metals helps to reduce the reaction temperature. However, Fe, Co, and Ni are not preferred for graphene growth due

to their higher solubility to carbon as well as the higher capability to decompose methane such that few layers of graphene sheets are not easy to control. Actually, few layers of graphene sheets are easier to control by using Cu substrate. This is due to the lower solubility of carbon (<0.001 %) in Cu which allows the possibility of controlling the number of graphene layers. Diffusion rate and carbon concentration are crucial in controlling the thickness of graphene sheets. The simultaneous flow of methane and hydrogen is due to the fact that hydrogen acts as a cocatalyst in formation of active surface-bounded $\text{CH}_3\cdot$ radical for the growth of graphene. On the other hand, it removes the active hydrogen $\text{H}\cdot$ radical to hydrogen gases which could be desorbed from the surface and diffused out to the bulk flow.

2.2 Synthesis and characterization of tin dioxide

2.2.1 Synthesize of tin dioxide

Metal oxides have attracted much attention in gas sensing due to their simplicity and flexibility in production, low cost, fast response and good structural stability. The transduced signal could be measured by the change of capacitance, resistance, or optical characteristics. Among all of them, tin dioxide (SnO_2) has been extensively studied due to its high sensitivity [55–57] for most gases, non-toxicity, and high dispersion in most solvents. The synthesis of tin dioxide could be achieved by (1) sol-gel method [58–61], (2) hydrothermal process [62–66], (3) chemical vapor deposition (CVD) [67–69], (4) physical vapor deposition (PVD)

[70–73] and (5) electrospinning [74–81].

2.2.1.1 Sol-gel method

The sol-gel method has long been used for synthesis of tin dioxide due to the low cost, simplicity and well controlled processing in production. Firstly hydrated tin chloride ($\text{SnCl}_2 \cdot 2\text{H}_2\text{O}$) is dissolved in organic solvent such as pure ethanol and acetyl acetone for 1h with stirring. Inorganic polymerization follows the hydrolysis and condensation processes of the metal oxide. Then a chemical modifier usually an organic binder such as polyethylene glycol (PEG) is added to the “sol” suspension to further improve the slurry texture. Then the “sol” is dried at room temperature for 24 h. Finally the dried slurry “sol” becomes a “gel” and is further dehydrated at 120 °C for 1 h and then calcination at 600 °C for 3 h to remove the organic solvents and improve the structural stability and grain size.

2.2.1.2 Hydrothermal process

The hydrothermal process is similar to the reduction of GO as mentioned above. Typically, a solution of tin chloride and solvents such as ethanol and distilled water would be mixed with ammonium hydroxide with stirring at room temperature for 1 h. Then the precursor solution would be transferred to a well-sealed stainless steel autoclave and heated to 180 °C for 16 h in a furnace. After that, the precipitate in the solution could be washed with water and ethanol, and then filtered by a 0.22 μm membrane filter. Finally the filtered precipitate would be dried at 120 °C for 1 h and calcined at 600 °C for 3 h to remove the organic

solvents and refine the grain size.

2.2.1.3 Chemical vapor deposition (CVD)

CVD is a more advanced technique to synthesize tin dioxide. Firstly, a cleaned substrate such as glass or silicon wafer is loaded in a quartz tube which is placed in a furnace. The substrate is positioned at a constant temperature zone usually in the middle of the furnace. Tin chloride crystal is heated to melt in a delivery tube which is connected to the inlet of the quartz tube under a constant flow of air. When the desired temperature is reached (~400 – 600 °C), the oxygen carried anhydrous tin chloride vapor is passed into the quartz tube for the growth of tin dioxide on the substrate. While the outlet of the quartz tube is connected to a delivery tube which is dipped in water for the exhaustion of air bubbles formed. Another simpler procedure is similar to the above but to coat the substrate firstly with tin chloride thin film and then directly passed air to the tube when the desired temperature is reached. CVD could synthesize pristine tin dioxide thin film down to several layers which is mostly adopted to produce monocrystalline structure. However monocrystalline structure has lower gas sensitivity than polycrystalline structure due to the lack of grain boundaries barriers. In order to produce polycrystalline metal oxides structures, temperature and vapor flow rate should be varied but it is difficult to optimize these conditions to meet the desired polycrystalline structure.

2.2.1.4 Physical vapor deposition (PVD)

PVD is mostly achieved by sputtering or e-beam evaporation, which is widely used to impregnate additives to the thin film substrate. In sputtering, the source

additive material such as metal catalyst Pd or Pt are sputtered by inert gases such as argon gas to the tin oxide thin film substrate. For the synthesis of tin oxide, the source material could be metal tin which is sputtered on a glass or silicon wafer substrate. Then the tin metal thin film could be thermally annealed at high temperature 800 °C in air ambient to produce tin oxide. The structure of the sputtered material on substrate could be polycrystalline since there would be deflections of sputtered material by inert gases. Due to momentum transfer of the inert gases to the source material, the weight of the inert gas must be comparable to the source material. Therefore argon gas would be used for sputtering heavy source material, and neon gas would be used for light source material. Throughout the whole process, no high temperature is needed to sputter the metal catalyst which is a merit over e-beam evaporator which requires high temperature to thermally emit electrons to strike the source metallic catalyst on substrate.

2.2.1.5 Electrospinning

The methods mentioned above could be used to synthesize nanostructures such as nanospheres, nanoplatelets, nanorods or nanobelts which have small grain size with high surface-to-volume ratio. Among the nanofabrication techniques, electrospinning has demonstrated as a versatile and facile technique to synthesize exceptionally high surface-to-volume ratio 1D nanofiber. The nanofibers formed are uniform and exceptionally long which are cross-linked to form a giant network. Moreover there are many voids or pores between the nanofibers which serve to channel the gases to the inside bulk from surface for gas sensing. Typically, a precursor solution of tin chloride with solvents such as ethanol and DMF is mixed with organic matrix such as PVP, polyvinyl alcohol (PVA) or

polyethylene oxide (PEO) under vigorous stirring at 90 °C for 2 h. Then the precursor solution is loaded to a container with a metallic needle or a rotating wire which is charged to extremely high voltage of 50 kV against a grounded collector substrate such as glass. The solution at the needle mouth or at the rotating wire would be extracted as a long thin fiber out from the solution and accelerated to strike on the grounded substrate by the extreme high voltage. Finally the nanofibers of tin oxide could be calcined to remove the organic solvents or residues.

2.2.2 Characterization of tin dioxide

Tin dioxide also known as stannic oxide, with chemical formula SnO_2 is a rutile structure usually found in cassiterite mineral ore. SnO_2 powder is white, insoluble in water and is usually regarded as an n-type semiconductor [55–57]. After calcination, SnO_2 possess high oxygen vacancies which act as electron donors and therefore making it an n-type semiconductor [82,83]. From X-ray diffraction (XRD) measurement, it could be found that the major peaks are due to the (110), (101) and (100) surface. SnO_2 has been widely used in electrode materials in solar cell, light emitting diodes, and gas sensors due to its non-toxicity, high optical transparency in visible region, wide band-gap energy ($E_g = 3.6$ eV) and high dispersion in most organic solvents. For gas sensing mechanism, the ambient oxygen adsorbed on the tin oxide grains would extract electrons away from the conducting bulk region to the surface due to the oxidizing property of oxygen. Therefore the concentration of the conducting electrons in bulk region reduced and hence the resistance increases.

When tin dioxide is exposed to reducing gases such as H_2 , CH_4 or CO , the bounded electrons near the surface would be injected back to the conducting bulk which decreases the resistance. The situation would be reversed for oxidizing gases such as NO_2 or SO_2 . The bounded electrons would be extracted more away from the conducting bulk region which further increases the resistance for oxidizing gases. Finally the change in the resistance would be modulated as the gas sensitivity. However, it has been found that tin oxide has good sensitivities for many gases including the oxidizing gases such NO_2 , SO_2 and the reducing gases such as H_2 , NH_3 and CH_4 . Hence in order to solve the selectivity problem, surface modification with other metal oxides, polymers, carbon nanotubes (CNT) or graphene has been demonstrated to greatly improve selectivity towards specific gases [75–78,80,84–94] due to the synergistic effects induced from the heterostructures.

However, there are problems associated with metal oxides gas sensors such as the high operating temperature, high power consumption and low dispersibility in most solvents making it non-uniformly distributed in the heterostructures. Since there are low oxygen vacancies after calcination, SnO_2 is insulating at room temperature. Therefore it is promising to incorporate it with conducting materials such as CNT, conducting polymers and graphene. However, CNT has very slow responses due to the long thin hollow structures limiting the escape of gases [85,86,94–96] while conducting polymers are thermally unstable in air at high temperature. On the hand, graphene a 2D material has larger surface-to-volume ratio than CNT and faster response of the gases due to the widely open 2D dimension. The structure is also stable when thermally annealed in air. Hence

it is expected to have the advantages of larger sensitivity and low power consumption of operating at room temperature for the hybridization of graphene and tin oxide. However, there are few efforts reporting on hybridization of graphene with tin dioxide in the application of gas sensor [77,78,88,89,91–93].

2.3 Synthesis of heterostructure of graphene and tin dioxide

It is found that the pristine graphene was seldomly used as the sole material in gas sensing due to the lack of high energy binding sites such as oxygen functional groups as compared with metal oxides or conducting polymers. The delocalized π - π interactions in the graphene basal plane are low energy binding sites such that the adsorbed gases are loosely bounded, so the change of resistance in the gas sensor is not remarkable. Besides, Van der Waals force and π - π interactions between the adjacent layers of graphene are strong enough to aggregate the layers together. Therefore graphene is poorly dispersive in most solvents. The aggregation of graphene would also cause the grain size increase such that the surface to bulk ratio decrease which lowers the sensitivity of gas sensing. Therefore graphene is seldomly used as a sole and a starting material in gas sensor. Usually, graphite is used as a precursor to obtain graphene and then hybridized with metal oxides or polymers to introduce high energy binding sites in gas sensing.

Most of the hybridization methods of graphene and additive materials are

achieved by the in situ chemical method, PVD method or the electrospinning method as mentioned above. Among them, the in situ chemical method has been demonstrated to be simple, easy and low-cost to synthesize small grain-sized heterostructures with high uniformity in distribution. The highly uniform distribution is exceptionally important due to the low dispersing power of reduced graphene oxide (RGO) and metal oxides in most solvents. Simply mixing of these two materials in solvents usually results in large grain size of individual agglomerations which is difficult to distribute uniformly in the suspension. This is due to the fact that RGO has strong agglomeration in most solvents by the strong π - π interlayer stacking force. Hence the metal oxide particles could not disperse into the interlayer space of RGO which results in individual agglomerations in the suspension. Therefore, the in situ synthesis begins the hybridization when the materials are in their precursor forms such as mixing GO and tin chloride, then the reduction of GO and the precipitation of tin oxide process simultaneously in one step by a base solution such as ammonium hydroxide. The advantage of this method is to distribute well the two precursor materials first before producing the final product. The precursor materials GO and tin chloride could be well dispersed and dissolved in acidic solution. Therefore, tin chloride ions could disperse into the GO interlayer first and forming precipitates at the interlayer space which lowers the self-agglomeration effect of the reduced RGO. Song et al. [97] synthesized graphene with SnO₂ by hydrothermal in situ method to test propanal by cataluminescence sensing measurement with high sensitivity and selectivity due to synergistic effect. Mao et al. [88] synthesized a nanocomposite of RGO with SnO₂ by electrostatic force-directed assembly (ESFDA) process to test NO₂ and NH₃. The synergistic effect found to increase the sensitivity to NO₂ but

decrease to NH_3 . Russo et al. [92] synthesized the heterostructure of graphene and SnO_2 by micro-wave assisted method with incorporation of Pt nanoparticles to test hydrogen gas which showed to have larger sensitivities than individual structures. Lee et al. [78] synthesized nanofibers of RGO with SnO_2 by electrospinning which showed a 20 fold increase in NO_2 sensitivity.

2.4 Electrospinning

2.4.1 Background

Electrospinning is a simple and versatile method of producing nanofibers from a precursor solution by applying high electrical voltage. It is widely used in the area of biomedical scaffolds, tissue engineering, filtration medium and batteries [98–102]. The origin of electrospinning can be traced back to 1934 when Formhals [103] firstly patented to produce artificial threads using electric field. In later years he filed another patent to improve his invention by increasing the nozzle-collector distance for better solvent drying process. A typical needle-typed electrospinning unit is illustrated in Figure 2.6.

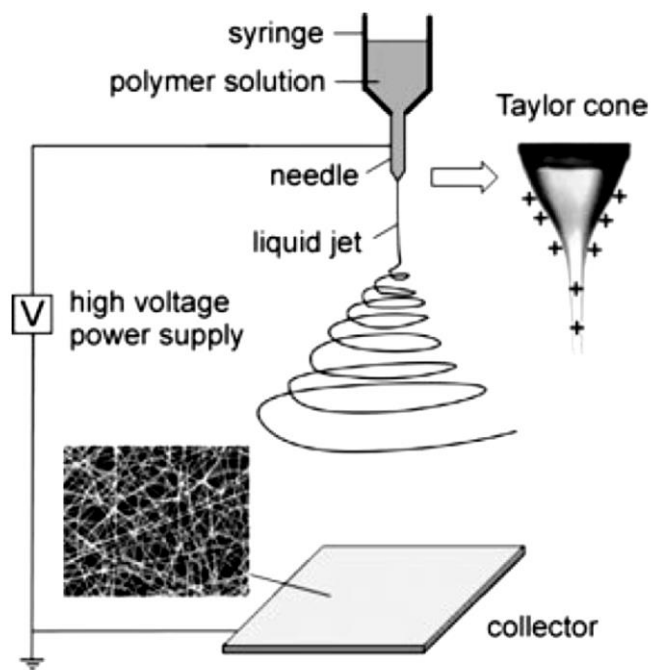


Figure 2.6 The operation of electrospinning. (Figure from reference [98])

In the 1960s, fundamental studies on jet stream formation process were studied by Taylor [104] who found the formation of the conical shape of the precursor droplet at the needle tip in high electric field. The conical shape of the droplet, later known as “Taylor Cone”, is critical to initiate jet streaming at the vertice of the cone for nanofiber formation. In 1971, Baumgarten [105] studied the dependence of fiber diameter on the viscosity of the solution of a polyacrylonitrile/dimethylformamide (PAN/DMF) solution. He reported that the fiber diameter firstly decreased to a minimum value and increased afterwards with increasing electric field. In 1987, Hayati et al. [106] studied the importance of liquid conductivity in the stability of jet streaming process. They showed that unstable jet streams whipped in different directions with broader diameter distribution which was due to high conductivity of fluids or under high electric field. While relatively stable jet streams were obtained with poor conducting

liquids such as paraffinic oil under relatively lower electric field. Electrospinning has become a vibrant topic for researchers since the works of Reneker and co-workers [100] who evidencing the electrospinning of organic nanomaterial in 1995. They studied the polyethylene oxide (PEO) nanofibers with different concentration and electric field and found that jet stream diameter decreases with increasing the distance between collector and the vertice of Taylor cone.

However there are numerous drawbacks in conventional needle-typed electrospinning such as low productivity and clogging problem at needle tip. Hence how to electrospin nanofiber in large scale has been in concern with further improvement in application of commercial market. Ding et al. [107] and Theron et al. [108] demonstrated multineedle spinneret electrospinning to improve yield of production. However, the system requires careful design of spinneret spacing so as to avoid unstable jet streaming due to strong electrostatic repulsion between jet streams. Recently, needleless electrospinning have been developed by Yarin et al. [109] to generate multiple jet streams without the use of needle nozzle but triggering by magnetic fluid on polymer solution surface. Later, Jirsak et al. [110] described the needleless electrospinning by a roller spinning unit which generates jet streams from a liquid uploaded on a rotating roller. The setup was subsequently commercialized by Elmarco under the brand name of Nanospider in 2003 which is illustrated in Figure 2.7. The needleless electrospinning improves the low production rate and the needle clogging problem as in conventional needle-type electrospinning.

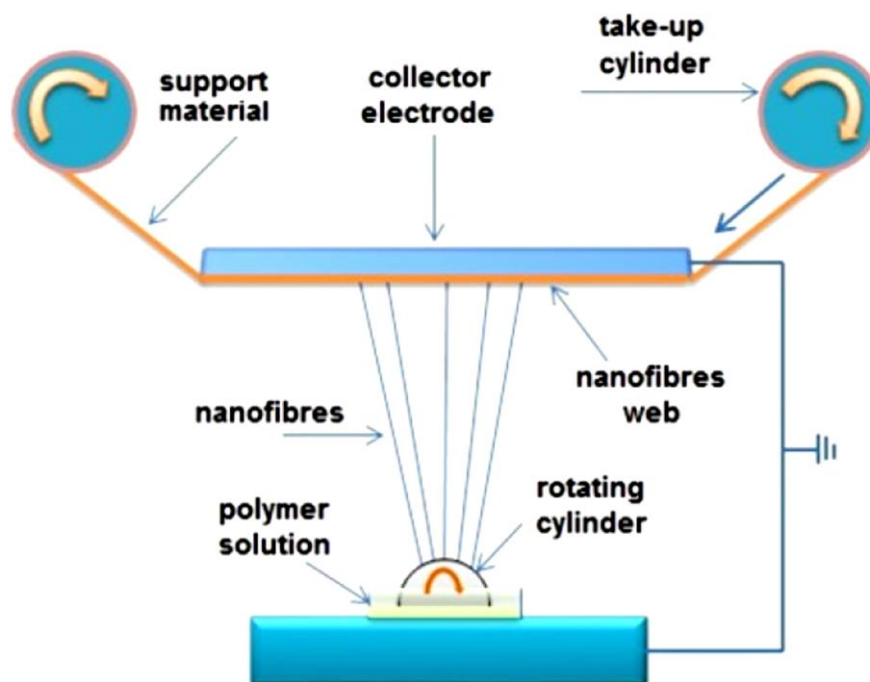


Figure 2.7 The operation of needleshless electrospinning. (Figure from reference [111])

2.4.2 Fiber formation process

In needleshless electrospinning unit Nanospider, the positive electrodes due to four thin wires are connected in a slowly rotating roller which is partially immersed in the precursor solution. The wires are charged at high voltage against the grounded collector held atop the roller. The solution loaded on the rotating wire would form many droplets and eventually Taylor cones as voltage keep increasing. When voltage increased to a critical value such that the electrostatic attraction between the droplet and the counter electrode is larger than the sum of the surface tension and gravitational force acting on the droplet, then fibers would be drawn upward from the droplet to the grounded collector. In brief, the electrospinning process has three main stages: (1) jet initiation from polymer solution, (2) Bending

instability during jet streaming and (3) jet solidification into nanofibers.

2.4.2.1 Jet initiation

When high potential is applied to the connecting wires immersed in the polymer solution, the free charges move to electrodes of opposite polarity which stress the surface by forming protrusions by electrical forces and surface tension. The accumulation of charges is greatest at the protrusion tip which eventually forms a conical shape known as Taylor Cone [104]. Taylor showed that a semi-vertical angle of 49.3° is formed when a critical potential is applied. As potential keep increased, a jet of polymer solution is pulled from the conical tip to the collector of opposite polarity. Recently, Yarin et al. [112] studied a family of nonself-similar solutions of hyperboloidal shapes and found that jet initiation occurs at conical shape of 33.5° which is less than the typical Taylor cone 49.3° . In addition, jet initiations with different conical shape angle were reported with a close association with the instability of the jet during streaming process [113]. The Images taken around the period of jet initiation are shown in Figure 2.8.

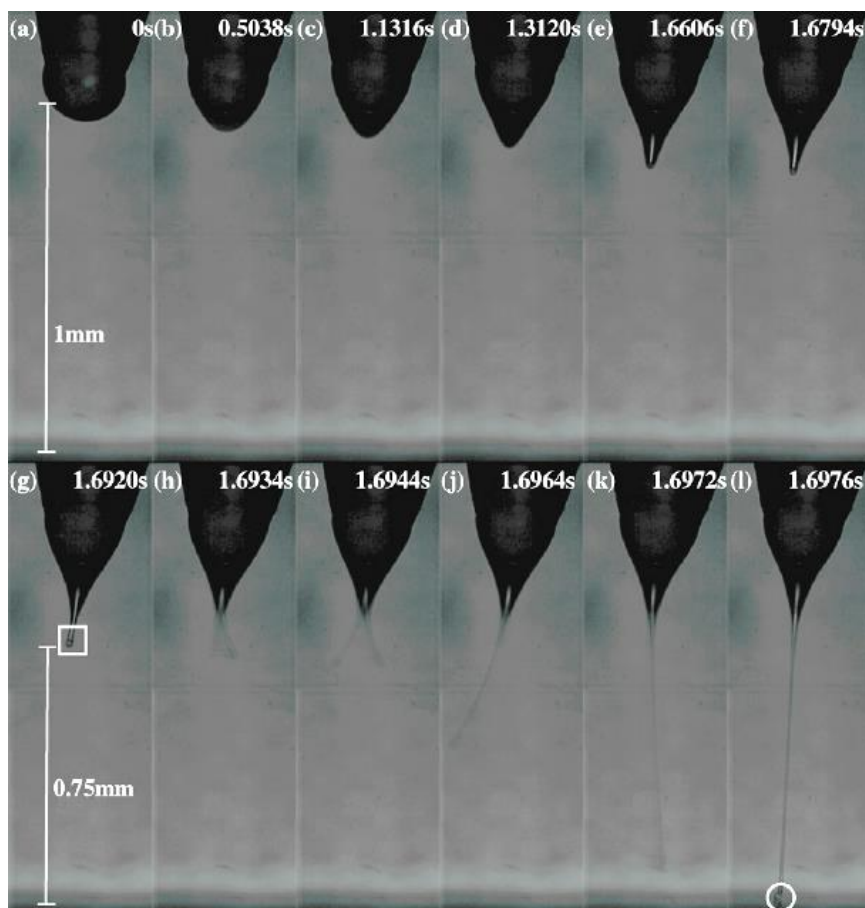


Figure 2.8 Images taken around the period of jet initiation. (Figure from reference [114])

2.4.2.2 Bending instability

When the jet ejected from Taylor cone, it is accelerating towards collector by electric field on the charges inside the jet under bending instability according to Yarin et al. [112] who suggested the mutually repulsive force exerted by the charges inside the jet would split the single jet into multiple thinner fibers, which is termed as splaying as shown in Figure 2.9. While Doshi and Reneker [100] argued that the splaying process was due to stretching of the jet and solvent evaporation which decreased the fiber diameter and resulted in larger charge density to split the single jet into multiple thinner jets. However, recently Warner

et al. [115] and Shin et al. [116] demonstrated the use of high speed camera to study the instability region of the jet, which was due to single rapidly whipping process which occurs too fast to appear as splitting into multiple thinner jets. Reneker and coworkers [117] contributed significantly in study of bending instability by developing a mathematical model for the viscoelastic jet under rectilinear electric field. In their work, the onset of jetting instability from the vertex of cone was observed with a high-frame rate electronic camera. According to them, a slight curvature in the jet developed into arrays of bends which becomes a series of spiraling loops with increasing diameters as shown in Figure 2.10. During the growth of spiral loop, the jet diameter decreased and it undergoes many cycles of instability before reaching the collector to form nanofibers. Besides, Shin et al. [116] modelled the bending instability by studying the competition of three different instabilities between the charges in the jet and electric field, such as (1) the Rayleigh axisymmetric instability (induced by mutually repulsive force exerted by charges in the jet), (2) electric field induced axisymmetric conducting instability and (3) whipping conducting instability. In their work, the stability of jet is modelled as a function of viscosity, conductivity, applied electric field and flow rate. They found that whipping instability dominates at high charge density in the jet while the axisymmetric instabilities dominate at low charge density. On the other hand, Fridrikh et al. [118] derived the ultimate jet diameter by accounting the nonlinear instability of the jets at final stage of whipping. In their work, the final whipping jet diameter is empirically modelled as Newtonian fluid in terms of flow rate, electric current and surface tension of the fluid.

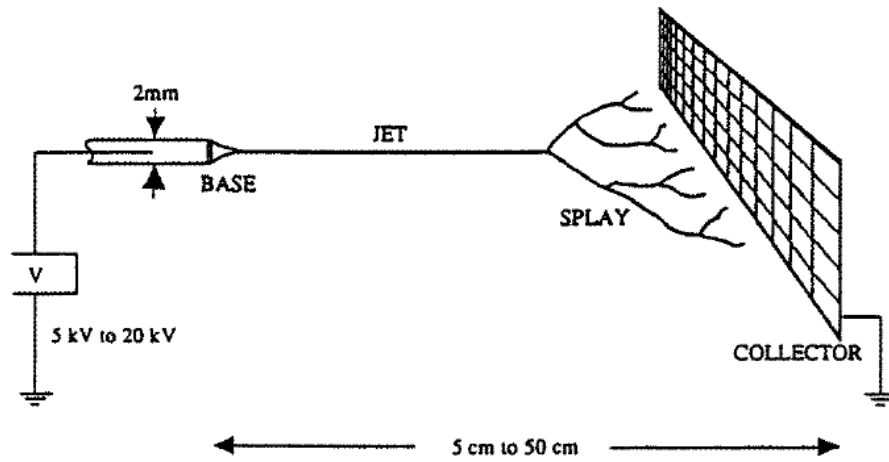


Figure 2.9 Bending instability during electrospinning. (Figure from reference [119])

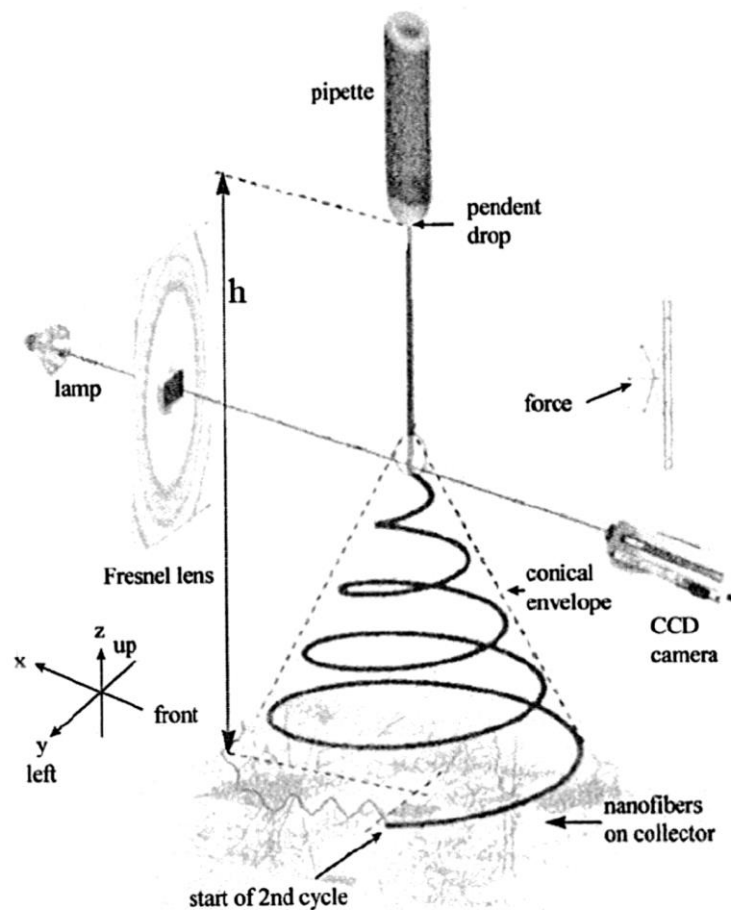


Figure 2.10 Spiral loop formation by curvature in the jet. (Figure from reference [117])

2.4.3 Fiber morphology control and parameters

2.4.3.1 Applied voltage

The onset of jet instabilities are attributed to the shape of cone in jet initiating process which could be controlled by applied voltage between the electrodes. Deitzel et al. [120] demonstrated that spinning current or applied voltage is related to the jet bending instability and the fiber morphology. In their work, polyethylene oxide (PEO)/water system current was found to increase with applied voltage. Current increased with charges accumulated at the jet initiating surface which deform the geometrical shape of Taylor cone and hence related with change in instability modes. It was observed that the fiber morphology was defect-free at applied voltage of 5.5 kV, but changed to a highly beaded structure at voltage of 9.0 kV for the PEO/water system.

Applied voltage not only affects the jet instability mode but also fiber diameter and length. Baumgarten [105] reported an increase of fiber length with smaller fiber diameter with an increase of applied voltage for acrylic fibers. Jaeger et al. [121] attempted to reduce instability by introducing a ring electrode between nozzle and collector. The ring electrode was set at the same potential with the electrode immersed in polymer solution which aimed to reduce instability at jet initiating stage. However, bending instability still dominates at later stages of the process. Deitzel et al. [122] demonstrated using a series of eight copper rings between nozzle and collector to reduce bending instability as shown in Figure 2.11. The copper rings were set at lower positive potentials than the electrode immersed in polymer solution, which converge the macroscopic electric field to a

centered field along the axis of centers of the rings. They suggested the setup dampened bending instability by producing straight jet lines and smaller fiber diameters due to the converged electric field.

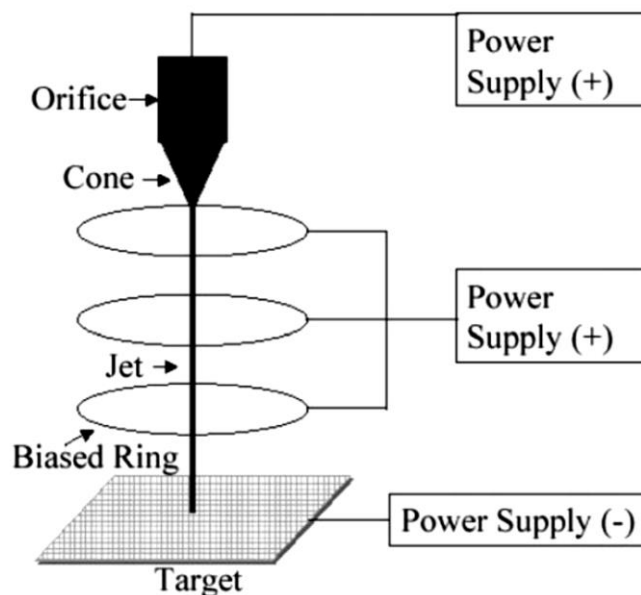


Figure 2.11 The multiple field technique. (Figure from reference [122])

2.4.3.2 Nozzle-collector distance

The structure and morphology of fibers are closely related to the nozzle-collector distance due to the evaporation time of solvent and instability period. Buchko et al. [123] showed that decreasing the nozzle-collector distance resulted in wet fibers with beaded structure for silk like polymer with fibronectin functionality (SLPF) fibers. The fiber morphology also changed from round to flat shape when the nozzle-collector distance decreased from 2 cm to 0.5 cm. Similarly, Megelski et al. [124] reported with beaded fiber structure with decreasing the nozzle-collector distance for polystyrene fiber system.

2.4.3.3 Relative humidity

Environmental condition such as relative humidity also affects the fiber structure and morphology. Baumgarten [105] observed the acrylic fibers were entangled and not dried properly for relative humidity higher than 60%. Srinivasarao et al. [125] suggested the porous fiber structure by evaporative cooling process of moisture droplets in air onto fiber surface. The pores are known as the “breathe figures”.

2.4.3.4 Solution concentration

Solution concentration could vary solution viscosity and surface tension which could determine the fiber structure and morphology. Low concentration solution might not have electrospinning but electro spraying due to the low surface tension of droplets which could not maintain a continuous jet stream. On the contrary, high concentration solution would block the nozzle for electrospinning or fiber diameter increased due to higher viscosity and surface tension. Deitzel et al. [122] demonstrated the relationship between fiber diameter and solution concentration by a power law in PEO/water system. They interpreted the fiber morphology to the shape of the cone at jet initiation process.

2.4.3.5 Solution conductivity

Solution conductivity or charge density in the jet is also important in determining fiber diameter. Higher solution conductivity accompanied with higher charge density in the jet which would experience a larger tensile force with the applied electric field. Baumgarten [105] reported the jet radius varied inversely with the

cube root of the electrical conductivity of the solution. Zong et al. [126] found that PDLA fibers were formed with smaller diameters and beadless structure with addition of ionic salts such as KH_2PO_4 , NaH_2PO_4 and NaCl .

2.4.3.6 Volatility of solvent

The volatility of solvent plays a major role in solvent evaporation and phase separation in the jet during electrospinning. Lee et al. [127] demonstrated the relationship between volume ratio of solvent in solution on fiber diameter and morphology using PVC fibers such that fiber diameter decreased with increasing the solvent DMF. Megelski et al. [124] demonstrated the PS fibers were spun with much smaller fiber diameters with different THF/DMF concentrations.

2.5 Gas sensing mechanism

2.5.1 Formation of Space charge layer

In gas sensors, the sensing mechanisms are mostly based on the studies of tin oxide as investigated by Yamazoe et al. and the coworkers [55,56,128–131]. According to them, the gas sensing mechanism consists of two important functions, namely receptor function and transducer function. In general, receptor function would recognize the gas analyte by some measurable variables such as resistance while transducer function would transduce the response to output signal such as change of resistance. Actually tin oxide is an n-type semiconductor due to the introduction of oxygen vacancies after calcinations. The oxygen vacancies act as electron donors and make it an n-type semiconductor. When an oxidizing gas

adsorbs on SnO_2 surface, electrons could be transferred to this molecule if the lowest unoccupied molecular orbitals (LUMO) of the molecule lies below the Fermi level of SnO_2 . On the contrary, if a reducing gas adsorbed on SnO_2 surface, electrons would be donated to SnO_2 if the highest occupied molecular orbitals (HOMO) lie above the Fermi-level of SnO_2 . The receptor function, transducer function and the electron depleted layer are shown in Figure 2.12.

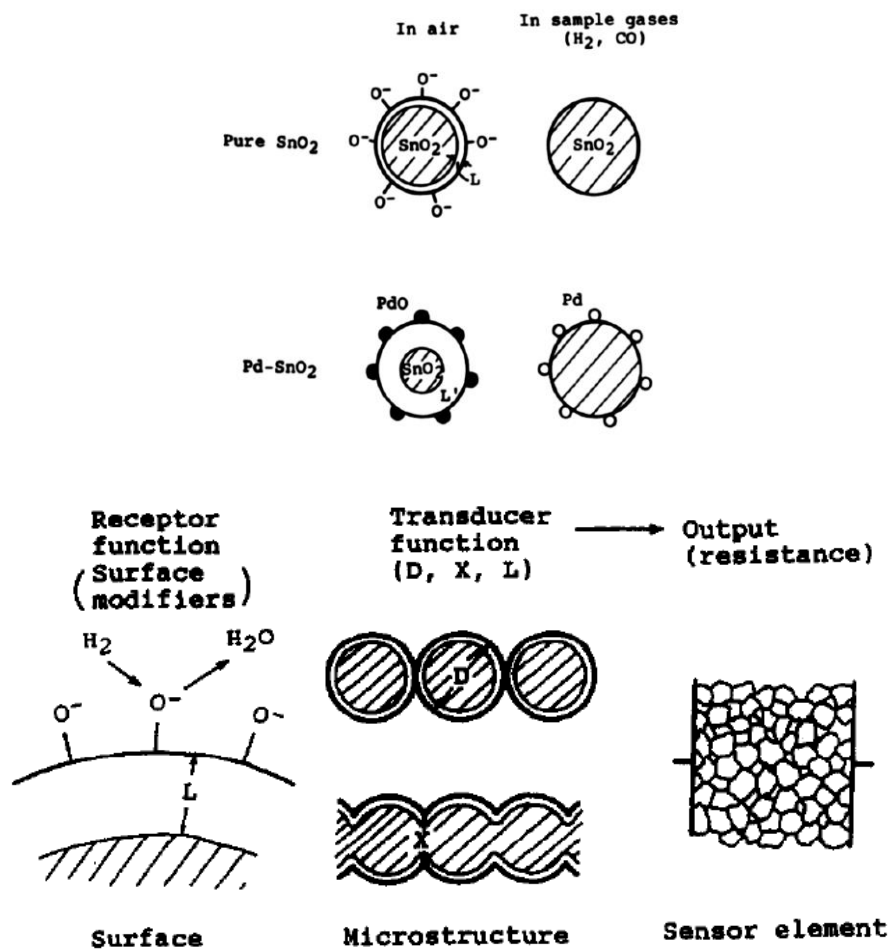


Figure 2.12 A schematic diagram showing the receptor function, transducer function and the space charge layer (electron depleted layer). (Figures from reference [129])

If tin dioxide is placed in the atmosphere, oxygen gas would be adsorbed onto the semiconductor surface. Since oxygen is an oxidizing gas, it would extract

electrons from the bulk of semiconductor, and generate a repulsive electrostatic force close to the surface which forms a space charge layer or an electron depleted region as illustrated in Figure 2.13. The Debye length (Λ_{air}) is the length of the space charge layer. The repulsive electrostatic force generated from the negative charge at surface cause an upward bending in energy bands in SnO_2 . The potential barrier for electrons in bulk of SnO_2 to overcome to surface state is known as Schottky barrier V_{surface} .

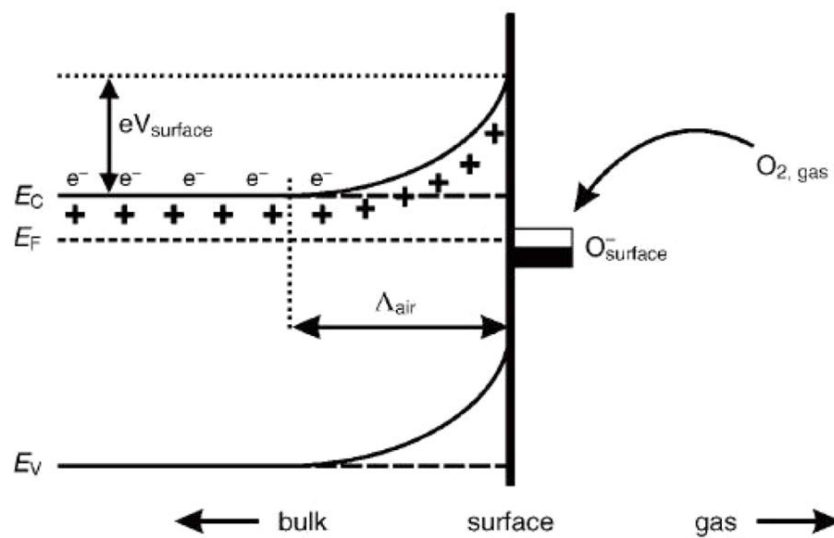
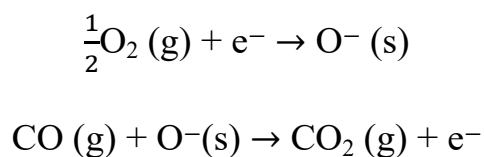


Figure 2.13 A schematic diagram showing the formation of space charge layer upon oxygen adsorption on SnO_2 surface. (Figure from reference [132])

Oxygen in air would be dissociated to O atom which adsorb onto SnO_2 surface at working temperatures (300-450°C) of SnO_2 gas sensor. Since oxygen is electron withdrawing which extract and bound electrons at surface to form ionic O^- and then create a space charge layer which increase the Schottky barrier and hence resistance. If the gas analyte is a reducing gas such as CO, it would react with the surface-adsorbed oxygen ion (O^-) to form CO_2 by releasing an electron

back to the bulk such that the Schottky barrier decreases and conduction path of the bulk region increases. Therefore resistance of the semiconductor decreases for a reducing gas analyte. The response is reversed for an oxidizing gas analyte. An equation describes the surface reaction of the receptor oxygen and reducing gas analyte CO as follows:



2.5.2 Factors affecting sensitivity

2.5.2.1 Grain boundary barrier effect (Schottky barrier effect)

When two grains are come into contact with each other, there is a potential barrier known as Schottky barrier across the boundary induced by the space charge layer. When electron transmits from the conducting bulk region across the grain boundary to the other grain, it has to overcome the potential barrier at the boundary due to the contact of the two electron depleted region as shown in Figure 2.14. Therefore the change of resistance or the transducer function increases. Therefore when grain boundaries increase, the accumulative change of resistance also increases which explains the fact that polycrystalline material has higher sensitivity than the monocrystalline counterpart. Also, small grain size material would have a larger sensitivity than large grain size with the same mass due to more grain boundaries.

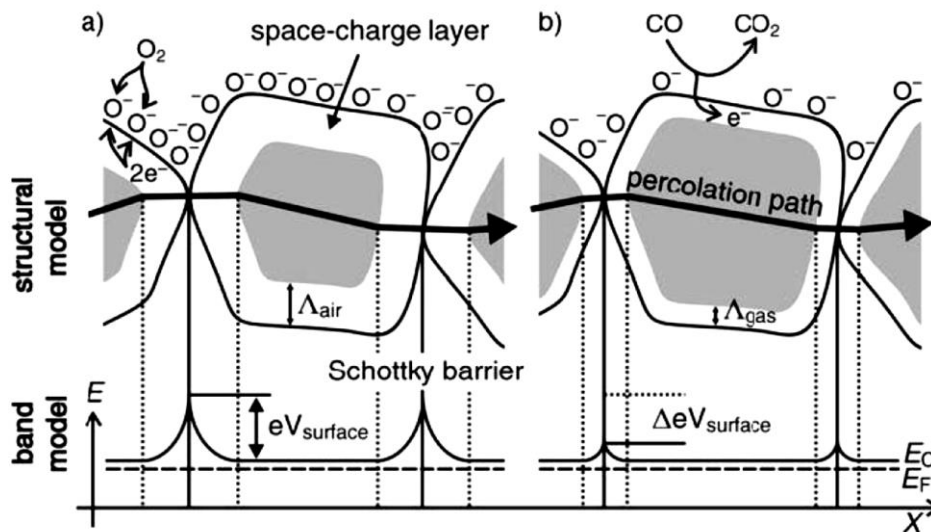


Figure 2.14 A schematic diagram showing the conductive path of charge carriers in bulk region varied due to different Schottky barriers at boundaries. (Figure from reference [132])

2.5.2.2 p-n junction effect

Similar to the grain boundary barrier, space charge layer could be increased from a p-n junction such that the holes in the p-type material at the boundary would be filled by the mobile electrons of the n-type material. Therefore the available valence states have been totally exhausted at the p-n junction which increased the space charge layer. When electron transmits through the p-n junction, it has to overcome a potential barrier such that the change of resistance of the transducer function increases. This is also the reason why gas sensitivity increases when p-type graphene is incorporated with n-type tin oxide.

2.5.2.3 Grain size effect

From the grain boundary analysis, it is expected that smaller grain size has larger

sensitivity. However, sensitivity does not increase linearly with decreasing grain size. From the studies of Xu et al. [130] and the coworkers [129], grain size (D) has a significant effect on sensitivity. According to their works, for $D > 20$ nm, the sensitivity is independent of the grain size; for $D < 20$ nm, the sensitivity increases slightly; but when $D < 10$ nm, the sensitivity increases incredibly even for a slight decrease in D . Therefore there are three sections of sensitivity control by grain size which are depicted in Figure 2.15.

(1) $D > 2L$ (Grain boundary control)

This is the range for a large grain when $D > 2L$ (L is the length of space charge layer). The sensitivity is independent on the grain size in this range since the transmission of e^- only experiences a resistance increase at the grain boundary which is independent of the grain size.

(2) $D \approx 2L$ (Neck control)

This is the medium grain size when D is close to $2L$ but still larger than $2L$. In this case, the electron depleted layer a grain extends into the bulk region of the adjacent grain which results in a constricted bulk region like a neck at the boundary. The transmission of e^- would experience a resistance increase at the constricted neck region at the boundary. For this case, sensitivity not only depends on grain boundaries but also the constricted neck size of the bulk at boundaries.

(3) $D < 2L$ (Grain control)

This is the range for small grain size when $D < 2L$. In this case, the space charge layer of a grain extends to cover the overall bulk region of the adjacent grain.

Therefore the mobile charge carriers inside the grains are totally exhausted that the resistance greatly increases. The grains now become insulating and the signal transmission would experience no resistance increase when crossing the neck or grain boundaries. Hence the sensitivity for this case is essentially controlled by the grain's inter-crystallite properties. Quantum confinement and tunneling may be accounted for this case. However, the sensing mechanism is still not clear and needs further elaboration.

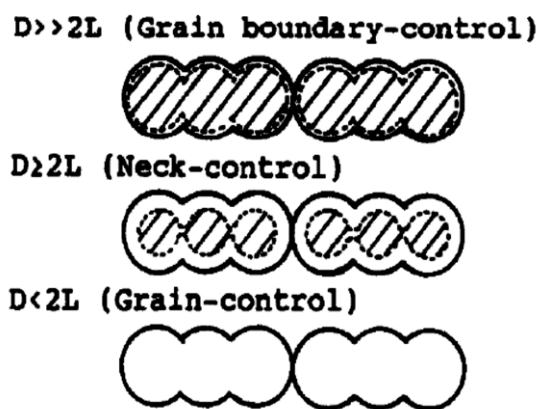


Figure 2.15 A schematic diagram of the grain size effect. (Figure from reference [129])

2.5.2.4 Additive effect

2.5.2.4.1 Chemical additive effect

The chemical additives on grain surface do not react with the adsorbed oxygen, but only act as catalyst to help dissociate the gas analyte to react with the adsorbed oxygen [128,129]. Here, the additives do not substitute the oxygen as the receptor function such that the space charge layer does not change for adding the additives. The process of the catalysis of the dissociation of the gas analyte by additive is also known as spill-over effect such that the rate of reaction between the gas

analytes and adsorbed oxygens increases. The increase in sensitivity by chemical additive is due to the increase in response time. Pt is an example for this case since it could not react with adsorbed oxygen to form stable oxide.

2.5.2.4.2 Electronic additive effect

On the contrary of chemical additive, electronic additive on grain surface would react with the adsorbed oxygen to form stable oxide [128,129]. Here, the receptor function is mainly due to the additive oxide rather than the adsorbed oxygen. The space charge layer induced by the additive oxide on grain surface is stronger than that induced by the solely adsorbed oxygen. When reducing gas analyte reacts with additive oxide, the additive's electronic state would be reduced resulting in a larger change of electron depleted layer. Therefore the increase in sensitivity by electronic additive is due to the increase in space charge layer. Pd and Ag are examples for this case since they could react with adsorbed oxygen to form stable oxide. A comparison of chemical and electronic additive effects towards a gas analyte is summarized in Table 2.1.

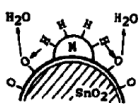
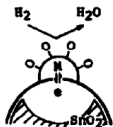
Type	Chemical	Electronic
Model		
Role of noble metal	Activation and spill-over of sample gas	Electron donor or acceptor
Origin of gas-sensitive properties	Change of adsorbed oxygen concentration	Change of oxidation state of noble metal
Example	Pt-SnO ₂	Ag ₂ O-SnO ₂ , PdO-SnO ₂

Table 2.1 A comparison of chemical and electronic additive effects towards a gas analyte. (Table from reference [128,129])

2.5.2.5 Porosity effect

2.5.2.5.1 Intrinsic void

The intrinsic void is the natural empty space between grains when they come into contact with each other. Therefore intrinsic void space is the natural empty space which is inevitable and unavoidable from any synthesis method. When grain size becomes smaller, the intrinsic void space also decreases which in turn decreases the permeation rate of the gases. Moreover, the intrinsic void space could be detrimental on the diffusion of gases with large molecular size when grains become much smaller. In comparison, larger grain size has larger intrinsic void space which benefits the diffusion of gases.

2.5.2.5.2 Chemical pore

Secondly, chemical pores are resulted from the synthesis process such as effervescence or the emission of gases from the bulk. Some semiconductors such as iron oxide and manganese oxide have the ability to induce porosities during the synthesis which greatly enhance gas sensitivity due to the increase of surface area [133,134].

2.5.2.5.3 Thermal crack/pore

Finally, thermal cracks are mostly resulted from thermal heating induced by different expansion rates or bond strengths of hetero-materials. Heating materials with viscous polymers or organic solvents is usually accompanied with the emission of carbon dioxide from the bulk which results in thermal pores.

2.6 Summary

This chapter begins with the fabrication methods of graphene by top-down approach and bottom-up approach. Top-down approach using chemical oxidation of graphite flake with Modified Hummers method to produce GO and then reduced GO with different reduction methods such as thermal method, microwave and photo method, chemical method, electrochemical method, solvothermal method and multi-step method. While bottom-up approach use CVD method to produce defect-free graphene. Although, graphene produced from bottom-up approach produce defect-free graphitic plane, it is reported that the pristine graphene has low sensitivities to gas sensing due to the lack of high energy binding sites such as functional groups in metal oxides or polymers. Therefore, it is expected that the defects of graphene synthesized by top-down approach could be a merit in gas sensing on the contrary due to the introduction of defects such as oxygen functional groups, voids and distortion in the basal network.

Electrospinning is a simple and versatile method of producing nanofibers from a precursor solution by applying high electrical voltage. It is widely used in the area of biomedical scaffolds, tissue engineering, filtration medium and batteries since the works of Reneker and co-workers who evidencing the electrospinning of organic nanomaterial in 1995. The problems of low production rate and needle clogging in conventional needle-type electrospinning have been solved by the needleless electrospinning unit or roller electrospinning initiated by Jirsak et al. in 2003. Indeed, nanofibers are promising material in gas sensing due to the high surface area and porosity which is most efficient in transducing gaseous interactions to electrical signal.

Finally, the sensing mechanisms of tin dioxide are introduced with formation of space charge layer with Schottky barrier by oxygen adsorbed on the surface. The sensitivity of tin dioxide are affected by several factors such as grain boundary effect (Schottky barrier effect), p-n junction effect, grain size effect, additives effect and porosity effect. However, the detailed sensing mechanism of graphene family has not been reported such as the difference of interaction of the gases between different oxygen functional groups.

References:

- [1] M.J. Allen, V.C. Tung, R.B. Kaner, Honeycomb Carbon: A Review of Graphene, *Chem. Rev.* 110 (2010) 132–145. doi:10.1021/cr900070d.
- [2] T. Gan, S. Hu, Electrochemical sensors based on graphene materials, *Microchim. Acta.* 175 (2011) 1.
- [3] E.V. Iski, E.N. Yitamben, L. Gao, N.P. Guisinger, Graphene at the Atomic-Scale: Synthesis, Characterization, and Modification, *Adv. Funct. Mater.* 23 (2013) 2554–2564. doi:10.1002/adfm.201203421.
- [4] Y. Shao, J. Wang, H. Wu, J. Liu, I.A. Aksay, Y. Lin, Graphene Based Electrochemical Sensors and Biosensors: A Review, *Electroanalysis.* 22 (2010) 1027–1036. doi:10.1002/elan.200900571.
- [5] S. Wu, Q. He, C. Tan, Y. Wang, H. Zhang, Graphene-Based Electrochemical Sensors, *Small.* 9 (2013) 1160–1172.
- [6] F. Yavari, N. Koratkar, Graphene-Based Chemical Sensors, *J. Phys. Chem. Lett.* 3 (2012) 1746–1753. doi:10.1021/jz300358t.
- [7] W. Yuan, G. Shi, Graphene-based gas sensors, *J. Mater. Chem. A.* 1 (2013) 10078. doi:10.1039/c3ta11774j.
- [8] S. Pei, H.-M. Cheng, The reduction of graphene oxide, *Carbon.* 50 (2012) 3210–3228.
- [9] S. Stankovich, D.A. Dikin, R.D. Piner, K.A. Kohlhaas, A. Kleinhammes, Y. Jia, Y. Wu, S.T. Nguyen, R.S. Ruoff, Synthesis of graphene-based nanosheets via chemical reduction of exfoliated graphite oxide, *Carbon.* 45 (2007) 1558–1565.

- [10] X. Dong, P. Wang, W. Fang, C.-Y. Su, Y.-H. Chen, L.-J. Li, W. Huang, P. Chen, Growth of large-sized graphene thin-films by liquid precursor-based chemical vapor deposition under atmospheric pressure, *Carbon*. 49 (2011) 3672–3678. doi:10.1016/j.carbon.2011.04.069.
- [11] A. Guermoune, T. Chari, F. Popescu, S.S. Sabri, J. Guillemette, H.S. Skulason, T. Szkopek, M. Siaj, Chemical vapor deposition synthesis of graphene on copper with methanol, ethanol, and propanol precursors, *Carbon*. 49 (2011) 4204–4210. doi:10.1016/j.carbon.2011.05.054.
- [12] W. Liu, H. Li, C. Xu, Y. Khatami, K. Banerjee, Synthesis of high-quality monolayer and bilayer graphene on copper using chemical vapor deposition, *Carbon*. 49 (2011) 4122–4130. doi:10.1016/j.carbon.2011.05.047.
- [13] H.J. Park, J. Meyer, S. Roth, V. Skákalová, Growth and properties of few-layer graphene prepared by chemical vapor deposition, *Carbon*. 48 (2010) 1088–1094. doi:10.1016/j.carbon.2009.11.030.
- [14] W.S. Hummers Jr, R.E. Offeman, Preparation of graphitic oxide, *J. Am. Chem. Soc.* 80 (1958) 1339–1339.
- [15] T. Szabó, O. Berkesi, P. Forgó, K. Josepovits, Y. Sanakis, D. Petridis, I. Dékány, Evolution of surface functional groups in a series of progressively oxidized graphite oxides, *Chem. Mater.* 18 (2006) 2740–2749.
- [16] W. Gao, L.B. Alemany, L. Ci, P.M. Ajayan, New insights into the structure and reduction of graphite oxide, *Nat. Chem.* 1 (2009) 403–408.
- [17] A. Lerf, H. He, M. Forster, J. Klinowski, Structure of graphite oxide revisited, *J. Phys. Chem. B.* 102 (1998) 4477–4482.

- [18] D. Chen, H. Feng, J. Li, Graphene Oxide: Preparation, Functionalization, and Electrochemical Applications, *Chem. Rev.* 112 (2012) 6027–6053. doi:10.1021/cr300115g.
- [19] H.C. Schniepp, J.-L. Li, M.J. McAllister, H. Sai, M. Herrera-Alonso, D.H. Adamson, R.K. Prud'homme, R. Car, D.A. Saville, I.A. Aksay, Functionalized single graphene sheets derived from splitting graphite oxide, *J. Phys. Chem. B.* 110 (2006) 8535–8539.
- [20] Z.-S. Wu, W. Ren, L. Gao, B. Liu, C. Jiang, H.-M. Cheng, Synthesis of high-quality graphene with a pre-determined number of layers, *Carbon.* 47 (2009) 493–499.
- [21] H.M. Hassan, V. Abdelsayed, S.K. Abd El Rahman, K.M. AbouZeid, J. Ternner, M.S. El-Shall, S.I. Al-Resayes, A.A. El-Azhary, Microwave synthesis of graphene sheets supporting metal nanocrystals in aqueous and organic media, *J. Mater. Chem.* 19 (2009) 3832–3837.
- [22] Y. Zhu, S. Murali, M.D. Stoller, A. Velamakanni, R.D. Piner, R.S. Ruoff, Microwave assisted exfoliation and reduction of graphite oxide for ultracapacitors, *Carbon.* 48 (2010) 2118–2122.
- [23] L.J. Cote, R. Cruz-Silva, J. Huang, Flash reduction and patterning of graphite oxide and its polymer composite, *J. Am. Chem. Soc.* 131 (2009) 11027–11032.
- [24] Y. Zhang, L. Guo, S. Wei, Y. He, H. Xia, Q. Chen, H.-B. Sun, F.-S. Xiao, Direct imprinting of microcircuits on graphene oxides film by femtosecond laser reduction, *Nano Today.* 5 (2010) 15–20.
- [25] M.J. Fernández-Merino, L. Guardia, J.I. Paredes, S. Villar-Rodil, P. Solís-Fernández, A. Martínez-Alonso, J.M.D. Tascón, Vitamin C is an ideal

- substitute for hydrazine in the reduction of graphene oxide suspensions, *J. Phys. Chem. C*. 114 (2010) 6426–6432.
- [26] W. Gao, L.B. Alemany, L. Ci, P.M. Ajayan, New insights into the structure and reduction of graphite oxide, *Nat. Chem.* 1 (2009) 403–408.
- [27] I.K. Moon, J. Lee, R.S. Ruoff, H. Lee, Reduced graphene oxide by chemical graphitization, *Nat. Commun.* 1 (2010) 73.
- [28] S. Pei, J. Zhao, J. Du, W. Ren, H.-M. Cheng, Direct reduction of graphene oxide films into highly conductive and flexible graphene films by hydrohalic acids, *Carbon*. 48 (2010) 4466–4474.
- [29] H.-J. Shin, K.K. Kim, A. Benayad, S.-M. Yoon, H.K. Park, I.-S. Jung, M.H. Jin, H.-K. Jeong, J.M. Kim, J.-Y. Choi, others, Efficient reduction of graphite oxide by sodium borohydride and its effect on electrical conductance, *Adv. Funct. Mater.* 19 (2009) 1987–1992.
- [30] S. Stankovich, D.A. Dikin, R.D. Piner, K.A. Kohlhaas, A. Kleinhammes, Y. Jia, Y. Wu, S.T. Nguyen, R.S. Ruoff, Synthesis of graphene-based nanosheets via chemical reduction of exfoliated graphite oxide, *Carbon*. 45 (2007) 1558–1565.
- [31] S. Stankovich, R.D. Piner, X. Chen, N. Wu, S.T. Nguyen, R.S. Ruoff, Stable aqueous dispersions of graphitic nanoplatelets via the reduction of exfoliated graphite oxide in the presence of poly (sodium 4-styrenesulfonate), *J. Mater. Chem.* 16 (2006) 155–158.
- [32] S.J. An, Y. Zhu, S.H. Lee, M.D. Stoller, T. Emilsson, S. Park, A. Velamakanni, J. An, R.S. Ruoff, Thin film fabrication and simultaneous anodic reduction of deposited graphene oxide platelets by electrophoretic deposition, *J. Phys. Chem. Lett.* 1 (2010) 1259–1263.

- [33] G.K. Ramesha, S. Sampath, Electrochemical reduction of oriented graphene oxide films: an in situ Raman spectroelectrochemical study, *J. Phys. Chem. C.* 113 (2009) 7985–7989.
- [34] Z. Wang, X. Zhou, J. Zhang, F. Boey, H. Zhang, Direct electrochemical reduction of single-layer graphene oxide and subsequent functionalization with glucose oxidase, *J. Phys. Chem. C.* 113 (2009) 14071–14075.
- [35] M. Zhou, Y. Wang, Y. Zhai, J. Zhai, W. Ren, F. Wang, S. Dong, Controlled synthesis of large-area and patterned electrochemically reduced graphene oxide films, *Chem. Eur. J.* 15 (2009) 6116–6120.
- [36] S. Dubin, S. Gilje, K. Wang, V.C. Tung, K. Cha, A.S. Hall, J. Farrar, R. Varshneya, Y. Yang, R.B. Kaner, A one-step, solvothermal reduction method for producing reduced graphene oxide dispersions in organic solvents, *ACS Nano.* 4 (2010) 3845–3852.
- [37] H. Wang, J.T. Robinson, X. Li, H. Dai, Solvothermal reduction of chemically exfoliated graphene sheets, *J. Am. Chem. Soc.* 131 (2009) 9910–9911.
- [38] Y. Zhou, Q. Bao, L.A.L. Tang, Y. Zhong, K.P. Loh, Hydrothermal dehydration for the “green” reduction of exfoliated graphene oxide to graphene and demonstration of tunable optical limiting properties, *Chem. Mater.* 21 (2009) 2950–2956.
- [39] H. Chen, M.B. Müller, K.J. Gilmore, G.G. Wallace, D. Li, Mechanically strong, electrically conductive, and biocompatible graphene paper, *Adv. Mater.* 20 (2008) 3557–3561.

- [40] G. Eda, G. Fanchini, M. Chhowalla, Large-area ultrathin films of reduced graphene oxide as a transparent and flexible electronic material, *Nat. Nanotechnol.* 3 (2008) 270–274.
- [41] W. Gao, L.B. Alemany, L. Ci, P.M. Ajayan, New insights into the structure and reduction of graphite oxide, *Nat. Chem.* 1 (2009) 403–408.
- [42] Y. Si, E.T. Samulski, Synthesis of water soluble graphene, *Nano Lett.* 8 (2008) 1679–1682.
- [43] C. Zhang, W. Lv, X. Xie, D. Tang, C. Liu, Q.-H. Yang, Towards low temperature thermal exfoliation of graphite oxide for graphene production, *Carbon.* 62 (2013) 11–24.
- [44] I.K. Moon, J. Lee, R.S. Ruoff, H. Lee, Reduced graphene oxide by chemical graphitization, *Nat. Commun.* 1 (2010) 73.
- [45] S. Thakur, N. Karak, Green reduction of graphene oxide by aqueous phytoextracts, *Carbon.* 50 (2012) 5331–5339.
- [46] X. Fan, W. Peng, Y. Li, X. Li, S. Wang, G. Zhang, F. Zhang, Deoxygenation of exfoliated graphite oxide under alkaline conditions: a green route to graphene preparation, *Adv. Mater.* 20 (2008) 4490–4493.
- [47] C. Nethravathi, M. Rajamathi, Chemically modified graphene sheets produced by the solvothermal reduction of colloidal dispersions of graphite oxide, *Carbon.* 46 (2008) 1994–1998.
- [48] D. Luo, G. Zhang, J. Liu, X. Sun, Evaluation criteria for reduced graphene oxide, *J. Phys. Chem. C.* 115 (2011) 11327–11335.
- [49] X. Gao, J. Jang, S. Nagase, Hydrazine and thermal reduction of graphene oxide: reaction mechanisms, product structures, and reaction design, *J. Phys. Chem. C.* 114 (2009) 832–842.

- [50] N. Song, H. Fan, H. Tian, PVP assisted in situ synthesis of functionalized graphene/ZnO (FGZnO) nanohybrids with enhanced gas-sensing property, *J. Mater. Sci.* 50 (2015) 2229–2238.
- [51] D. Luo, G. Zhang, J. Liu, X. Sun, Evaluation criteria for reduced graphene oxide, *J. Phys. Chem. C.* 115 (2011) 11327–11335.
- [52] J. Shen, Y. Hu, M. Shi, X. Lu, C. Qin, C. Li, M. Ye, Fast and facile preparation of graphene oxide and reduced graphene oxide nanoplatelets, *Chem. Mater.* 21 (2009) 3514–3520.
- [53] E. Kayhan, R.M. Prasad, A. Gurlo, O. Yilmazoglu, J. Engstler, E. Ionescu, S. Yoon, A. Weidenkaff, J.J. Schneider, Synthesis, Characterization, Electronic and Gas-Sensing Properties towards H₂ and CO of Transparent, Large-Area, Low-Layer Graphene, *Chem. Eur. J.* 18 (2012) 14996–15003.
- [54] S. Bhaviripudi, X. Jia, M.S. Dresselhaus, J. Kong, Role of kinetic factors in chemical vapor deposition synthesis of uniform large area graphene using copper catalyst, *Nano Lett.* 10 (2010) 4128–4133.
- [55] J.F. McAleer, P.T. Moseley, J.O. Norris, D.E. Williams, B.C. Tofield, Tin dioxide gas sensors. Part 2.—The role of surface additives, *J. Chem. Soc. Faraday Trans. 1 Phys. Chem. Condens. Phases.* 84 (1988) 441–457.
- [56] J.F. McAleer, P.T. Moseley, J.O. Norris, D.E. Williams, Tin dioxide gas sensors. Part 1.—Aspects of the surface chemistry revealed by electrical conductance variations, *J. Chem. Soc. Faraday Trans. 1 Phys. Chem. Condens. Phases.* 83 (1987) 1323–1346.
- [57] J. Watson, The tin oxide gas sensor and its applications, *Sens. Actuators.* 5 (1984) 29–42.

- [58] A. Maddalena, R. Dal Maschio, S. Dire, A. Raccanelli, Electrical conductivity of tin oxide films prepared by the sol-gel method, *J. Non-Cryst. Solids*. 121 (1990) 365–369.
- [59] S.-S. Park, J.D. Mackenzie, Sol-gel-derived tin oxide thin films, *Thin Solid Films*. 258 (1995) 268–273.
- [60] R. Rella, A. Serra, P. Siciliano, L. Vasanelli, G. De, A. Licciulli, A. Quirini, Tin oxide-based gas sensors prepared by the sol-gel process, *Sens. Actuators B Chem.* 44 (1997) 462–467.
- [61] J. Zhang, L. Gao, Synthesis and characterization of nanocrystalline tin oxide by sol-gel method, *J. Solid State Chem.* 177 (2004) 1425–1430.
- [62] N.S. Baik, G. Sakai, N. Miura, N. Yamazoe, Hydrothermally treated sol solution of tin oxide for thin-film gas sensor, *Sens. Actuators B Chem.* 63 (2000) 74–79.
- [63] H.-C. Chiu, C.-S. Yeh, Hydrothermal synthesis of SnO₂ nanoparticles and their gas-sensing of alcohol, *J. Phys. Chem. C*. 111 (2007) 7256–7259.
- [64] O. Lupan, L. Chow, G. Chai, A. Schulte, S. Park, H. Heinrich, A rapid hydrothermal synthesis of rutile SnO₂ nanowires, *Mater. Sci. Eng. B*. 157 (2009) 101–104.
- [65] J. Zhang, L. Gao, Synthesis and characterization of antimony-doped tin oxide (ATO) nanoparticles by a new hydrothermal method, *Mater. Chem. Phys.* 87 (2004) 10–13.
- [66] M. Krishna, S. Komarneni, Conventional-vs microwave-hydrothermal synthesis of tin oxide, SnO₂ nanoparticles, *Ceram. Int.* 35 (2009) 3375–3379.

- [67] J. Kane, H.P. Schweizer, W. Kern, Chemical vapor deposition of transparent, electrically conductive tin oxide films formed from dibutyl tin diacetate, *J. Electrochem. Soc.* 122 (1975) 1144–1149.
- [68] Y. Liu, E. Koep, M. Liu, A highly sensitive and fast-responding SnO₂ sensor fabricated by combustion chemical vapor deposition, *Chem. Mater.* 17 (2005) 3997–4000.
- [69] Y. Liu, M. Liu, Growth of Aligned Square-Shaped SnO₂ Tube Arrays, *Adv. Funct. Mater.* 15 (2005) 57–62.
- [70] A. Czapla, E. Kusior, M. Bucko, Optical properties of non-stoichiometric tin oxide films obtained by reactive sputtering, *Thin Solid Films.* 182 (1989) 15–22.
- [71] T. Minami, H. Nanto, S. Takata, Highly conducting and transparent SnO₂ thin films prepared by RF magnetron sputtering on low-temperature substrates, *Jpn. J. Appl. Phys.* 27 (1988) L287.
- [72] R.E. Presley, C.L. Munsee, C.H. Park, D. Hong, J.F. Wager, D.A. Keszler, Tin oxide transparent thin-film transistors, *J. Phys. Appl. Phys.* 37 (2004) 2810.
- [73] Y. Suda, H. Kawasaki, J. Namba, K. Iwatsuji, K. Doi, K. Wada, Properties of palladium doped tin oxide thin films for gas sensors grown by PLD method combined with sputtering process, *Surf. Coat. Technol.* 174 (2003) 1293–1296.
- [74] M.M. Arafat, B. Dinan, S.A. Akbar, A.S.M.A. Haseeb, Gas Sensors Based on One Dimensional Nanostructured Metal-Oxides: A Review, *Sensors.* 12 (2012) 7207–7258. doi:10.3390/s120607207.

- [75] W. Chen, Q. Zhou, L. Xu, F. Wan, S. Peng, W. Zeng, Improved methane sensing properties of co-doped SnO₂ electrospun nanofibers, J. Nanomater. 2013 (2013) 4.
- [76] J.-K. Choi, I.-S. Hwang, S.-J. Kim, J.-S. Park, S.-S. Park, U. Jeong, Y.C. Kang, J.-H. Lee, Design of selective gas sensors using electrospun Pd-doped SnO₂ hollow nanofibers, Sens. Actuators B Chem. 150 (2010) 191–199. doi:10.1016/j.snb.2010.07.013.
- [77] S.-J. Choi, B.-H. Jang, S.-J. Lee, B.K. Min, A. Rothschild, I.-D. Kim, Selective Detection of Acetone and Hydrogen Sulfide for the Diagnosis of Diabetes and Halitosis Using SnO₂ Nanofibers Functionalized with Reduced Graphene Oxide Nanosheets, ACS Appl. Mater. Interfaces. 6 (2014) 2588–2597. doi:10.1021/am405088q.
- [78] J.-H. Lee, A. Katoch, S.-W. Choi, J.-H. Kim, H.W. Kim, S.S. Kim, Extraordinary Improvement of Gas-Sensing Performances in SnO₂ Nanofibers Due to Creation of Local *p* – *n* Heterojunctions by Loading Reduced Graphene Oxide Nanosheets, ACS Appl. Mater. Interfaces. 7 (2015) 3101–3109. doi:10.1021/am5071656.
- [79] Q. Qi, T. Zhang, L. Liu, X. Zheng, Synthesis and toluene sensing properties of SnO₂ nanofibers, Sens. Actuators B Chem. 137 (2009) 471–475. doi:10.1016/j.snb.2008.11.042.
- [80] D.-J. Yang, I. Kamienchick, D.Y. Youn, A. Rothschild, I.-D. Kim, Ultrasensitive and Highly Selective Gas Sensors Based on Electrospun SnO₂ Nanofibers Modified by Pd Loading, Adv. Funct. Mater. 20 (2010) 4258–4264. doi:10.1002/adfm.201001251.

- [81] Y. Zhang, X. He, J. Li, Z. Miao, F. Huang, Fabrication and ethanol-sensing properties of micro gas sensor based on electrospun SnO₂ nanofibers, *Sens. Actuators B Chem.* 132 (2008) 67–73.
doi:10.1016/j.snb.2008.01.006.
- [82] J. Oviedo, M.J. Gillan, Energetics and structure of stoichiometric SnO₂ surfaces studied by first-principles calculations, *Surf. Sci.* 463 (2000) 93–101.
- [83] V. Lantto, T.T. Rantala, T.S. Rantala, Atomistic understanding of semiconductor gas sensors, *J. Eur. Ceram. Soc.* 21 (2001) 1961–1965.
- [84] S. Deng, V. Tjoa, H.M. Fan, H.R. Tan, D.C. Sayle, M. Olivo, S. Mhaisalkar, J. Wei, C.H. Sow, Reduced Graphene Oxide Conjugated Cu₂O Nanowire Mesocrystals for High-Performance NO₂ Gas Sensor, *J. Am. Chem. Soc.* 134 (2012) 4905–4917. doi:10.1021/ja211683m.
- [85] Z.K. Horastani, S.M. Sayedi, M.H. Sheikhi, Effect of single wall carbon nanotube additive on electrical conductivity and methane sensitivity of SnO₂, *Sens. Actuators B Chem.* 202 (2014) 461–468.
- [86] Z. Karami Horastani, S.M. Sayedi, M.H. Sheikhi, Effect of single wall carbon nanotube additive on electrical conductivity and methane sensitivity of SnO₂, *Sens. Actuators B Chem.* 202 (2014) 461–468.
doi:10.1016/j.snb.2014.05.100.
- [87] J.S. Lee, O.S. Kwon, S.J. Park, E.Y. Park, S.A. You, H. Yoon, J. Jang, Fabrication of Ultrafine Metal-Oxide-Decorated Carbon Nanofibers for DMMP Sensor Application, *ACS Nano.* 5 (2011) 7992–8001.
doi:10.1021/nn202471f.

- [88] S. Mao, S. Cui, G. Lu, K. Yu, Z. Wen, J. Chen, Tuning gas-sensing properties of reduced graphene oxide using tin oxide nanocrystals, *J. Mater. Chem.* 22 (2012) 11009. doi:10.1039/c2jm30378g.
- [89] C. Marichy, P.A. Russo, M. Latino, J.-P. Tessonier, M.-G. Willinger, N. Donato, G. Neri, N. Pinna, Tin dioxide–carbon heterostructures applied to gas sensing: structure-dependent properties and general sensing mechanism, *J. Phys. Chem. C.* 117 (2013) 19729–19739.
- [90] B.-K. Min, S.-D. Choi, Undoped and 0.1 wt.% Ca-doped Pt-catalyzed SnO₂ sensors for CH₄ detection, *Sens. Actuators B Chem.* 108 (2005) 119–124.
- [91] R.K. Mishra, S.B. Upadhyay, A. Kushwaha, T.-H. Kim, G. Murali, R. Verma, M. Srivastava, J. Singh, P.P. Sahay, S. Hee Lee, SnO₂ quantum dots decorated on RGO: a superior sensitive, selective and reproducible performance for a H₂ and LPG sensor, *Nanoscale.* 7 (2015) 11971–11979. doi:10.1039/C5NR02837J.
- [92] P.A. Russo, N. Donato, S.G. Leonardi, S. Baek, D.E. Conte, G. Neri, N. Pinna, Room-Temperature Hydrogen Sensing with Heteronanostructures Based on Reduced Graphene Oxide and Tin Oxide, *Angew. Chem. Int. Ed.* 51 (2012) 11053–11057. doi:10.1002/anie.201204373.
- [93] Z. Wang, C. Zhao, T. Han, Y. Zhang, S. Liu, T. Fei, G. Lu, T. Zhang, High-performance reduced graphene oxide-based room-temperature NO₂ sensors: A combined surface modification of SnO₂ nanoparticles and nitrogen doping approach, *Sens. Actuators B Chem.* 242 (2017) 269–279. doi:10.1016/j.snb.2016.10.101.

- [94] A. Yang, X. Tao, R. Wang, S. Lee, C. Surya, Room temperature gas sensing properties of SnO₂/multiwall-carbon-nanotube composite nanofibers, *Appl. Phys. Lett.* 91 (2007) 133110. doi:10.1063/1.2783479.
- [95] C.B. Jacobs, M.J. Peairs, B.J. Venton, Review: Carbon nanotube based electrochemical sensors for biomolecules, *Anal. Chim. Acta.* 662 (2010) 105–127.
- [96] H. Qian, E.S. Greenhalgh, M.S. Shaffer, A. Bismarck, Carbon nanotube-based hierarchical composites: a review, *J. Mater. Chem.* 20 (2010) 4751–4762.
- [97] H. Song, L. Zhang, C. He, Y. Qu, Y. Tian, Y. Lv, Graphene sheets decorated with SnO₂ nanoparticles: in situ synthesis and highly efficient materials for cataluminescence gas sensors, *J. Mater. Chem.* 21 (2011) 5972–5977.
- [98] D. Li, Y. Xia, Electrospinning of Nanofibers: Reinventing the Wheel?, *Adv. Mater.* 16 (2004) 1151–1170. doi:10.1002/adma.200400719.
- [99] C.J. Luo, S.D. Stoyanov, E. Stride, E. Pelan, M. Edirisinghe, Electrospinning versus fibre production methods: from specifics to technological convergence, *Chem. Soc. Rev.* 41 (2012) 4708. doi:10.1039/c2cs35083a.
- [100] J. Doshi, D.H. Reneker, Electrospinning process and applications of electrospun fibers, *J. Electrostat.* 35 (1995) 151–160.
- [101] A. Frenot, I.S. Chronakis, Polymer nanofibers assembled by electrospinning, *Curr. Opin. Colloid Interface Sci.* 8 (2003) 64–75.
- [102] Z.-M. Huang, Y.-Z. Zhang, M. Kotaki, S. Ramakrishna, A review on polymer nanofibers by electrospinning and their applications in

- nanocomposites, *Compos. Sci. Technol.* 63 (2003) 2223–2253.
doi:10.1016/S0266-3538(03)00178-7.
- [103] A. Formhals, Process and apparatus for preparing artificial threads. US Patent, 1975504, 1934.
- [104] G. Taylor, Electrically driven jets, in: *Proc. R. Soc. Lond. Math. Phys. Eng. Sci.*, The Royal Society, 1969: pp. 453–475.
<http://rspa.royalsocietypublishing.org/content/313/1515/453.short>
(accessed May 22, 2017).
- [105] P.K. Baumgarten, Electrostatic spinning of acrylic microfibers, *J. Colloid Interface Sci.* 36 (1971) 71–79.
- [106] I. Hayati, A. Bailey, T.F. Tadros, Investigations into the mechanism of electrohydrodynamic spraying of liquids: II. Mechanism of stable jet formation and electrical forces acting on a liquid cone, *J. Colloid Interface Sci.* 117 (1987) 222–230.
- [107] B. Ding, E. Kimura, T. Sato, S. Fujita, S. Shiratori, Fabrication of blend biodegradable nanofibrous nonwoven mats via multi-jet electrospinning, *Polymer.* 45 (2004) 1895–1902.
- [108] S.A. Theron, A.L. Yarin, E. Zussman, E. Kroll, Multiple jets in electrospinning: experiment and modeling, *Polymer.* 46 (2005) 2889–2899.
- [109] A.L. Yarin, E. Zussman, Upward needleless electrospinning of multiple nanofibers, *Polymer.* 45 (2004) 2977–2980.
- [110] O. Jirsak, F. Sanetnik, D. Lukas, V. Kotek, L. Martinova, J. Chaloupek, A method of nanofibres production from a polymer solution using electrostatic spinning and a device for carrying out the method, WO2005024101 A1, 2005.

- <http://www.google.com/patents/WO2005024101A1> (accessed April 2, 2017).
- [111] M.S. Peresin, Y. Habibi, A.-H. Vesterinen, O.J. Rojas, J.J. Pawlak, J.V. Seppälä, Effect of moisture on electrospun nanofiber composites of poly (vinyl alcohol) and cellulose nanocrystals, *Biomacromolecules*. 11 (2010) 2471–2477.
- [112] A.L. Yarin, S. Koombhongse, D.H. Reneker, Bending instability in electrospinning of nanofibers, *J. Appl. Phys.* 89 (2001) 3018–3026.
- [113] M. Cloupeau, B. Prunet-Foch, Electrostatic spraying of liquids: main functioning modes, *J. Electrostat.* 25 (1990) 165–184.
- [114] Precision deposition of a nanofibre by near-field electrospinning (PDF Download Available), ResearchGate. (n.d.).
https://www.researchgate.net/publication/228436507_Precision_deposition_of_a_nanofibre_by_near-field_electrospinning (accessed May 22, 2017).
- [115] S.B. Warner, A. Buer, S.C. Ugbolue, G.C. Rutledge, M.Y. Shin, A fundamental investigation of the formation and properties of electrospun fibers, *Natl. Text. Cent. Annu. Rep.* (1998) 83–90.
- [116] Y.M. Shin, M.M. Hohman, M.P. Brenner, G.C. Rutledge, Electrospinning: A whipping fluid jet generates submicron polymer fibers, *Appl. Phys. Lett.* 78 (2001) 1149–1151.
- [117] D.H. Reneker, A.L. Yarin, H. Fong, S. Koombhongse, Bending instability of electrically charged liquid jets of polymer solutions in electrospinning, *J. Appl. Phys.* 87 (2000) 4531–4547.
- [118] S.V. Fridrikh, H.Y. Jian, M.P. Brenner, G.C. Rutledge, Controlling the fiber diameter during electrospinning, *Phys. Rev. Lett.* 90 (2003) 144502.

- [119] D.H. Reneker, I. Chun, Nanometre diameter fibres of polymer, produced by electrospinning, *Nanotechnology*. 7 (1996) 216.
- [120] J.M. Deitzel, J. Kleinmeyer, D.E.A. Harris, N.B. Tan, The effect of processing variables on the morphology of electrospun nanofibers and textiles, *Polymer*. 42 (2001) 261–272.
- [121] R. Jaeger, M.M. Bergshoef, C.M. Batle, Schö nher, H.; Vaneso, G, in: *J Macromol Symp*, 1998: pp. 141–150.
- [122] J.M. Deitzel, J.D. Kleinmeyer, J.K. Hirvonen, N.B. Tan, Controlled deposition of electrospun poly (ethylene oxide) fibers, *Polymer*. 42 (2001) 8163–8170.
- [123] C.J. Buchko, L.C. Chen, Y. Shen, D.C. Martin, Processing and microstructural characterization of porous biocompatible protein polymer thin films, *Polymer*. 40 (1999) 7397–7407.
- [124] S. Megelski, J.S. Stephens, D.B. Chase, J.F. Rabolt, Micro-and nanostructured surface morphology on electrospun polymer fibers, *Macromolecules*. 35 (2002) 8456–8466.
- [125] M. Srinivasarao, D. Collings, A. Philips, S. Patel, Three-dimensionally ordered array of air bubbles in a polymer film, *Science*. 292 (2001) 79–83.
- [126] X. Zong, K. Kim, D. Fang, S. Ran, B.S. Hsiao, B. Chu, Structure and process relationship of electrospun bioabsorbable nanofiber membranes, *Polymer*. 43 (2002) 4403–4412.
- [127] K.H. Lee, H.Y. Kim, Y.M. La, D.R. Lee, N.H. Sung, Influence of a mixing solvent with tetrahydrofuran and N, N-dimethylformamide on electrospun poly (vinyl chloride) nonwoven mats, *J. Polym. Sci. Part B Polym. Phys.* 40 (2002) 2259–2268.

-
- [128] N. Yamazoe, Y. Kurokawa, T. Seiyama, Effects of additives on semiconductor gas sensors, *Sens. Actuators*. 4 (1983) 283–289.
- [129] N. Yamazoe, New approaches for improving semiconductor gas sensors, *Sens. Actuators B Chem.* 5 (1991) 7–19.
- [130] C. Xu, J. Tamaki, N. Miura, N. Yamazoe, Grain size effects on gas sensitivity of porous SnO₂-based elements, *Sens. Actuators B Chem.* 3 (1991) 147–155.
- [131] S.R. Morrison, Mechanism of semiconductor gas sensor operation, *Sens. Actuators*. 11 (1987) 283–287.
- [132] C. Wang, L. Yin, L. Zhang, D. Xiang, R. Gao, Metal oxide gas sensors: sensitivity and influencing factors, *Sensors*. 10 (2010) 2088–2106.
- [133] M. Sadakane, T. Horiuchi, N. Kato, C. Takahashi, W. Ueda, Facile preparation of three-dimensionally ordered macroporous alumina, iron oxide, chromium oxide, manganese oxide, and their mixed-metal oxides with high porosity, *Chem. Mater.* 19 (2007) 5779–5785.
- [134] C. Yu, X. Dong, L. Guo, J. Li, F. Qin, L. Zhang, J. Shi, D. Yan, Template-free preparation of mesoporous Fe₂O₃ and its application as absorbents, *J. Phys. Chem. C*. 112 (2008) 13378–13382.

Chapter 3

Synthesis and characterization of heterostructures of Reduced Graphene Oxide/Tin Dioxide by drop-drying method

3.1 Introduction

Among metal oxide semiconductor gas sensors, tin dioxide (SnO_2) has been intensively studied for its advantages of high gas sensitivity, stability and fast response [1–3]. SnO_2 is an n-type semiconductor due to the oxygen vacancy defects on the surface, which serve as active sites for gas sensing to induce a high gas response. The addition of metallic particles such as palladium (Pd) or platinum (Pt) to SnO_2 has been reported to have increased gas sensitivity via chemical and electronic additive effects [4–6]. However, in general, metal oxide gas sensors have drawbacks, including a high operating temperature and high power consumption. To improve the conductivity of metal oxides, alternative additive materials such as reduced graphene oxide (RGO) have recently been explored for their advantages of high sensitivity, fast response and good conductivity [7–11]. As a frontier material, graphene is of particular interest in

applications such as solar cells and gas sensors due to its superior electrochemical properties. Graphene is a two-dimensional and single-layer sheet of sp^2 hybridised carbon atoms with zero band gap energy, which possesses superior electrical conductance. It demonstrates ambipolar effects, allowing the type of charge carrier to be tuned by adjusting the gate voltage. Moreover, graphene can be considered an ideal electrode material because of its large surface area, superior electrical conductance and fast electron transfer rate. The specific surface area of graphene is $\sim 2,600 \text{ m}^2/\text{g}$, about twice as large than that of carbon nanotubes (CNTs) [12]. Moreover, the widely open structure enables it to have a faster response than CNTs. Currently, gas sensors based on graphene-related materials are being intensively studied due to their high sensitivity, selectivity and fast response to a variety of gases [13]. However, the pristine form of graphene has been reported to have low gas sensitivity due to the lack of energetically favourable sites, such as defects or functional groups, to interact with gases [14].

Graphene oxide (GO), the oxidised form of graphene, contains abundant defect sites as well as oxygen functional groups on the graphitic plane [15]. A gas sensor based on GO has been reported to have a high gas response due to the presence of energetically favourable sites to interact with gases [16]. GO has further advantages over pristine graphene, including the ability to disperse in polar solvents such as water or alcohol due to the formation of hydrogen bonds between the solvent and the oxygen functional groups on GO. However, the defects and functional groups on GO also destroy the continuity of the ballistic transport of charge carriers on the graphitic plane [17]. Hence, GO is poorly conductive, which restrains its electrical applications. The reduction of GO could be achieved

by thermal reduction, microwave and UV irradiation, laser interference reduction and chemical reduction [18]. Gas sensors based on thermal reduction of GO in vacuum [19] and laser interference reduction [20] were shown to have high sensitivities with good conductivities at room temperature due to the removal of oxygen functional groups under these conditions. Chemical reductions of GO by different reducing agents have been reported in the development of sensors with various sensitivities towards different gases. For example, hydrazine hydrate is commonly used due to its strong reducing power [21,22]. However, it is highly toxic, and the focus has now shifted to producing RGO using less toxic and more environmentally friendly reagents such as sodium borohydride, L-ascorbic acid (vitamin C) and d-glucose [23–25]. The hybridisation of RGO with metal oxides such as SnO₂ has been reported to greatly increase the gas sensitivity at much lower operating temperatures [26–28] due to the high conductivity of RGO. For example, Mao et al. [26] fabricated SnO₂ nanocrystals by mini-arc reactor and deposition of it onto RGO by electrostatic force-directed assembly (ESFDA) process. The sensors were tested with NO₂ and NH₃ at room temperature. Lee and co-workers [27] fabricated SnO₂-RGO nanofibers by electrospinning and sensing towards NO₂ at the lowest temperature of 50°C. Mishra et al. [28] demonstrated SnO₂ quantum dots decorated with RGO sensing towards H₂ and LPG was operated at the lowest temperature of 150 °C. Besides SnO₂, RGO gas sensors were also reported to increase sensitivities by incorporating with TiO₂ [29], ZnO [30,31] and CuO [32] etc. However most operating temperatures of the sensors reported were still higher than room temperature, hence there is still large potential in developing room temperature gas sensing materials with high sensitivity. In addition to inducing good responsiveness, the addition of SnO₂ is

far more economical than the use of noble transition metals such as Pd or Pt. Hence, sensors based on heterostructures of RGO and SnO₂ are expected to have stronger and faster gas responses.

As different reducing agents produce forms of RGO with different gas-sensing properties, a promising approach is to search for an optimal reducing agent combining high electrical conductivity with a high gas response. In this work, GO obtained by the modified Hummers method was reduced by four agents: D-glucose, sodium borohydride, L-ascorbic acid and hydrazine hydrate. SnO₂ was then incorporated into the resulting RGO to further increase their room-temperature gas response and conductivity. The morphology, degree of reduction and crystallinity of the homostructures and heterostructures were characterised by SEM, Raman spectroscopy, FTIR spectroscopy and XRD. The resistance and methane response of the different composites were compared.

3.2 Experimental

3.2.1 Materials

Graphite flake (1000 mesh) was purchased from QingDao HuaTai Lubricant Sealing S&T Co. Ltd. D-glucose, sodium borohydride and L-ascorbic acid were purchased from Tianjin OuBoKai Chemical Industry. Hydrazine hydrate (80%), potassium permanganate were purchased from Tianjin Kernal Chemical Reagent Co., Ltd. Tin dioxide (50-70nm) and PVA (1788) were purchased from Aladdin Chemical Reagent Co., Ltd. Sodium nitrate was purchased from Tianjin ZhiYuan Chemical Reagent Co. Ltd. Sulfuric acid (95%) was purchased from Sigma

Aldrich. Hydrogen peroxide (35%) and hydrochloric acid (1N) were purchased from VWR International Ltd. All chemicals were used as received without further purification.

3.2.2 Preparation of GO

A schematic diagram of the preparation of the heterostructured RGO-SnO₂ composite is shown in Figure 3.1. First, GO was prepared using the modified Hummers method [33]. The following typical procedure was adopted: 1.0 g of graphite flakes (1,000 mesh) was mixed with 25 ml of concentrated sulphuric acid (96%, Sigma Aldrich) with vigorous stirring for 15 min. Then, 1.25 g of sodium nitrate was added to the suspension with vigorous stirring for 1 h. Then, 3.7 g of potassium permanganate was added to the suspension and stirred constantly for 3 h at the elevated temperature of 35 °C. During this process effervescence occurred and a dark brown slurry paste was formed. Then, 60 ml of icy water was added gradually to the slurry paste and stirred constantly until no bubbles evolved. The slurry paste turned light brown in colour. Then, the slurry paste was further diluted with 140 ml of icy water and stirred constantly until no bubbles evolved. Finally, 30 ml of hydrogen peroxide (35%) was added to the slurry paste and the colour immediately changed from light brown to bright yellow. The paste was then filtered and washed with a solution of 50 ml of D.I. water and 20 ml of hydrochloric acid (1N) three times. Finally, the filtered light brown cake was dried at 60°C overnight in an oven.

3.2.3 Preparation of RGO-SnO₂

The GO obtained was reduced in situ by d-glucose (G), sodium borohydride (B), l-ascorbic acid (A) and hydrazine hydrate (H) in separate experiments. Typically, 0.15 g of GO was dispersed in 15 ml of D.I. water with stirring for 1 h and sonication for 1 h. Then, 0.1 g of D-glucose (for example) was added to the suspension and stirred for 1 h with heating at 95 °C. Then, 0.6 g SnO₂ and 0.01 g polyvinyl alcohol (PVA) powders were added to the reduced suspension with vigorous stirring and heating at 95 °C for 30 min. A small amount of PVA was added as a binder and homogeniser to disperse the SnO₂ crystallites uniformly in the suspension. The same reduction procedure followed by an incorporation of SnO₂ was followed for the sodium borohydride, L-ascorbic acid and hydrazine hydrate. The RGO reduced by D-glucose, sodium borohydride, L-ascorbic acid and hydrazine hydrate was designated as R(G), R(B), R(A) and R(H), respectively. Gas sensors were fabricated by drop-drying the composite solutions onto a glass substrate (10 x 10 mm) with gentle heating at 120°C for 15 min. A pair of gold electrodes (10 x 2 mm) with a separation of 5 mm was sputtered onto the surfaces of the samples for sensor tests.

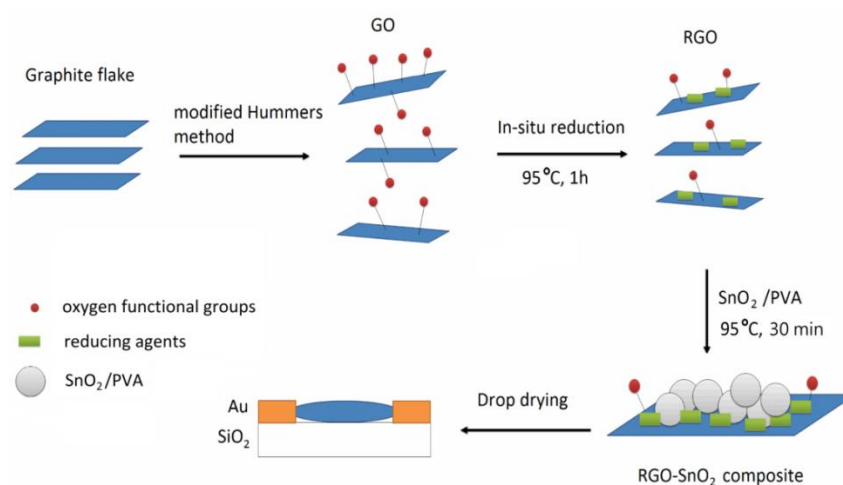


Figure 3.1 Schematic diagram for preparation of RGO-SnO₂ composite.

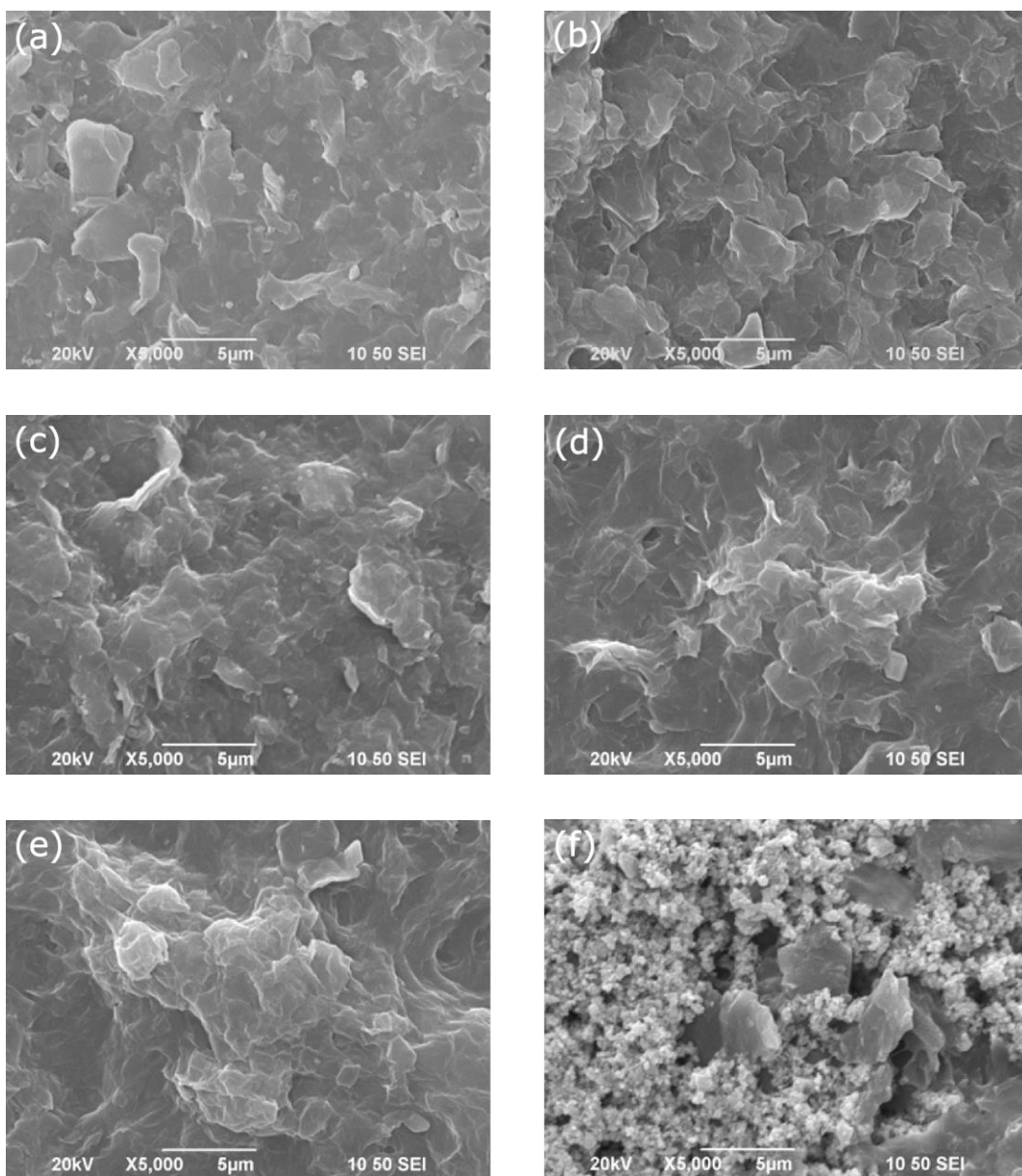
3.3 Results and discussion

The morphologies of samples were examined by Scanning Electron Microscope (200kV, JEOL Model JSM-6490). Raman spectrum was performed on Horiba LabRAM HR 800. The crystalline structures of samples were examined by X-ray Diffractometer on Rigaku SmartLab (9kW Rotating anode, Cu K α $\lambda=1.542$ Å). The functional compositions of samples were obtained by Fourier Transform Infrared Spectroscopy on Bruker Vertex-70 FTIR.

3.3.1 SEM analysis

SEM images of the homostructures of GO, R(G), R(B), R(A) and R(H) and all of the heterostructures with SnO₂ are shown in Figure 3.2. Figure 3.2 (a) shows that in the GO, stacked layers of GO platelets of different sizes were aggregated and randomly distributed over each other. Figure 3.2 (b) and (c) shows that the RGO platelets in R(G) and R(B) respectively were slightly aggregated than the GO platelets. Figure 3.2 (d) and (e) shows that the RGO platelets in R(A) and R(H) respectively were much more aggregated than GO, R(G) and R(B) platelets. This aggregation was due to the recovery of the π - π interaction between the graphitic planes after reduction by removing the electrostatically repelling oxygen functional groups on the GO [18]. Figure 3.2 (f) and (g) shows that dispersed SnO₂ nanocrystallites with sizes of 50–70 nm were uniformly distributed on the GO and R(G) platelets respectively. Figure 3.2 (h) shows that the composites of R(B) and SnO₂ were firmly aggregated, with a partially transparent film of PVA. Film-like structures could be formed by crosslinking PVA polymers via a solvolysis reaction between the borohydride and hydroxyl group of PVA [34,35].

However, the film-like structure of PVA was not favourable for gas sensing, as it screened the gas from passing into the sensing elements of the composites. Figure 3.2 (i) shows that the composites of R(A) and SnO₂ were more aggregated, with larger platelets, due to the greater degree of reduction of R(A). Figure 3.2 (j) shows that the composites of R(H) and SnO₂ were mostly stacked and aggregated, evidencing that hydrazine had the strongest reducing power of the tested reducing agents.



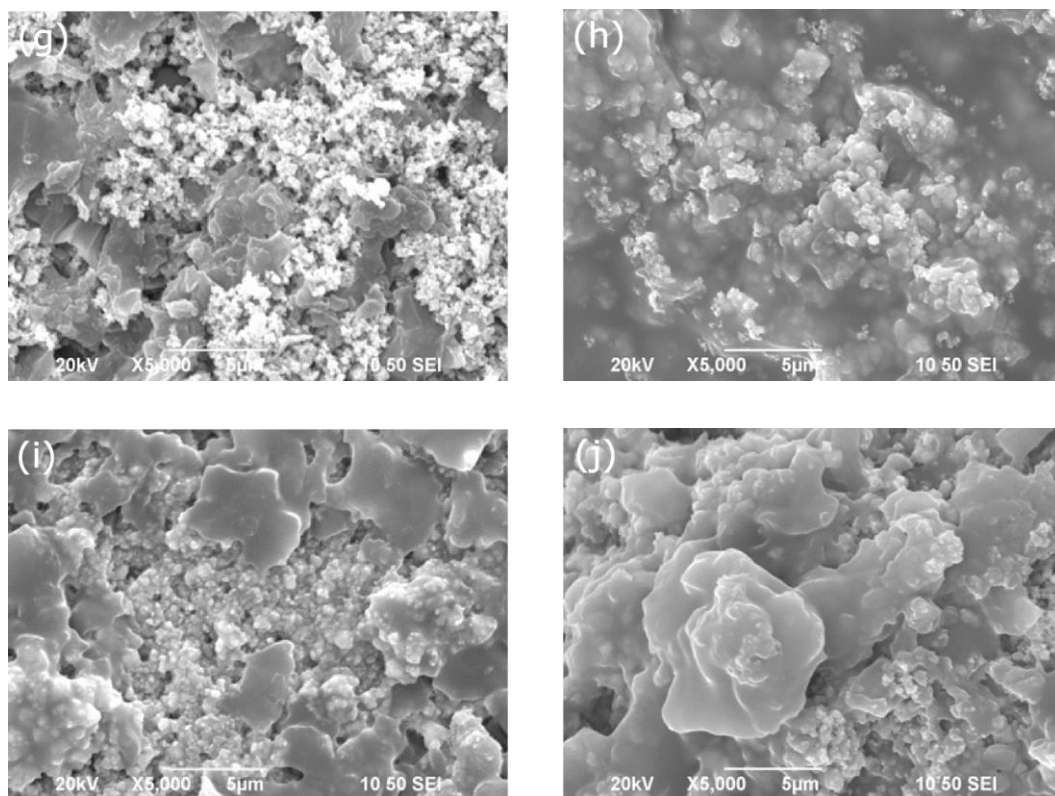


Figure 3.2 SEM images of homostructures (a) GO, (b) R(G), (c) R(B), (d) R(A), (e) R(H) and heterostructures (f) GO-SnO₂, (g) R(G)-SnO₂, (h) R(B)-SnO₂, (i) R(A)-SnO₂ and (j) R(H)-SnO₂.

3.3.2 Raman analysis

The degrees of reduction of the GO, R(G), R(B), R(A) and R(H) were elucidated by Raman spectroscopy, as shown in Figure 3.3. The characteristic vibrational D and G bands at $\sim 1,360$ and $\sim 1,590$ cm^{-1} , respectively, were observed in the GO and all of the RGO. The D band, representing a ‘defect’ signal, typically corresponds to the breathing-mode vibrations of the out-of-plane sp^3 carbon. The presence of a D band requires a breaking of the symmetry of the aromatic ring, as occurs in the sp^3 chair form of the ring or at edge sites. Hence, pristine graphite does not display this band. The G band, representing a pristine ‘graphitic’ signal,

corresponds to the stretching-mode vibrations of the in-plane sp^2 carbon. After the reduction of the GO, the intensity ratio of I_D/I_G increased from 0.91 for R(G) to 1.01 in the case of R(H). This increase in the D band signal relative to the G band was due to edge sites around the newly formed multiple sp^2 domains accompanying the removal of oxygen functional groups [36–38]. The edge sites around the newly formed sp^2 domains would induce asymmetric breathing-mode vibration which increases D band signal while the formation of multiple sp^2 domains broadens the signal of G band which increases the ratio of I_D/I_G . Hence, an increase in the intensity ratio I_D/I_G indicated an increased degree of reduction. Figure 3.3 shows that R(G) had the lowest degree of reduction ($I_D/I_G \sim 0.91$), while that of R(A) ($I_D/I_G \sim 0.97$) was slightly higher than R(B) ($I_D/I_G \sim 0.96$). R(H) had the highest degree of reduction ($I_D/I_G \sim 1.01$).

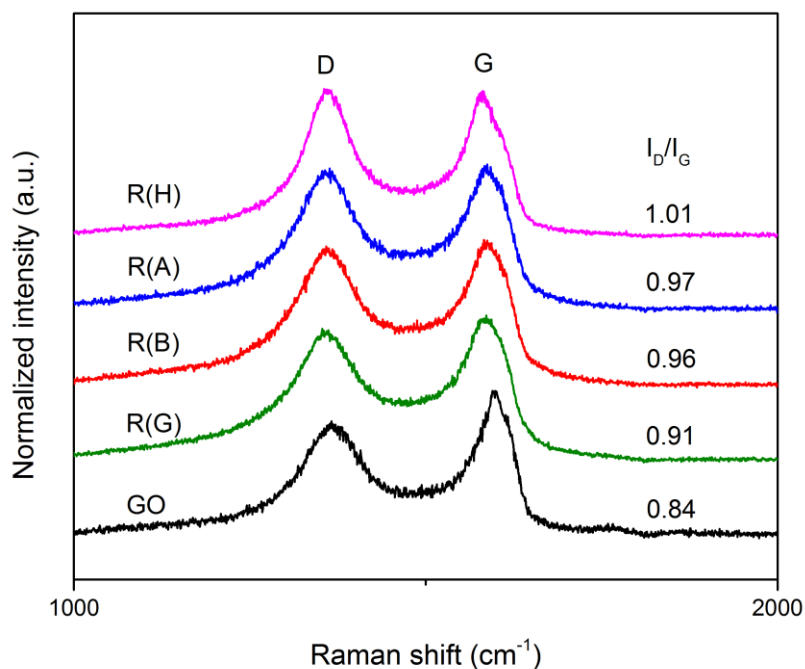


Figure 3.3 Raman spectra of GO, R(G), R(B), R(A) and R(H).

3.3.3 FTIR analysis

The functional-group compositions of the GO, R(G), R(B), R(A) and R(H) were elucidated by FTIR spectroscopy, as shown in Figure 3.4. Strong bands at $1,750\text{ cm}^{-1}$ (C=O), $1,280\text{ cm}^{-1}$ (C-O-C), $1,064\text{ cm}^{-1}$ (C-OH) and a broad band at $3,575\text{ cm}^{-1}$ (O-H) were all observed in the GO, indicating the presence of oxygen functional groups including carbonyl, epoxy, carboxylic and hydroxyl. R(G) showed characteristic signals with intensities similar to those of the GO, indicating that the reducing power of glucose against these oxygen functional groups was very weak. However, the signals were strongly attenuated in R(B), R(A) and R(H), indicating that sodium borohydride, ascorbic acid and hydrazine hydrate were more powerful reducing agents than glucose. R(B) displayed low-intensity but broad signals of hydroxyl groups (O-H and C-OH), indicating that sodium borohydride was weak in reducing these groups. R(B), R(A) and R(H) all featured a small peak at $1,621\text{ cm}^{-1}$, corresponding to C=C, indicating that the sp^2 domain became more populated upon reduction. The C=C bond signals in R(A) and R(H) were stronger than that in R(B), indicating a greater degree of reduction. The signal at $1,280\text{ cm}^{-1}$ (C-O-C) in the GO was up-shifted slightly to $1,336\text{ cm}^{-1}$ in R(A) and R(H) due to the increased sp^2 content. However, the epoxy group (C-O-C) signal at $1,336\text{ cm}^{-1}$ was stronger in R(A) than in R(B) and R(H), possibly due to the formation of dehydroascorbic acid (DHA) by the oxidation of ascorbic acid (A) after the reduction of the GO. The residual epoxy groups in DHA would thus have contributed to the relatively strong signal for C-O-C in R(A). The remaining oxygen functional groups, including carboxylic, epoxy and hydroxyl, were electron-withdrawing, allowing them to bind electron carriers at the surface, thus increasing the size of the space charge layer and the resistivity and gas

sensitivity [4]. These oxygen functional groups acted as active surface sites for the gases to attack, hence their effect on the resistance and gas response. The amount of oxygen functional groups remaining at the surface of the RGO after reduction was positively linked with their gas sensitivity (see the sensitivity tests in Section 5.2.1.2). Hence, R(G) and R(A) showed greater gas sensitivity than R(B) and R(H). However, R(A) showed a much higher degree of reduction than R(G), as discussed previously, indicating that ascorbic acid was the best reducing agent of the four candidates, having a higher reducing power as well as higher gas sensitivity.

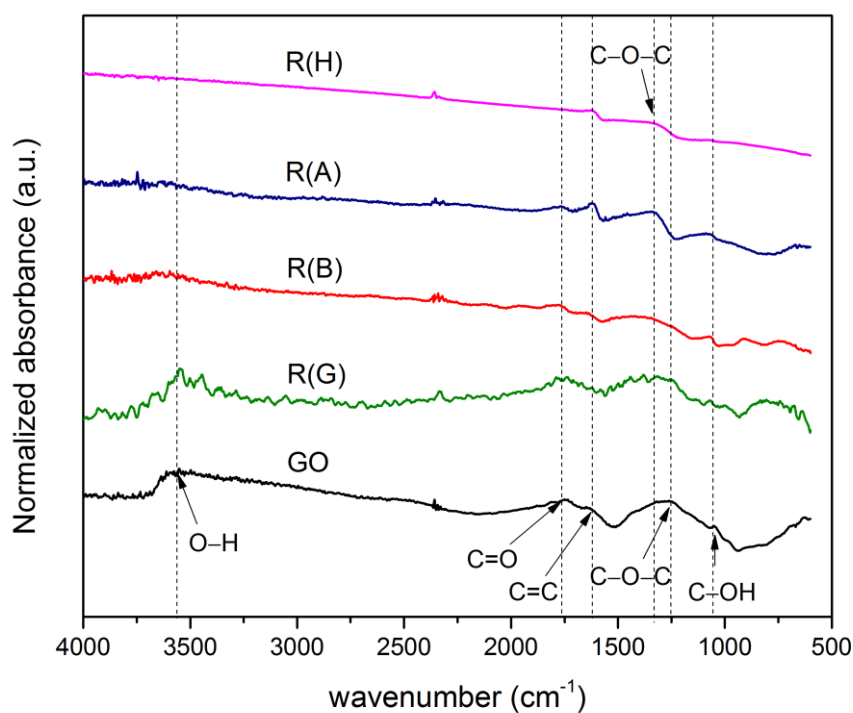


Figure 3.4 FTIR spectra of GO, R(G), R(B), R(A) and R(H).

3.3.4 XRD analysis

The crystalline structures of the GO, R(G), R(B), R(A) and R(H) and their heterostructures with SnO₂ were elucidated by XRD, as shown in Figure 3.5. An intense signal of GO(002) at 9.06° was observed in the GO, corresponding to a d-spacing of 9.75 Å, as shown in Figure 3.5 (a). The increased d-spacing of the GO compared with the typical value of 3.35 Å in graphite was caused by the mutually repelling oxygen functional groups intercalated between the graphitic planes in the GO. Amorphous signals of RGO(002) at 23.88°, corresponding to a d-spacing of 3.72 Å, were observed in R(G), R(B), R(A) and R(H) due to the recovery of the π - π interaction between the graphitic planes by removing the electrostatically repelling oxygen functional groups in the GO. The d-spacing of 3.72 Å was still larger than the typical value of 3.35 Å in pristine graphite due to the incomplete removal of functional groups between graphitic planes. The intensity of GO(002) became weaker while the amorphous RGO(002) signal became stronger as the degree of reduction increased. Comparison of the relative intensity of GO(002) and RGO(002) showed that the degrees of reduction were in ascending order of R(G), R(B), (A) and R(H). The slight shifts of GO(002) to smaller angles from 9.06° to 8.48° (d-spacing ~10.41 Å) in R(G) and 7.32° (d-spacing ~ 12.06 Å) in R(B) could have been due to the intercalation of glucose and borohydride molecules, respectively, between the expanded graphitic planes. The shift in R(B) to a smaller angle than in R(G) could have been due to the formation of a large complex polynuclear borate after hydrolysis of borohydride, further increasing the interplanar distance [35]. The shift of GO(002) to a smaller angle was not observed in R(A) and R(H) due to the stronger reducing power of ascorbic acid and hydrazine, such that the graphitic π - π interactions were strong enough to

inhibit the intercalation of molecules between graphitic planes.

The XRD spectra for the heterostructures of the GO, R(G), R(B), R(A) and R(H) with SnO₂ are shown in Figure 3.5 (b). The intense signals indicated by the indexes were caused by SnO₂ nanocrystallites. The strongest signal, at 26.58°, corresponds to the (110) plane, which is dominant in the SnO₂ crystalline structure. The lattice parameters of the tetragonal SnO₂ structure were determined as $a=b=4.739$ Å, $c=3.187$ Å by using high angle XRD planes of (220), (002), (310), (112), (301), (202) and (321) as shown in Figure 3.5 (b). The crystallite size (D) of SnO₂ could be deduced from Scherrer equation such that $D=0.9\lambda/(\beta\cos\theta)$, where λ is the Cu K α wavelength=1.542 Å, β is the full width at half maximum (FWHM) and θ is the Bragg angle. Therefore the crystallite sizes of SnO₂ were determined as 32.39, 32.04 and 29.51 nm for the dominant planes of (110), (101) and (211) respectively. The signal of GO(002) was shifted to the smaller angle of 6.94° in GO- SnO₂ compared with the pure GO (9.06°) due to the intercalation of SnO₂ nanocrystallites between graphitic planes. However, the signals of GO(002) and RGO(002) were absent in all of the RGO heterostructures after the incorporation of SnO₂, which could be attributed to (1) the strong graphitic π - π interaction in RGO, which inhibited the intercalation of SnO₂ nanocrystals, or (2) the disordered stacking of RGO sheets in the composites, as observed in other work [39].

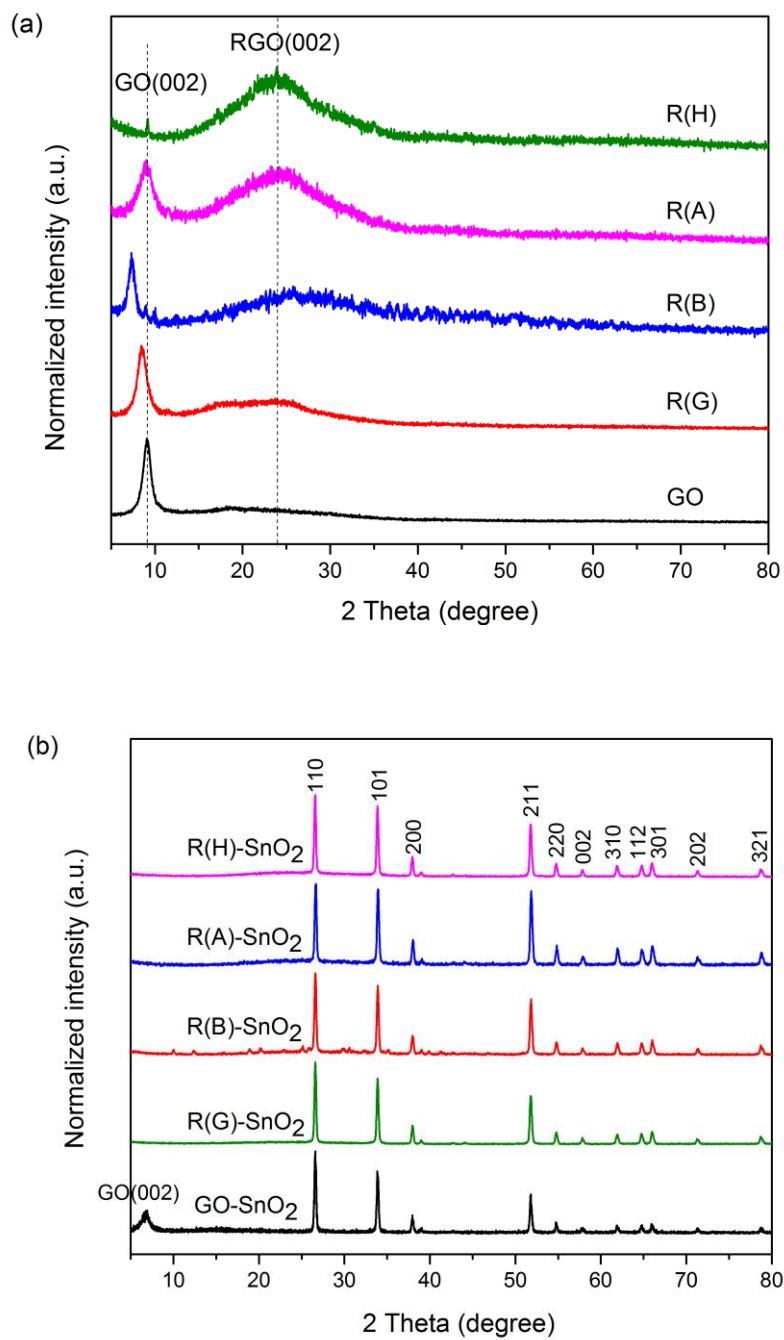


Figure 3.5 XRD spectra of (a) GO, R(G), R(B), R(A) and R(H); (b) GO-SnO₂, R(G)-SnO₂, R(B)-SnO₂, R(A)-SnO₂ and R(H)-SnO₂.

3.4 Conclusion

In this chapter, GO was fabricated by modified Hummers method, then in-situ

reduced by four reducing agents such as D-glucose, sodium borohydride, L-ascorbic acid and hydrazine hydrate. Finally, GO and all RGO were mixed together with SnO₂ in suspensions to form heterostructures. The morphology, degree of reduction and crystallinity of the homostructures and heterostructures were characterised by SEM, Raman spectroscopy, FTIR spectroscopy and XRD.

After the reduction of the GO, the intensity ratio of I_D/I_G in Raman spectrum were found to increase from 0.91 for R(G) to 1.01 in the case of R(H). The increase in the intensity ratio I_D/I_G indicated an increased degree of reduction in ascending order of R(G), R(B), R(A) and R(H).

In FTIR spectrum, all signals of oxygen functional group were found in descending order of R(G), R(B), R(A) and R(H) indicating that the reducing power increased from glucose (weakest) to hydrazine hydrate (strongest) which is consistent with the result from Raman spectrum.

The intensity of GO(002) signal became weaker while the intensity of amorphous RGO(002) signal became stronger as the degree of reduction increased as shown in the homostructure XRD spectrum. The typical signals of SnO₂ nanocrystallites were all found in the heterostructures with lattice parameters of $a=b=4.739 \text{ \AA}$ and $c=3.187 \text{ \AA}$ by using high angle XRD planes. While the crystallite sizes (D) of SnO₂ deduced from Scherrer equation were determined as 32.39, 32.04 and 29.51 nm for the dominant planes of (110), (101) and (211) respectively.

References:

- [1] J.F. McAleer, P.T. Moseley, J.O. Norris, D.E. Williams, Tin dioxide gas sensors. Part 1.—Aspects of the surface chemistry revealed by electrical conductance variations, *J. Chem. Soc. Faraday Trans. 1 Phys. Chem. Condens. Phases.* 83 (1987) 1323–1346.
- [2] J.F. McAleer, P.T. Moseley, J.O. Norris, D.E. Williams, B.C. Tofield, Tin dioxide gas sensors. Part 2.—The role of surface additives, *J. Chem. Soc. Faraday Trans. 1 Phys. Chem. Condens. Phases.* 84 (1988) 441–457.
- [3] J. Watson, The tin oxide gas sensor and its applications, *Sens. Actuators.* 5 (1984) 29–42.
- [4] N. Yamazoe, New approaches for improving semiconductor gas sensors, *Sens. Actuators B Chem.* 5 (1991) 7–19.
- [5] N. Yamazoe, Y. Kurokawa, T. Seiyama, Effects of additives on semiconductor gas sensors, *Sens. Actuators.* 4 (1983) 283–289.
- [6] S.R. Morrison, Mechanism of semiconductor gas sensor operation, *Sens. Actuators.* 11 (1987) 283–287.
- [7] J. Allen Matthew, C. Tung Vincent, B. Kaner Richard, Honeycomb carbon a review of graphene, *Chem Rev.* 110 (2010) 132–145.
- [8] E.V. Iski, E.N. Yitamben, L. Gao, N.P. Guisinger, Graphene at the Atomic-Scale: Synthesis, Characterization, and Modification, *Adv. Funct. Mater.* 23 (2013) 2554–2564.
- [9] D. Chen, H. Zhang, Y. Liu, J. Li, Graphene and its derivatives for the development of solar cells, photoelectrochemical, and photocatalytic applications, *Energy Environ. Sci.* 6 (2013) 1362–1387.

- [10] J.D. Fowler, M.J. Allen, V.C. Tung, Y. Yang, R.B. Kaner, B.H. Weiller, Practical chemical sensors from chemically derived graphene, *ACS Nano*. 3 (2009) 301–306.
- [11] T. Gan, S. Hu, Electrochemical sensors based on graphene materials, *Microchim. Acta*. 175 (2011) 1–19.
- [12] X. Li, H. Wang, J.T. Robinson, H. Sanchez, G. Diankov, H. Dai, Simultaneous nitrogen doping and reduction of graphene oxide, *J. Am. Chem. Soc.* 131 (2009) 15939–15944.
- [13] E. Llobet, Gas sensors using carbon nanomaterials: A review, *Sens. Actuators B Chem.* 179 (2013) 32–45.
- [14] W. Yuan, G. Shi, Graphene-based gas sensors, *J. Mater. Chem. A*. 1 (2013) 10078–10091.
- [15] D. Chen, H. Feng, J. Li, Graphene oxide: preparation, functionalization, and electrochemical applications, *Chem. Rev.* 112 (2012) 6027–6053.
- [16] K. Toda, R. Furue, S. Hayami, Recent progress in applications of graphene oxide for gas sensing: A review, *Anal. Chim. Acta*. 878 (2015) 43–53. doi:10.1016/j.aca.2015.02.002.
- [17] F. Schedin, A.K. Geim, S.V. Morozov, E.W. Hill, P. Blake, M.I. Katsnelson, K.S. Novoselov, Detection of individual gas molecules adsorbed on graphene, *Nat. Mater.* 6 (2007) 652–655.
- [18] S. Pei, H.-M. Cheng, The reduction of graphene oxide, *Carbon*. 50 (2012) 3210–3228.
- [19] A. Lipatov, A. Varezchnikov, P. Wilson, V. Sysoev, A. Kolmakov, A. Sinitskii, Highly selective gas sensor arrays based on thermally reduced graphene oxide, *Nanoscale*. 5 (2013) 5426. doi:10.1039/c3nr00747b.

- [20] L. Guo, H.-B. Jiang, R.-Q. Shao, Y.-L. Zhang, S.-Y. Xie, J.-N. Wang, X.-B. Li, F. Jiang, Q.-D. Chen, T. Zhang, H.-B. Sun, Two-beam-laser interference mediated reduction, patterning and nanostructuring of graphene oxide for the production of a flexible humidity sensing device, *Carbon*. 50 (2012) 1667–1673. doi:10.1016/j.carbon.2011.12.011.
- [21] X. Gao, J. Jang, S. Nagase, Hydrazine and thermal reduction of graphene oxide: reaction mechanisms, product structures, and reaction design, *J. Phys. Chem. C*. 114 (2009) 832–842.
- [22] S. Park, J. An, J.R. Potts, A. Velamakanni, S. Murali, R.S. Ruoff, Hydrazine-reduction of graphite-and graphene oxide, *Carbon*. 49 (2011) 3019–3023.
- [23] H.-J. Shin, K.K. Kim, A. Benayad, S.-M. Yoon, H.K. Park, I.-S. Jung, M.H. Jin, H.-K. Jeong, J.M. Kim, J.-Y. Choi, others, Efficient reduction of graphite oxide by sodium borohydride and its effect on electrical conductance, *Adv. Funct. Mater.* 19 (2009) 1987–1992.
- [24] M.J. Fernandez-Merino, L. Guardia, J.I. Paredes, S. Villar-Rodil, P. Solis-Fernandez, A. Martinez-Alonso, J.M.D. Tascon, Vitamin C is an ideal substitute for hydrazine in the reduction of graphene oxide suspensions, *J. Phys. Chem. C*. 114 (2010) 6426–6432.
- [25] C. Zhu, S. Guo, Y. Fang, S. Dong, Reducing sugar: new functional molecules for the green synthesis of graphene nanosheets, *ACS Nano*. 4 (2010) 2429–2437.
- [26] S. Mao, S. Cui, G. Lu, K. Yu, Z. Wen, J. Chen, Tuning gas-sensing properties of reduced graphene oxide using tin oxide nanocrystals, *J. Mater. Chem.* 22 (2012) 11009. doi:10.1039/c2jm30378g.

- [27] J.-H. Lee, A. Katoch, S.-W. Choi, J.-H. Kim, H.W. Kim, S.S. Kim, Extraordinary Improvement of Gas-Sensing Performances in SnO₂ Nanofibers Due to Creation of Local *p* – *n* Heterojunctions by Loading Reduced Graphene Oxide Nanosheets, *ACS Appl. Mater. Interfaces*. 7 (2015) 3101–3109. doi:10.1021/am5071656.
- [28] R.K. Mishra, S.B. Upadhyay, A. Kushwaha, T.-H. Kim, G. Murali, R. Verma, M. Srivastava, J. Singh, P.P. Sahay, S. Hee Lee, SnO₂ quantum dots decorated on RGO: a superior sensitive, selective and reproducible performance for a H₂ and LPG sensor, *Nanoscale*. 7 (2015) 11971–11979. doi:10.1039/C5NR02837J.
- [29] Z. Ye, H. Tai, T. Xie, Y. Su, Z. Yuan, C. Liu, Y. Jiang, A facile method to develop novel TiO₂/rGO layered film sensor for detecting ammonia at room temperature, *Mater. Lett.* 165 (2016) 127–130. doi:10.1016/j.matlet.2015.11.129.
- [30] J. Yi, J.M. Lee, W.I. Park, Vertically aligned ZnO nanorods and graphene hybrid architectures for high-sensitive flexible gas sensors, *Sens. Actuators B Chem.* 155 (2011) 264–269. doi:10.1016/j.snb.2010.12.033.
- [31] T.V. Cuong, V.H. Pham, J.S. Chung, E.W. Shin, D.H. Yoo, S.H. Hahn, J.S. Huh, G.H. Rue, E.J. Kim, S.H. Hur, P.A. Kohl, Solution-processed ZnO-chemically converted graphene gas sensor, *Mater. Lett.* 64 (2010) 2479–2482. doi:10.1016/j.matlet.2010.08.027.
- [32] S. Deng, V. Tjoa, H.M. Fan, H.R. Tan, D.C. Sayle, M. Olivo, S. Mhaisalkar, J. Wei, C.H. Sow, Reduced Graphene Oxide Conjugated Cu₂O Nanowire Mesocrystals for High-Performance NO₂ Gas Sensor, *J. Am. Chem. Soc.* 134 (2012) 4905–4917. doi:10.1021/ja211683m.

-
- [33] L. Shahriary, A.A. Athawale, Graphene oxide synthesized by using modified hummers approach, *Int J Renew Energy Env. Eng.* 2 (2014) 58–63.
- [34] R.F. Nickerson, Thickening of poly (vinyl alcohol) by borate, *J. Appl. Polym. Sci.* 15 (1971) 111–116.
- [35] R.K. Momii, N.H. Nachtrieb, Nuclear magnetic resonance study of borate-polyborate equilibria in aqueous solution, *Inorg. Chem.* 6 (1967) 1189–1192.
- [36] D. Luo, G. Zhang, J. Liu, X. Sun, Evaluation criteria for reduced graphene oxide, *J. Phys. Chem. C.* 115 (2011) 11327–11335.
- [37] J. Shen, Y. Hu, M. Shi, X. Lu, C. Qin, C. Li, M. Ye, Fast and facile preparation of graphene oxide and reduced graphene oxide nanoplatelets, *Chem. Mater.* 21 (2009) 3514–3520.
- [38] S. Stankovich, D.A. Dikin, R.D. Piner, K.A. Kohlhaas, A. Kleinhammes, Y. Jia, Y. Wu, S.T. Nguyen, R.S. Ruoff, Synthesis of graphene-based nanosheets via chemical reduction of exfoliated graphite oxide, *Carbon.* 45 (2007) 1558–1565.
- [39] H. Song, L. Zhang, C. He, Y. Qu, Y. Tian, Y. Lv, Graphene sheets decorated with SnO₂ nanoparticles: in situ synthesis and highly efficient materials for cataluminescence gas sensors, *J. Mater. Chem.* 21 (2011) 5972–5977.

Chapter 4

Synthesis and characterization of

Polyvinyl alcohol/Tin

dioxide/Graphene oxide nanofiber by

electrospinning method

4.1 Introduction

One dimensional metal oxide nanofibers are promising material in gas sensing due to the high surface area and porosity, which is most efficient in transducing gaseous interactions to electrical signal by directional carrier transport [1–6]. Tin dioxide (SnO_2) is non-toxic, low cost, easily accessible, n-typed with wide band-gap ($E_g = 3.6 \text{ eV}$) semi-conductor, have been reported to have high sensitivity and fast response to a number of gases due to the oxygen vacancies on surface after annealing which serves as active sites for gaseous interaction [7–12]. Accordingly, SnO_2 nanofiber gas sensors are promising material in gas sensing [4–6,13–21]. However, SnO_2 nanofiber gas sensors are usually operating at high temperatures making it less facile in miniature device application [4–6,13,17,19]. However only few efforts on heterostructures of SnO_2 nanofibers were reported to lower the operating temperature [14,20,21,16,18,15]. For example, Russo et al. [20]

fabricated nanocomposites of Pt- SnO₂/RGO by microwave assisted method and tested with hydrogen at the lowest temperature of 50 °C. Lee and co-workers [14] synthesized SnO₂ nanofiber with reduced graphene oxide (RGO) from electrospinning and tested with a number of gases at the lowest temperature of 50 °C. While limited works of gas sensors are reported to operate at room temperature. For example, Yang and co-workers [18] fabricated SnO₂ nanofiber with carbon nanotubes (CNTs) by electrospinning and tested the sensor with carbon monoxide. Lee et al. [15] synthesized PAN/PVP/ SnO₂/ZnO nanofiber and followed by carbonization and tested with DMMP gas. Hence there are still lots of rooms and potential in developing SnO₂ nanofiber gas sensor operating at low temperature.

Graphene consists of two-dimensional few layers of sp² aromatic carbon which has become a vibrant research topic over the decades due to the excellent mechanical and electrical properties that has many applications in sensors and electronics [22–26]. Recently, graphene derivative such as graphene oxide (GO) has become an interesting research with significant potential in applications of sensors, batteries and biomedical engineering due to the abundant oxygen functional groups. GO consists of few layers of graphite oxide which is usually produced by chemical oxidation of graphite with exfoliation process [27–29]. Meanwhile, the oxygen functional groups of hydroxyl, epoxy, carbonyl and carboxylic groups on basal planes or edges could serve as active sites for chemical interactions in gas sensors. The GO/ SnO₂ nanofiber could further enhance the sensing performance by the p-n junction effect [30,31]. However GO is poor conducting due to the electron-withdrawing oxygen functional groups bounding

the electrons at these sites which form a space charge layer on surface. Reduction of GO to RGO by chemical reduction and thermal reduction were reported to improve conductivity [32] by removing the electron-withdrawing functional groups. In chemical reduction, Stankovich et al. [33] was first reported to use hydrazine to chemically reduce GO. The highest conductivity of RGO reduced by hydrazine is 99.6 S/cm with C/O ratio of 12.5 [34]. Fernandez-Merino and co-workers [34] chemically reduced GO with vitamin-C which achieved a conductivity of 77 S/cm with C/O ratio of 12.5. In thermal reduction, Schniepp et al. [35] found that the C/O ratio of GO increased from 2.6/1 at room temperature to 9.7/1 at 1050 °C which indicated oxygen functional groups were gradually removed at higher temperatures. Wang and co-workers [36] annealed GO films under protective gas of Ar/H₂ to obtain 49, 93 and 550 S/cm at 500 °C, 700 °C and 1100 °C respectively which indicated the improved conductivity at higher annealing temperatures. RGO is more conducting but less p-typed than GO after thermal reduction as some residual oxygenated groups were not completely removed. The hybridisation of RGO with metal oxides such as SnO₂ has been reported to greatly increase the gas sensitivity at much lower operating temperatures [14,30,37] due to the high conductivity of RGO.

Electrospinning is a simple and versatile method of producing nanofibers from a precursor solution by applying high electrical voltage. It is widely used in the area of biomedical scaffolds, tissue engineering, filtration medium and batteries [38–42]. Although electrospinning process was first patent by Formhals in 1930s [43], it has become a vibrant topic for researchers since the works of Reneker and co-workers who evidencing the electrospinning of organic

nanomaterial in 1995 [40]. Recently, Jirsak et al. [44] described the needleless electrospinning by a roller spinning unit which generates jet streams from a liquid uploaded on a rotating roller. The setup was subsequently commercialized by Elmarco under the brand name of Nanospider in 2003. The needleless electrospinning improves the low production rate and the needle clogging problem as in conventional needle-type electrospinning. Schematic diagram of needleless electrospinning method was given in Figure 4.1. In the device, four thin wires are connected in a slowly rotating roller which is partially immersed in the precursor solution. The wires are charged at high voltage against the grounded collector held atop the roller. The solution loaded on the rotating wire would form many droplets and eventually Taylor cones as voltage keep increasing. When voltage increased to a critical value such that the electrostatic attraction between the droplet and the counter electrode is larger than the sum of the surface tension and gravitational force acting on the droplet, then fibers would be drawn upward from the droplet to the grounded collector.

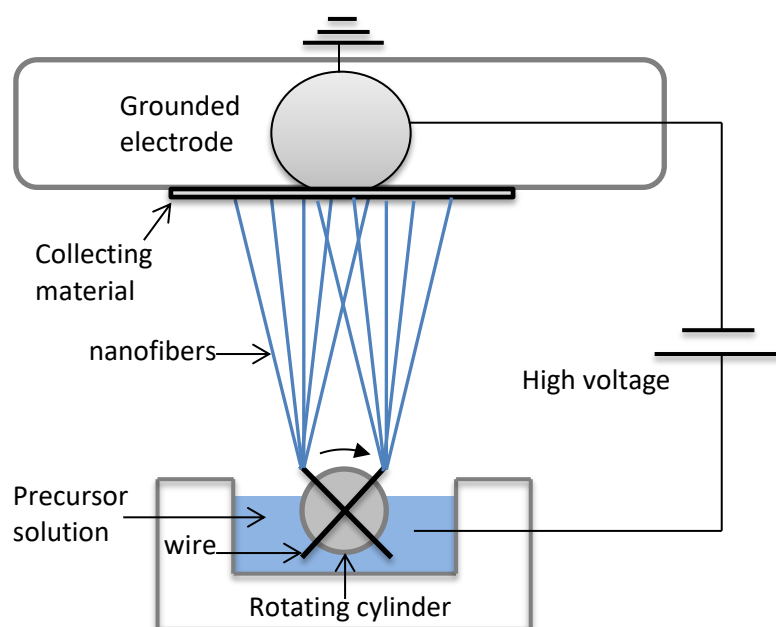


Figure 4.1 Schematic diagram of needleless electrospinning.

Among the polymers reported in electrospinning process, polyvinyl alcohol (PVA) is mostly used electrophilic polymer due to the high density of hydroxyl groups in polymer chain which makes it cross-linkable with GO to improve mechanical and thermal properties as applications in material filler, barrier film and biomedical engineering [45–48]. Here, we present a one-pot synthesis of PVA/SnO₂/GO nanofiber by electrospinning and subsequently carbonized in N₂ to achieve good conductivity at room temperature with high sensitivity. After carbonization, PVA and GO were pyrolysed to conducting carbon nanofibers with some residual oxygen functional groups. The improved thermal stability of PVA and GO by cross-linkage between the oxygen functional groups also increased the yield of carbon nanofiber after carbonization. The advantages of our work are facile and less expensive than most electrospun polyarylonitrile (PAN) carbon nanofibers [49–51] as PVA is much cheaper. The structural morphology, thermal properties, defect level, crystallinity and compositions of functional groups of the composite nanofiber would be characterized by SEM, TEM, TGA, Raman, XRD and FTIR spectroscopies. The resistance and gas sensitivities towards methane would also be tested.

4.2 Experimental

4.2.1 Materials

Graphite flake (1000 mesh) was purchased from QingDao HuaTai Lubricant Sealing S&T Co. Ltd. Dihydrate stannous chloride and polyvinyl alcohol (PVA, Mw ~ 105000) were purchased from Xilong Scientific Co., Ltd. Potassium permanganate were purchased from Tianjin Kernal Chemical Reagent Co., Ltd.

Sodium nitrate was purchased from Tianjin ZhiYuan Chemical Reagent Co. Ltd. Sulfuric acid (95%) was purchased from Sigma Aldrich. Hydrogen peroxide (35%) and hydrochloric acid (1N) were purchased from VWR International Ltd. All chemicals were used as received without further purification.

4.2.2 Preparation of PVA nanofiber

Electrospinning precursor solutions were prepared by a series of different concentrations of polyvinyl alcohol (PVA, Mw ~ 105000) solutions of 2 wt%, 3 wt%, 4 wt%, 5 wt%, 6 wt%, 7 wt% and 8 wt%. For 2 wt% PVA concentration, 0.8 g PVA powder was dissolved in 40 ml deionized water with vigorous stirring at 95 °C for 2 h. The preparations of other PVA concentrations follow the same procedure. The precursor solutions of PVA were electrospun to composite nanofibers using roller electrospinning method at voltage of 75 kV and roller-collector distance of 150 mm. The nanofibers were electrospun upward onto glass substrates attached on aluminium foil at the grounded electrode. The as-spun PVA nanofibers of different concentrations were put in desiccator immediately after electrospinning.

4.2.3 Preparation of GO

GO was prepared by modified Hummers method [52]. Briefly, 25 ml of concentrated sulfuric acid was added to a beaker containing 1.0 g of graphite flakes (1000 mesh) and 1.25 g of sodium nitrate. The suspended mixture was vigorous stirring for 1 hour. Then 3.7 g of potassium permanganate was gradually added to the suspension and keep stirring for 3 h at 35 °C. Meanwhile bubbles

evolved and the suspended mixture became a brown slurry paste. Then 150 ml of icy water was gradually added to the slurry paste during which temperature would rise to about 90 °C. Keep stirring until no bubbles evolved. Then, 30 ml of hydrogen peroxide (35%) was added to the paste and the colour changed to brilliant yellow. After that, the paste was filtered and washed three times with 40 ml of D.I. water and 20 ml of HCl (1N). Finally, the filtered cake was dried in air at 70 °C in oven for one day.

4.2.4 Preparation of PVA/SnO₂/GO nanofiber

Electrospinning precursor solution was prepared by 5 wt% poly(vinyl) alcohol (PVA, Mw~105000) solution, mixing with SnCl₂·2H₂O powder and GO suspension. Typically, 2 g PVA powder was dissolved in 25 ml deionized water with vigorous stirring at 95 °C for 2 h. Then 4 g SnCl₂·2H₂O powder was added to the polymer solution with vigorous stirring at 95 °C for 15 min. A series of different concentrations of GO suspension was prepared by grinding (0.025 g, 0.05 g, 0.1 g and 0.2 g) GO into powders and suspended in 15 ml of deionized water following with vigorous stirring for 2 h and sonication for 2 h. The prepared GO suspension was added to the as-prepared PVA/ SnCl₂·2H₂O solution with vigorous stirring at 95 °C for 15 min. The precursor solution of PVA/ SnCl₂·2H₂O/GO was spun to composite nanofibers using roller electrospinning method at voltage of 75 kV and roller-collector distance of 150 mm. The nanofibers were spun upward onto glass substrates attached on aluminium foil at the grounded electrode. The as-spun composite nanofibers of different GO concentrations were put in desiccator immediately after electrospinning and

carbonized in N₂ at 400, 450, 500, 550, 600 and 650 °C for 1h at heating rate of 10 °C/min. The nanofiber turned from white to brown and finally black after carbonization which were designated with GO content with respect to PVA in precursor solutions as N0 (0 wt%), N1 (1.25 wt%), N2 (2.5 wt%), N3 (5 wt%) and N4 (10 wt%). A pair of gold electrodes (10 x 2 mm) with separation of 5 mm was sputtered on the surface of the composite nanofibers for sensor tests.

4.3 Results and discussion

The morphologies of samples were examined by Scanning Electron Microscope (200kV, JEOL Model JSM-6490) and Transmission Electron Microscope (JEOL Model JEM-2011). The thermal properties of samples were examined by Thermogravimetric analyser / Differential Scanning Calorimeter (Netzch STA 449C, Jupiter). Raman spectrum was performed on Horiba LabRAM HR 800. The crystalline structures of samples were examined by X-ray Diffractometer on Rigaku SmartLab (9kW Rotating anode, Cu K α λ =1.542 Å). The functional compositions of samples were obtained by Fourier Transform Infrared Spectroscopy on Bruker Vertex-70 FTIR.

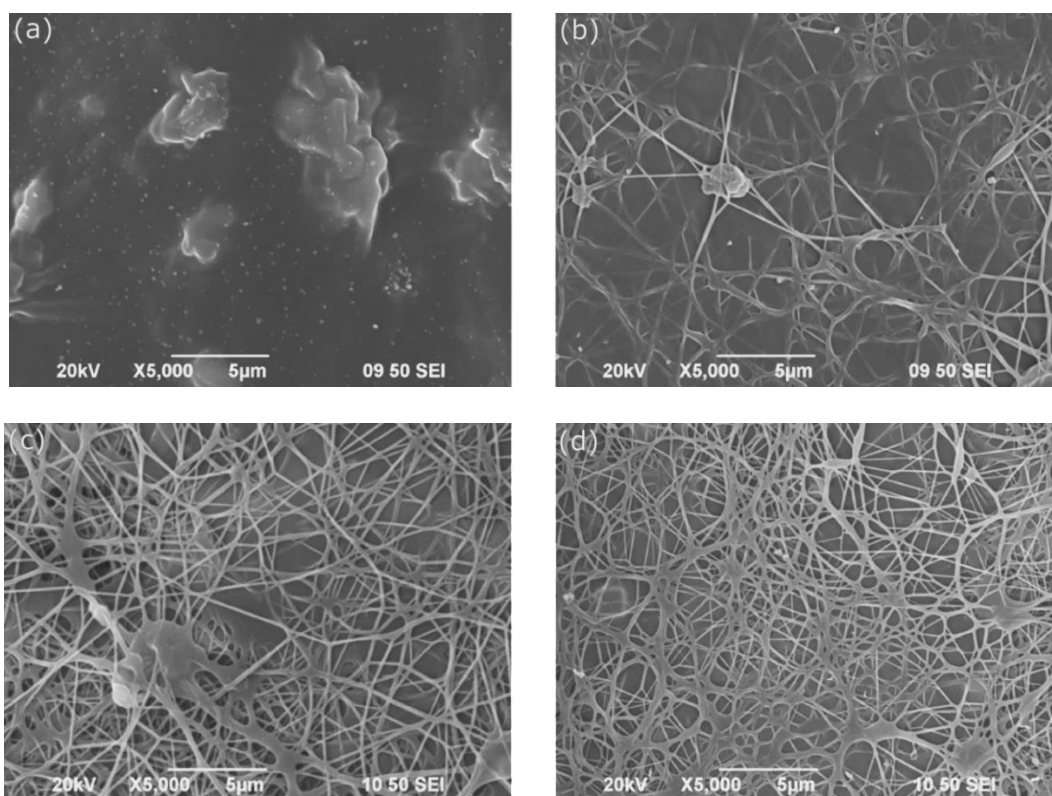
4.3.1 SEM analysis of pure PVA nanofiber

PVA nanofibers of 2 wt%, 3 wt%, 4 wt%, 5 wt%, 6 wt%, 7 wt% and 8 wt% concentrations were fabricated as shown in the SEM images of Figure 4.2 (a)-(g) respectively. The 2 wt% concentration could not be electrospun to fiber as viscosity was too low to against surface tension to form droplets rather a

continuous jet stream as shown in Figure 4.2 (a). Actually, electrospinning would not occur for concentration lower than a critical value no matter how large the voltage be applied. In this case, electrospinning corresponds for “droplet initiation” rather than “jet initiation” in concentration lower than the critical value to form fiber. For 3 wt% concentration as shown in Figure 4.2(b), the nanofibers were barely formed with beaded structure indicating that electrospinning began at this concentration. While the 4 wt% nanofibers were apparently denser than that of the 3 wt% as 4 wt% concentration was larger than the critical concentration to have jet initiation as shown in Figure 4.2 (c). However, the nanofibers were still formed with some beaded structures indicating that viscosity is not large enough to overcome the surface tension which tried to minimize surface area by forming beaded structures. The 5 wt% concentration nanofibers were uniform, smooth and beadless with smaller diameters as shown in Figure 4.2 (d). However, the nanofibers become thicker and denser for higher concentrations in 6 wt%, 7 wt% and 8 wt% as shown in Figure 4.2 (e)-(g) respectively.

Figure 4.3 (a)-(f) show the fiber diameter distributions of PVA nanofibers of 3 wt%, 4 wt%, 5 wt%, 6 wt%, 7 wt% and 8 wt% with average fiber diameters of 258, 239, 218, 322, 481 and 588 nm respectively by randomly selected 50 fibers for counting. By comparing the diameter size, it was shown that increasing concentrations from 3 wt% to 5 wt% would decrease slightly the diameter and the minimum diameter of 218 nm was obtained at 5 wt%. The diameters of the nanofibers decreased from 3 wt% to 5 wt% which could be due to the decrease of beaded structures as concentration increased. However, fiber diameters increased for increasing concentrations from 5 wt% to 8 wt% which could be due to the

reductions of periods of solvent evaporations during jet streaming process. Indeed, jet stream would be stretched and become thinner during solvent evaporation in the acceleration process of the jet travelling towards collector due to electrostatic repulsion of the charges along the axial direction of the jet. For higher concentration, the period of solvent evaporation reduced as the solvent to polymer ratio reduced which restrained the stretching motion of polymers due to electrostatic repulsion of the charges along the axial direction of the jet. Since the nanofiber of 5 wt% concentration has the minimum diameter with beadless structure, hence the composite nanofiber of PVA/SnO₂/GO would be prepared by using 5 wt% PVA precursor solution.



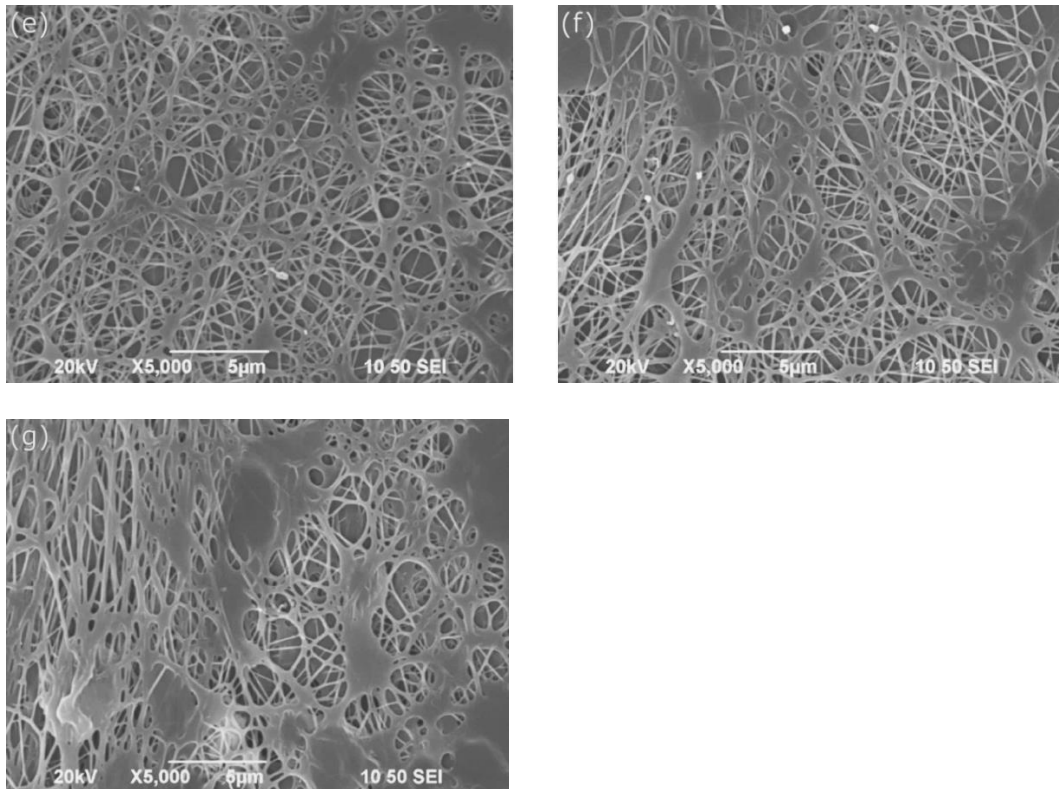
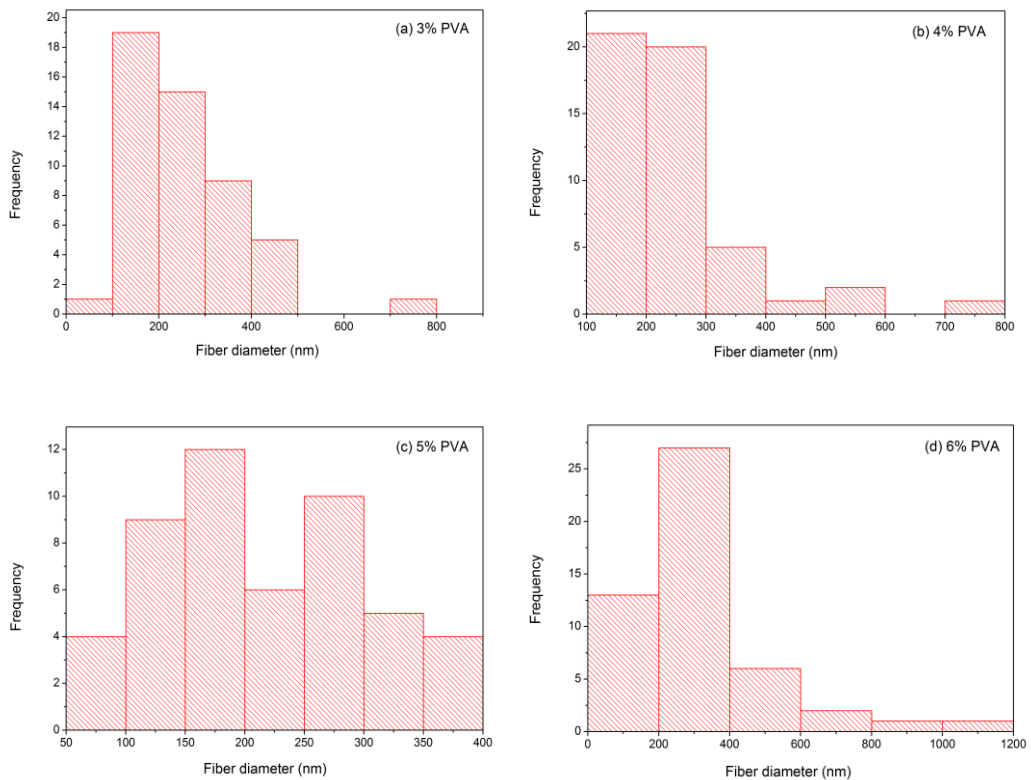


Figure 4.2 SEM images of (a) 2wt%, (b) 3wt%, (c) 4wt%, (d) 5wt%, (e) 6wt%, (f) 7wt% and (g) 8wt% PVA.



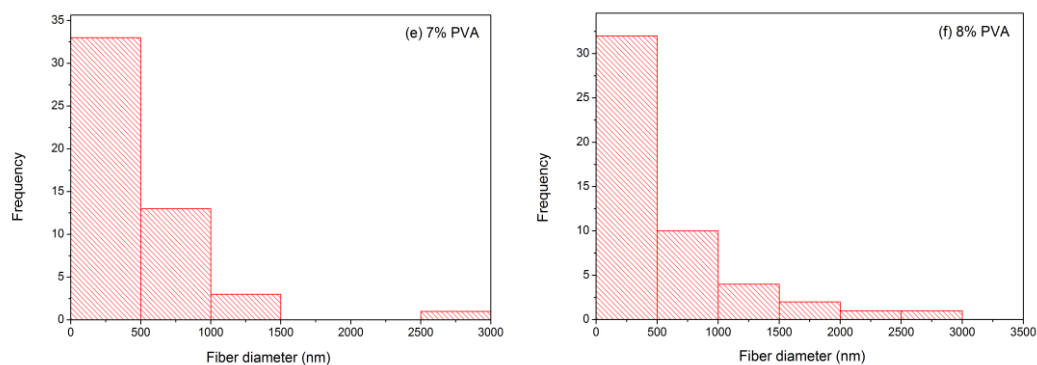


Figure 4.3 Fiber diameter distribution of (a) 2wt%, (b) 3wt%, (c) 4wt%, (d) 5wt%, (e) 6wt%, (f) 7wt% and (g) 8wt% PVA.

4.3.2 SEM analysis of PVA/SnO₂/GO composite nanofiber

PVA/SnO₂/GO nanofibers with different GO concentrations were successfully fabricated as shown in the SEM images of Figure 4.4. The nanofibers were uniform, smooth and bead-free with smaller diameters as GO content increased. Figure 4.5 (a)-(f) show the fiber diameter distributions of the composite nanofibers with average fiber diameters of 258, 243, 235, 236, 189 and 128 nm respectively by randomly selected 50 fibers for counting. By comparing the diameter size, it was shown that the composite nanofiber had smaller diameters with more GO content. This would be due to the increased viscosity and conductivity for more GO content which resulted as smaller diameter. The nanofiber morphology is generally determined by three factors (1) surface tension, (2) conductivity and (3) viscosity [38,53–56]. Surface tension tends to reduce the jet surface area by changing the straight jet into a spherical droplet. While conductivity controlled by charge density increases the elongation force of the jet by exerting electrical repulsion between the charges which decreases fiber

diameter. Viscosity tends to resist any rapid change of the shape of fiber by inertia. Hence a smooth and beadless fiber could be produced by increasing conductivity and viscosity against the surface tension of the fiber.

Adding more GO into the polymer composite would increase conductivity and viscosity which support the formation of a smooth and beadless nanofiber. However, the formation of thinner fiber with more GO content indicated the effect of conductivity was more significant than viscosity. Indeed, jet stream would be stretched and become thinner during solvent evaporation in the acceleration process of the jet towards collector due to electrostatic repulsion of the charges along the axial directional of the jet. Therefore the stretching motion of the jet would be reduced for higher viscosity due to larger inertia, which increased the fiber diameter. On the contrary, increasing conductivity accompanied with increasing charge density, which would increase the electrostatic repulsion of the charges inside the jet, and hence increasing the stretching motion along the axial direction of the jet which decrease the fiber diameter. These two competitive factors work against each other which resulted with a decrease in fiber diameter indicating that the effect of conductivity was more significant than that of viscosity with more GO content.

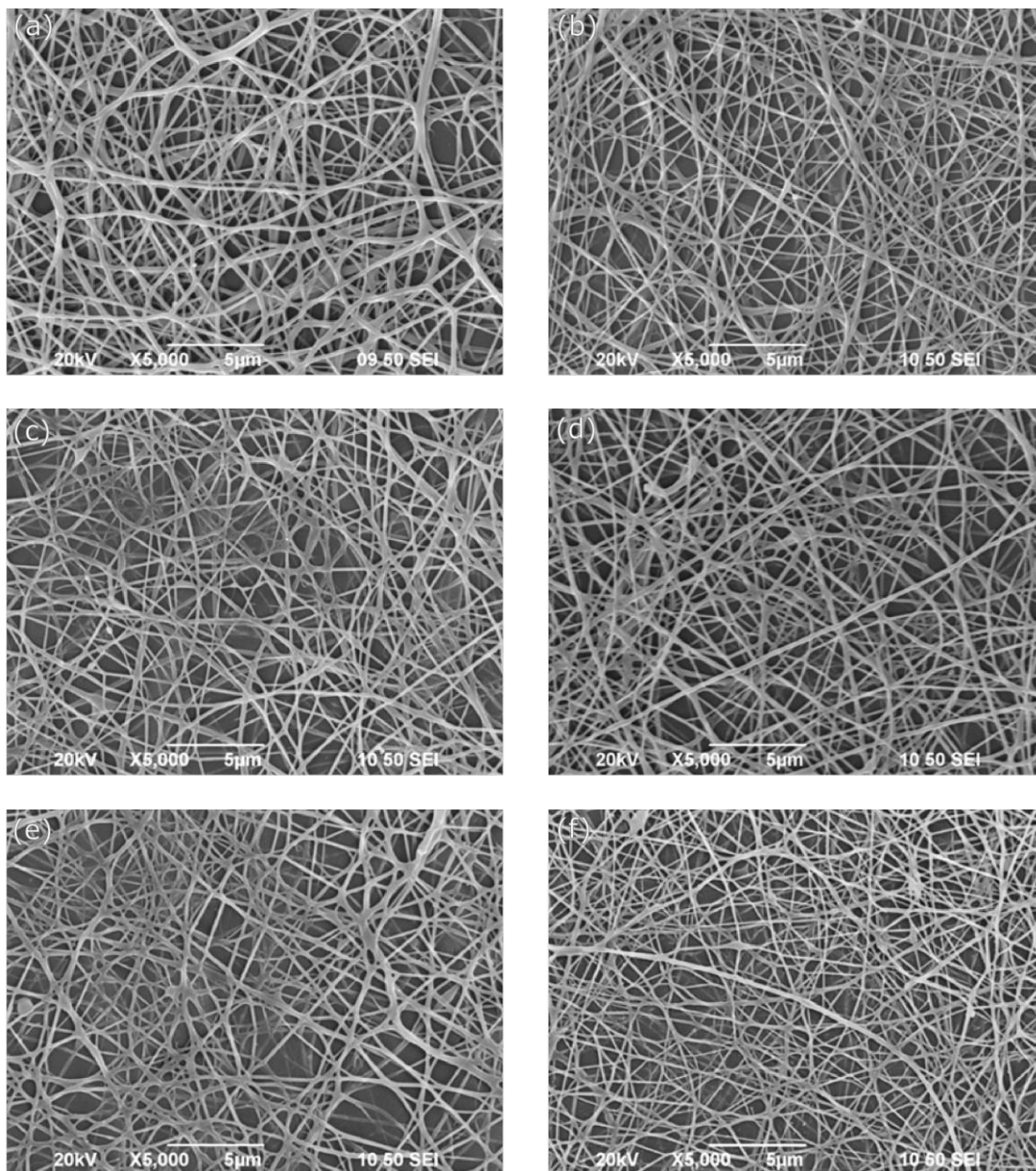


Figure 4.4 SEM images of (a) N0, (b) N1, (c) N2, (d) N2 (before carbonization), (e) N3 and (f) N4.

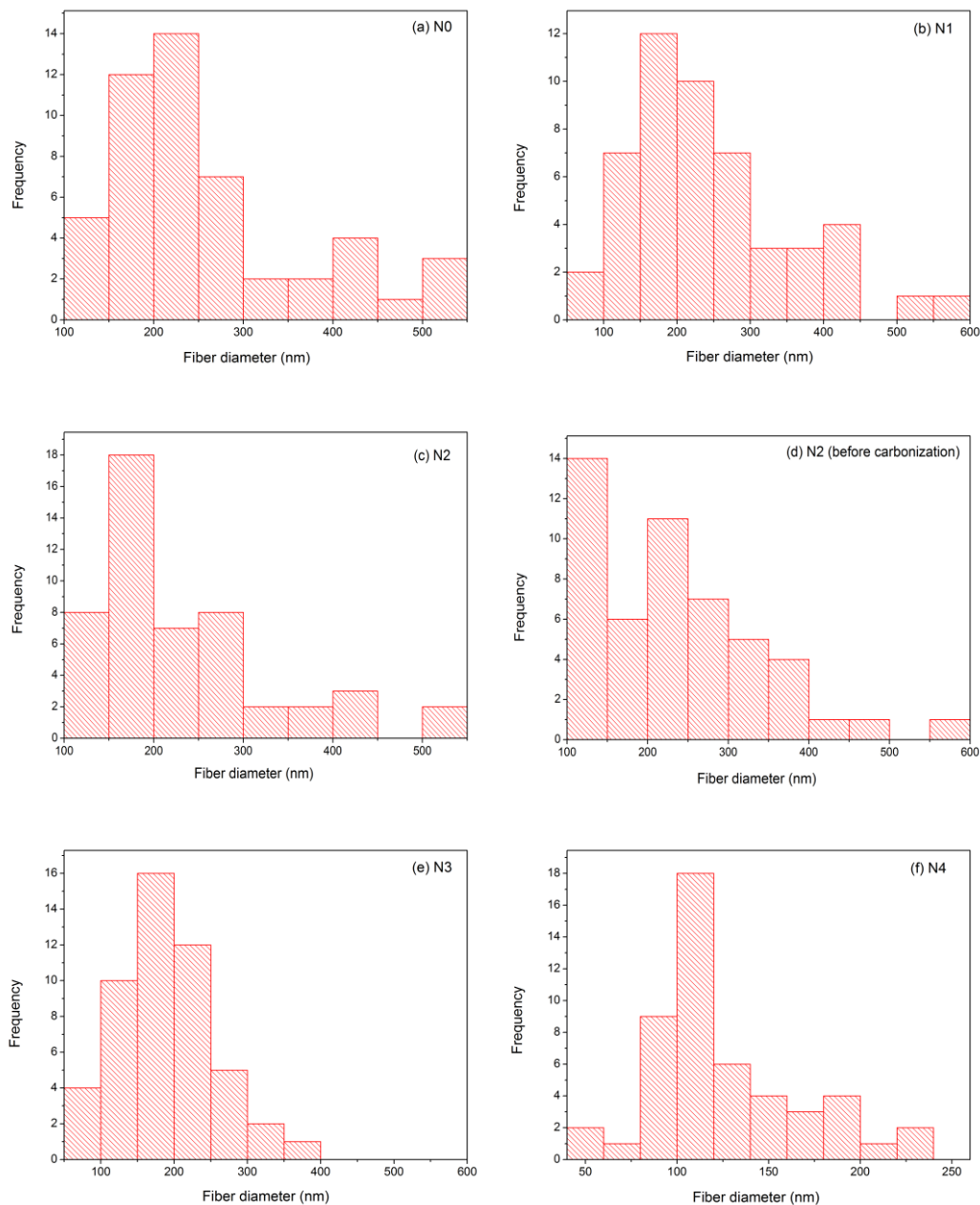


Figure 4.5 Fiber diameter distribution of (a) N0, (b) N1, (c) N2, (d) N2 (before carbonization), (e) N3 and (f) N4.

4.3.3 TEM analysis

Representative TEM images of N0, N1 and N3 after carbonization at 550 °C in N₂

are shown in Figure 4.6. We could observe that the composite nanofibers are uniform in size and shape with SnO₂ nanocrystallites aggregated on surface. The diameter of the nanofiber of N3 is smallest as shown in Figure 4.6 (c) which was confirmed by SEM images due to more GO content. The composite nanofiber N0 without GO content formed with a core-shell structure as shown in Figure 4.6 (a) as contrast difference is obviously observed between the core and shell of the nanofiber. The SnO₂ nanocrystallites form a uniform and dense layer on the shell to cover the PVA core. The formation mechanism of the core-shell structure could be attributed to phase separation [5,57–61] of PVA and Sn precursors due to rapid solvent evaporation during electrospinning and Kirkendall effect [61–66] during carbonization such that they are well studied theoretically and experimentally to be generally accepted for the formation of the core-shell nanofiber. For example, A. J. Guenther et al [57] explained the skin-layered formation on nanofiber surface is due to solvent evaporation by using a combination of Cahn-Hilliard (CH) time-evolution equation and Fick's law. M. Wei and co-workers [58] found that the rapid solvent evaporation together with high molecular mobility were crucial for the formation of core-shell structures. They also found that the composition with higher viscosity was always located at the center and the composition with lower viscosity located outside. On the other hand, X. Xia et al [61] confirmed the core-shell nanofiber formation by Kirkendall effect by examining TEM images of the nanofibers at different calcination temperatures. Y. Yin and co-workers [62] confirmed the formation of hollow nanocrystals through Kirkendall effect by examining TEM images of cobalt oxide at different times of calcination. Hence during electrospinning, the high surface tension of PVA tends to wrap it into core, while Sn precursors were diffused outward to the surface of

the jet stream which is driven by the evaporation of solvents during electrospinning. During carbonization, Sn precursors were diffused outward to the surface of nanofiber which is driven by the concentration gradient when SnO₂ was formed on surface. Pores and voids were found on the surface of N1 and N3 nanofibers with GO content as shown in Figure 4.6 (b) and (c). The nanofiber structures in N1 and N3 completely changed from core-shell to porous with addition of GO which could be due to the immobilization effect of GO in stabilization of the Sn precursors from diffusion by the oxygen functional groups of GO during electrospinning and carbonization. The immobilization effect could be further enhanced by the cross-linkage effect between GO and PVA due to the oxygen functional groups. Similar immobilization effect with addition of GO were also demonstrated by other works [67–71]. For example, Ji et al [67] demonstrated GO as a sulfur immobilizer in rechargeable lithium/sulfur cells by the reactive functional groups on GO. Pham and co-workers [68] demonstrated a novel hybrid material of GO and cadmium sulfide quantum dots through immobilization between the materials by the functionalized groups. The HRTEM images of N0, N1 and N3 are shown in Figure 4.6 (d)-(f). The inter-planar distances of ~0.35 nm and ~0.26 nm were attributed to (110) and (101) planes of the rutile SnO₂ nanocrystallites as observed in N0, N1, and N3. The highlighted region in Figure 4.6(d) was identified as amorphous carbon pyrolysed from PVA in the core with some amorphous carbon diffused out to form a skin layer to cover the shell of SnO₂ nanocrystallites after carbonization. The amount of amorphous carbon in N3 was more than in N1 as GO content increased as shown in Figure 4.6 (e) and (f). However, the amorphous carbon layer in N1 and N3 were less than N0 which could be due to the reasons that the porous structures in N1 and N3

were advantageous to the decomposition of PVA and GO to volatile organic compounds due to less shielding as compared with the core-shell structure in N0.

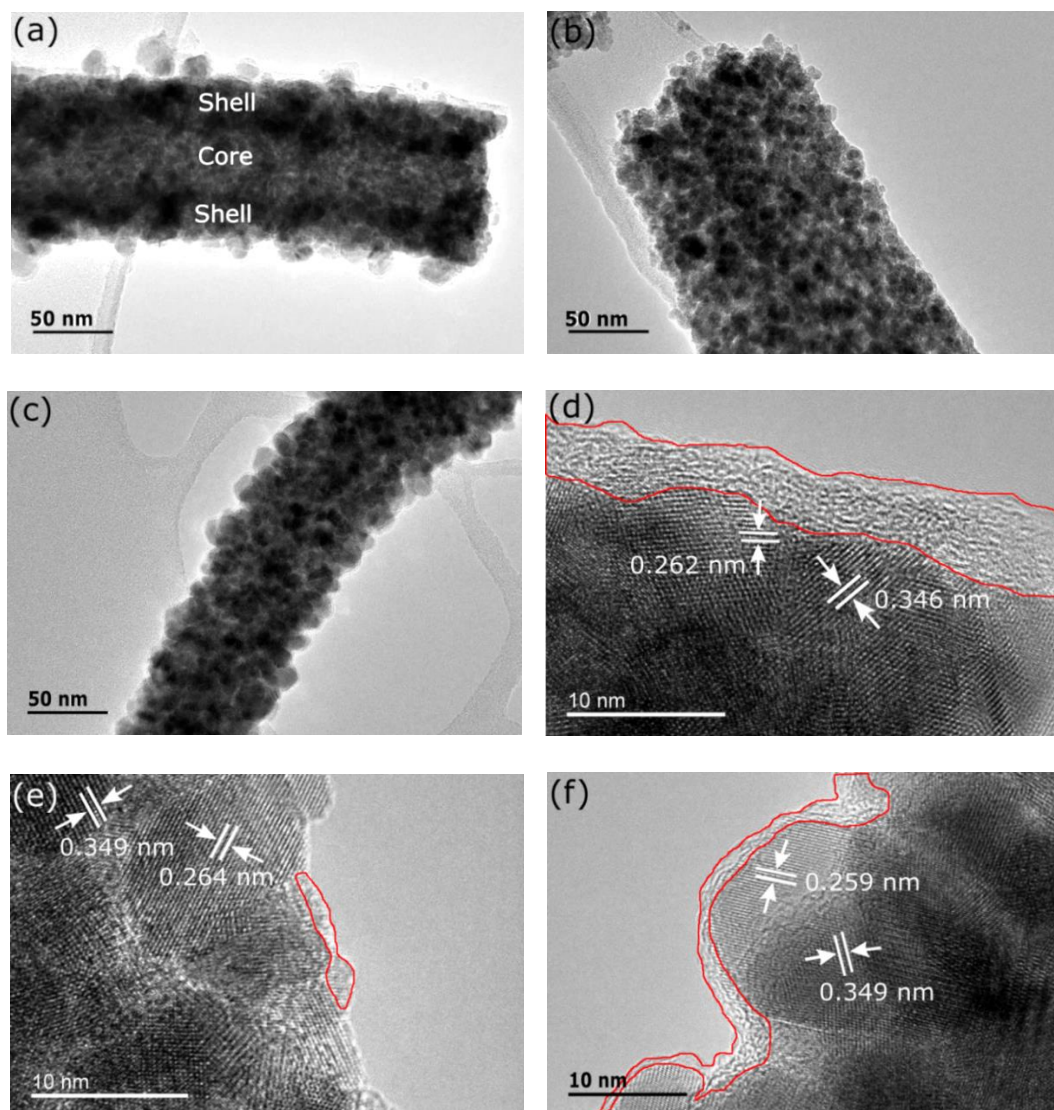


Figure 4.6 Representative TEM images of (a) N0, (b) N1 and (c) N3. HRTEM images of (d) N0, (e) N1 and (f) N3.

4.3.4 TGA analysis

Thermal properties of the composite nanofibers N0, N1, N2, N3 and N4 were elucidated by thermal gravimetric analysis (TGA) and differential thermal gravimetric analysis (DTG) under nitrogen as shown in Figure 4.7 (a) and (b)

respectively. There are three steps for the weight loss for all the composite nanofibers as shown in Figure 4.7 (a). The first weight loss around 179-226 °C was due to the decomposition of the labile oxygen functional groups in PVA or GO to H₂O or O₂. The first weight loss is largest for N0 and decreases for increasing GO content from N1 to N4 as shown in Figure 4.7 (a) which could be due to the increased thermal stability by the cross-linkage of GO and PVA. Comparing with the temperature for the first step of N0 at 194 °C as shown in Figure 4.7 (b), N1 and N2 have higher temperatures of 226 °C and 221 °C respectively. The increased temperatures could be due to the cross-linkage effect of GO and PVA. In contrast, N3 and N4 with more GO content lower the temperatures to 183 °C and 179 °C respectively, which could be due to the removal of the oxygen functional groups on the un-crosslinked GO in excessive amount. The second weight loss of N0 at 331 °C was due to the removal of the remaining oxygen functional groups of PVA and GO and the side chains of PVA. The third weight loss of N0 at 438 °C was due to the breakdown of the main carbon skeletons of PVA and GO. The second and third weight loss of N1 to N4 were at temperatures of ~410 °C and ~455 °C respectively which are higher than N0 as also reported by other works [72,45,73–75]. The increased temperatures for N1 to N4 at second step is much larger than that of the third step as the cross-linkage between PVA and GO has less effect in the main carbon skeletons than the sides chains with oxygen functional groups.

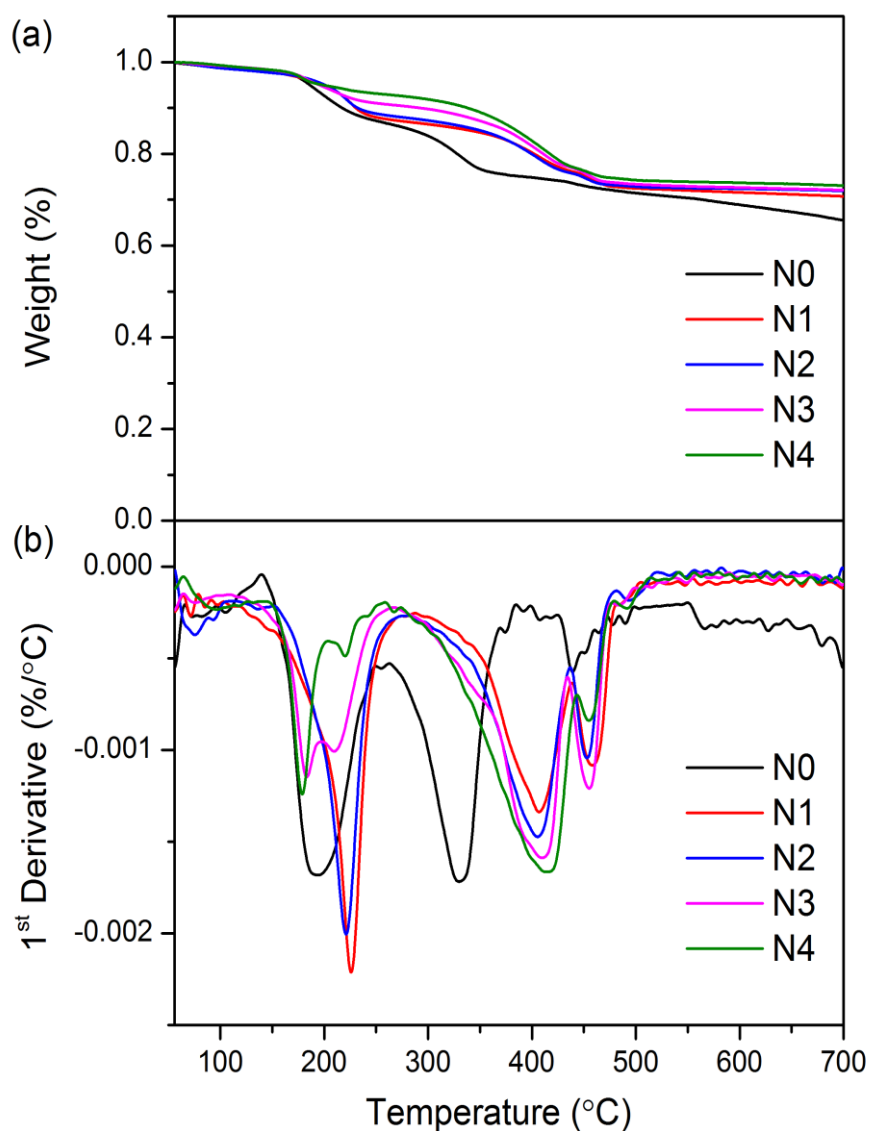


Figure 4.7 (a) TGA and (b) DTG spectra of the composite nanofibers.

4.3.5 Raman analysis

The Raman spectra of the composite nanofibers before and after carbonization are shown in Figure 4.8 (a) and (b) respectively. In Figure 4.8 (a), the characteristic peak at 2917 cm^{-1} of N0 corresponds to the stretching vibration of C-H in PVA. However, the peak is not observed in all composite nanofibers after addition of

GO in N1 to N4 which could be due to the coverage of nanofiber surface by GO as also reported in other work [76]. The characteristic vibrational G band at $\sim 1590\text{ cm}^{-1}$ were observed in all composite nanofibers after addition of GO. The broad band at $\sim 3060\text{ cm}^{-1}$ of N4 corresponds to the stretching vibration of $=\text{C-H}$ in GO. The small peak at $\sim 610\text{ cm}^{-1}$ is observed in all composite nanofibers corresponding to Sn-O. The characteristic D and G bands at ~ 1360 and $\sim 1590\text{ cm}^{-1}$ respectively are both observed in all composite nanofibers after carbonization as shown in Fig 4.8 (b). D band owing to defect signal corresponds to the stretching vibrations of the out-of-plane sp^3 carbon while G band owing to the pristine “graphitic” signal corresponds to the stretching vibrations of the in-plane sp^2 carbon [77,78]. The G bands were relatively higher in Fig 4.8 (b) than 4.8 (a) which could be due to the increased graphitic domain contributed from amorphous carbon after carbonization of PVA and GO. The ratio I_D/I_G was determined to decrease from 0.754 to 0.636 as GO content increased from N0 to N4. D band signal decreased relatively while G band signal increased with increasing GO content from N0 to N4 due to the increased amount of amorphous carbon after carbonization.

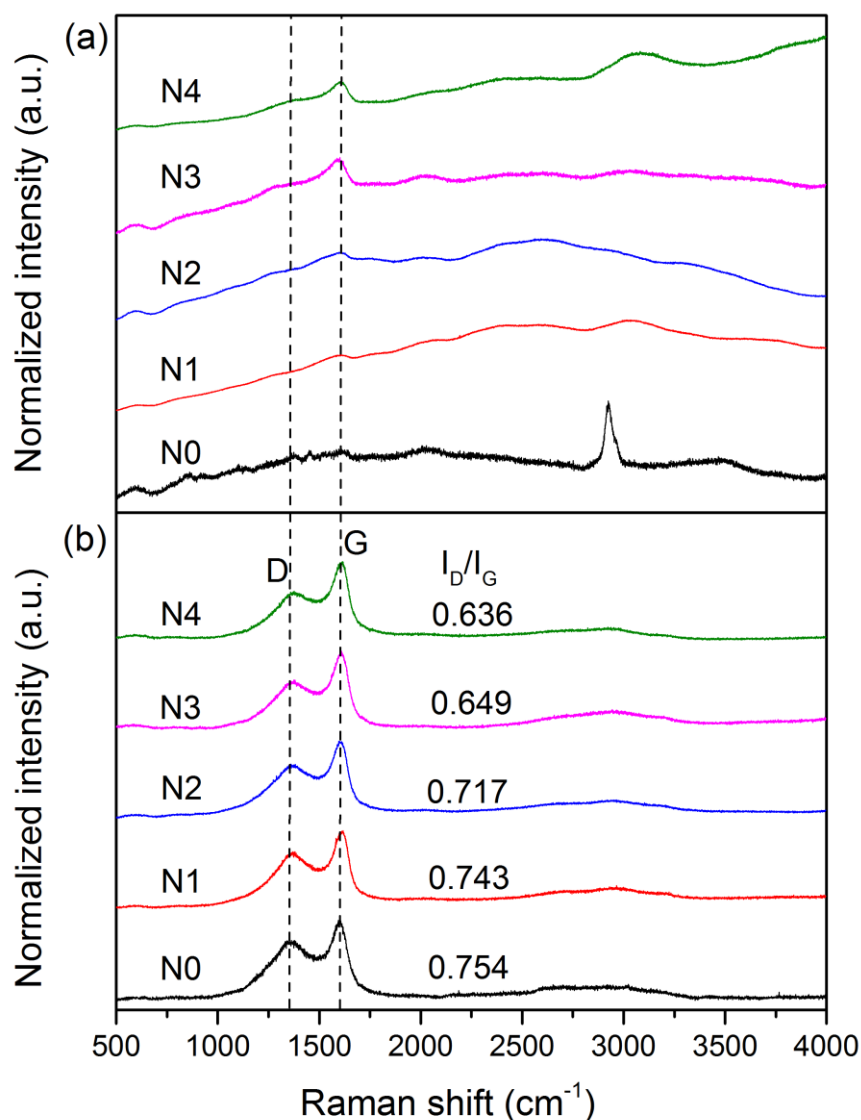


Figure 4.8 Raman spectra of the composite nanofibers of PVA/SnO₂/GO with different GO contents (a) before carbonization and (b) after carbonization.

4.3.6 XRD analysis

The crystalline structure of the composite nanofiber of PVA/SnO₂/GO before and after carbonization at different temperatures was elucidated by XRD spectra as shown in Figure 4.9. The small peak at 11.42° corresponding to the plane of GO

(002) is clearly observed in the composite nanofiber before carbonization. The peaks at 19.68° and 22.48° corresponding to the planes of (101) and (200) of PVA as it is a semi-crystalline polymer. After carbonization at 400°C , the dominant peaks of SnO_2 at 26.61° , 33.86° and 51.79° corresponding to the planes of (110), (101) and (211) respectively are weakly observed. The peaks are weak indicating the crystallization of the rutile structure of SnO_2 had begun at this temperature. The crystallization of the rutile structure of SnO_2 became more significant with increasing the carbonization temperatures as the peaks are sharper at higher temperatures. The lattice parameters of the rutile tetragonal SnO_2 after carbonization at 650°C were determined as $a=b=4.735\text{ \AA}$ and $c=3.185\text{ \AA}$ by using high angle planes of (220), (002), (310), (112), (301), (202) and (321) as shown in Figure 4.9. The crystallite size of SnO_2 could be determined by Scherrer equation $D = 0.9\lambda/(\beta\cos\theta)$, where λ is the Cu $K\alpha$ wavelength= 1.5418 \AA , β is the full width at half maximum (FWHM) and θ is the Bragg angle. The average crystallite sizes of SnO_2 were determined as 8.720, 6.270 and 7.614 nm for the dominant planes of (110), (101) and (211) respectively.

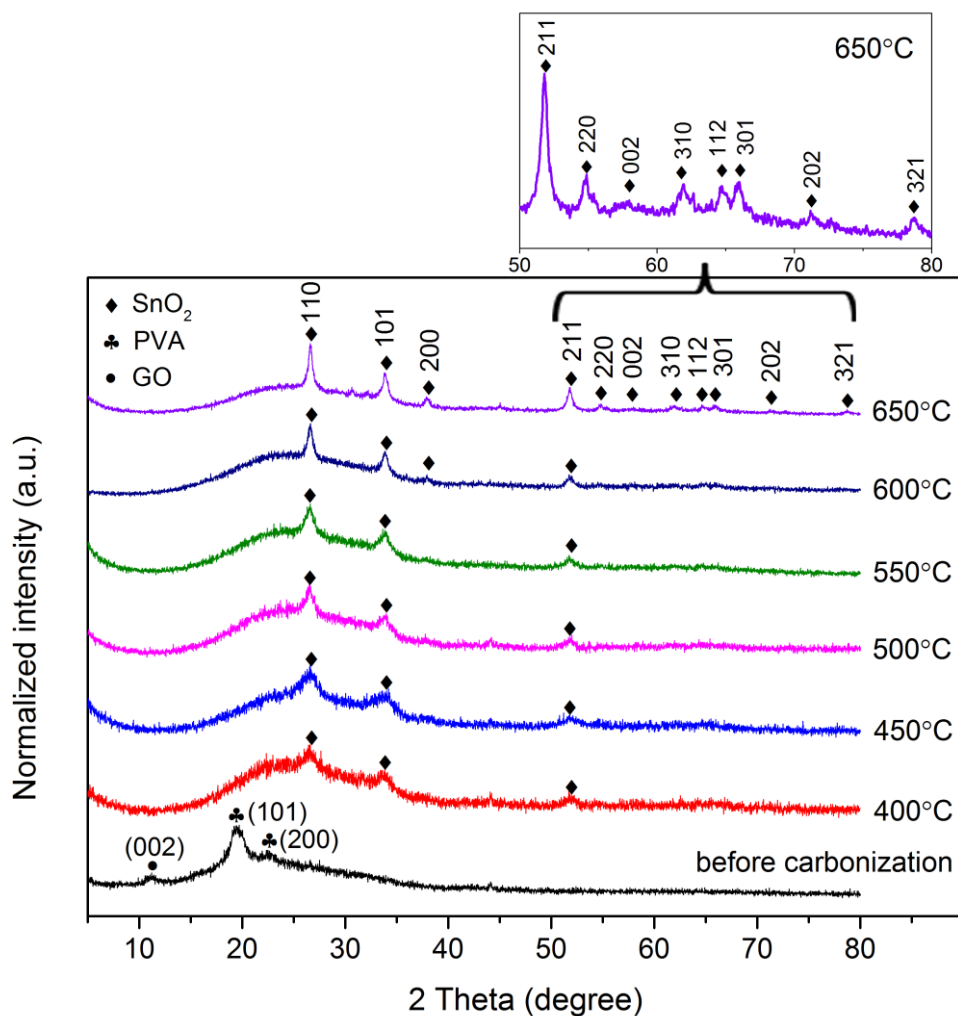


Figure 4.9 XRD spectra of the composite nanofibers of PVA/SnO₂/GO before and after carbonization at different temperatures.

4.3.7 FTIR analysis

The functional compositions of the nanofiber of PVA/SnO₂/GO before and after carbonization at different temperatures were elucidated by FTIR spectrum as shown in Figure 4.10. The strong bands at 1386 cm⁻¹ (C-O-C), 1587 cm⁻¹ (C=C), 1639 cm⁻¹ (C=O) and the broad band at 3399 cm⁻¹ (O-H) were all observed before carbonization indicating that the oxygen functional groups of epoxy, carbonyl, hydroxyl, carboxylic and aromatic groups were found in PVA and GO of the

composite nanofiber. The signals of oxygen functional groups were gradually decreased by increasing the carbonization temperatures and they were almost pyrolysed at 650 °C. While the thermal stability of aromatic group (C=C) in GO is higher than oxygen functional groups as it pyrolysed slowly and still show significant signal at 550 °C.

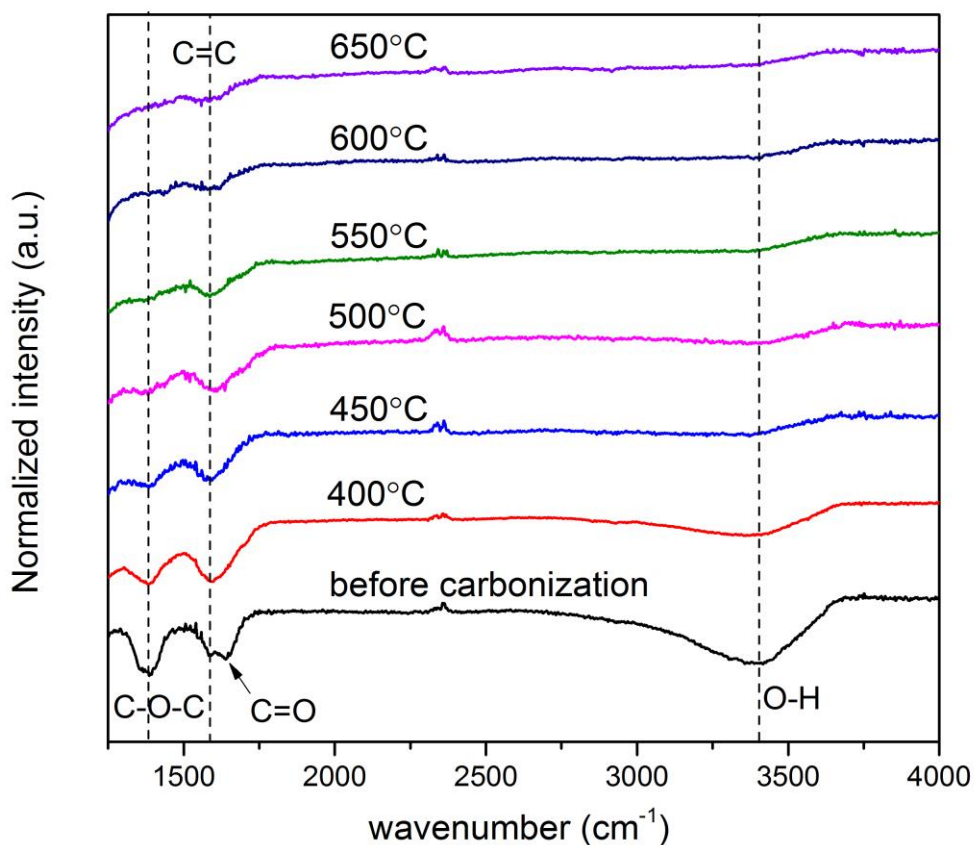


Figure 4.10 FTIR spectra of the composite nanofibers of PVA/SnO₂/GO before and after carbonization at different temperatures.

4.4 Conclusion

In this chapter, pure PVA nanofibers were fabricated by electrospinning using different PVA concentrations in precursor solutions. It was found that concentration that was too low or too high in precursor solutions could not form

uniform and beadless nanofibers with small diameters. For too low concentrations such as 2 wt% - 4 wt%, either there was no nanofibers formation or formation of nanofibers with beaded structures. While too high concentrations such as 6 wt% - 8 wt%, the nanofibers were formed with beadless structure but larger diameters. Therefore, the optimal PVA concentration was found at 5 wt% such that the nanofibers were uniform, smooth and beadless with smallest diameter of 218 nm.

PVA/SnO₂/GO nanofibers with different GO concentrations were successfully fabricated at 5 wt% PVA concentration. The nanofibers were uniform, smooth and beadless with smaller diameters as GO content increased. The average fiber diameters of N0 (0 wt%), N1 (1.25 wt%), N2 (2.5 wt%), N3 (5 wt%) and N4 (10 wt%) after carbonization were found as 258, 243, 235, 189 and 128 nm respectively by randomly selected 50 fibers for counting. Adding more GO into the polymer composite would increase conductivity and viscosity. However, the formation of thinner fiber with more GO content indicating the effect of conductivity was more significant than viscosity.

In TEM analysis, it was found that the composite nanofiber N0 without GO content formed with a core-shell structure with a continuous thin layer of amorphous carbon pyrolysed from PVA covering the shell of SnO₂ nanocrystallites after carbonization. While the nanofibers of N1 and N3 with GO content were formed with porous structure after carbonization with some discontinuous amorphous carbon residue on the nanofiber surface. Indeed, the core-shell structure of N0 could be attributed to the phase separation of PVA and Sn precursors during electrospinning and Kirkendall effect during carbonization

While the porous nanofiber structure of N1 and N3 could be due to the stabilization of Sn precursors by the oxygen functional groups of GO to diffusion during electrospinning and carbonization.

In TGA and DTG analysis, it was found that there were three steps for the weight loss for all the composite nanofibers. The first weight loss around 179-226 °C was due to the decomposition of the labile oxygen functional groups in PVA or GO. The second weight loss were found at around 331-410 °C which was due to the removal of the remaining oxygen functional groups of PVA and GO and the side chains of PVA. The third weight loss were found at around 438-455 °C which was due to the breakdown of the main carbon skeletons of PVA and GO. The thermal stability of the nanofibers were found to be increased with addition of GO due to interlinkage effect between GO and PVA as second and third weight loss temperatures were also increased. The increased thermal stability also increases the yield of nanofibers after carbonization.

In Raman spectrum, the characteristic D and G bands are both observed in all composite nanofibers after carbonization with a decrease of the ratio I_D/I_G from 0.754 to 0.636 as GO content increased from N0 to N4 which could be due to the increased amount of amorphous carbon by adding more GO after carbonization.

In XRD spectrum, the crystallization of the rutile structure of SnO₂ became more significant with increasing the carbonization temperatures as the peaks are sharper at higher temperatures. The lattice parameters of the rutile tetragonal SnO₂ after carbonization at 650 °C were determined as a=b=4.735 Å

and $c=3.185 \text{ \AA}$ by using high angle XRD planes. While the crystallite sizes of SnO_2 deduced from Scherrer equation were determined as 8.720, 6.270 and 7.614 nm for the dominant planes of (110), (101) and (211) respectively.

In FTIR spectrum, the signals of oxygen functional groups such as C-O-C, C=O and O-H were gradually decreased by increasing the carbonization temperatures and they were almost pyrolysed at 650 °C. While the thermal stability of aromatic group C=C in GO is higher than oxygen functional groups as it pyrolysed slowly and still show significant signal at 550 °C.

References:

- [1] M.M. Arafat, B. Dinan, S.A. Akbar, A.S.M.A. Haseeb, Gas Sensors Based on One Dimensional Nanostructured Metal-Oxides: A Review, *Sensors*. 12 (2012) 7207–7258. doi:10.3390/s120607207.
- [2] J. Huang, Q. Wan, Gas Sensors Based on Semiconducting Metal Oxide One-Dimensional Nanostructures, *Sensors*. 9 (2009) 9903–9924. doi:10.3390/s91209903.
- [3] B. Ding, M. Wang, J. Yu, G. Sun, Gas Sensors Based on Electrospun Nanofibers, *Sensors*. 9 (2009) 1609–1624. doi:10.3390/s90301609.
- [4] D.-J. Yang, I. Kamienchick, D.Y. Youn, A. Rothschild, I.-D. Kim, Ultrasensitive and Highly Selective Gas Sensors Based on Electrospun SnO₂ Nanofibers Modified by Pd Loading, *Adv. Funct. Mater.* 20 (2010) 4258–4264. doi:10.1002/adfm.201001251.
- [5] J.-K. Choi, I.-S. Hwang, S.-J. Kim, J.-S. Park, S.-S. Park, U. Jeong, Y.C. Kang, J.-H. Lee, Design of selective gas sensors using electrospun Pd-doped SnO₂ hollow nanofibers, *Sens. Actuators B Chem.* 150 (2010) 191–199. doi:10.1016/j.snb.2010.07.013.
- [6] Y. Zhang, X. He, J. Li, Z. Miao, F. Huang, Fabrication and ethanol-sensing properties of micro gas sensor based on electrospun SnO₂ nanofibers, *Sens. Actuators B Chem.* 132 (2008) 67–73. doi:10.1016/j.snb.2008.01.006.
- [7] J. Watson, The tin oxide gas sensor and its applications, *Sens. Actuators*. 5 (1984) 29–42.
- [8] J.F. McAleer, P.T. Moseley, J.O. Norris, D.E. Williams, Tin dioxide gas sensors. Part 1.—Aspects of the surface chemistry revealed by electrical

- conductance variations, *J. Chem. Soc. Faraday Trans. 1 Phys. Chem. Condens. Phases.* 83 (1987) 1323–1346.
- [9] J.F. McAleer, P.T. Moseley, J.O. Norris, D.E. Williams, B.C. Tofield, Tin dioxide gas sensors. Part 2.—The role of surface additives, *J. Chem. Soc. Faraday Trans. 1 Phys. Chem. Condens. Phases.* 84 (1988) 441–457.
- [10] P. Ménini, F. Parret, M. Guerrero, K. Soulantica, L. Erades, A. Maisonnat, B. Chaudret, CO response of a nanostructured SnO₂ gas sensor doped with palladium and platinum, *Sens. Actuators B Chem.* 103 (2004) 111–114. doi:10.1016/j.snb.2004.04.103.
- [11] V. Lantto, T.T. Rantala, T.S. Rantala, Atomistic understanding of semiconductor gas sensors, *J. Eur. Ceram. Soc.* 21 (2001) 1961–1965.
- [12] J. Oviedo, M.J. Gillan, Energetics and structure of stoichiometric SnO₂ surfaces studied by first-principles calculations, *Surf. Sci.* 463 (2000) 93–101.
- [13] Z. Karami Horastani, S.M. Sayedi, M.H. Sheikhi, Effect of single wall carbon nanotube additive on electrical conductivity and methane sensitivity of SnO₂, *Sens. Actuators B Chem.* 202 (2014) 461–468. doi:10.1016/j.snb.2014.05.100.
- [14] J.-H. Lee, A. Katoch, S.-W. Choi, J.-H. Kim, H.W. Kim, S.S. Kim, Extraordinary Improvement of Gas-Sensing Performances in SnO₂ Nanofibers Due to Creation of Local *p* – *n* Heterojunctions by Loading Reduced Graphene Oxide Nanosheets, *ACS Appl. Mater. Interfaces.* 7 (2015) 3101–3109. doi:10.1021/am5071656.
- [15] J.S. Lee, O.S. Kwon, S.J. Park, E.Y. Park, S.A. You, H. Yoon, J. Jang, Fabrication of Ultrafine Metal-Oxide-Decorated Carbon Nanofibers for

- DMMP Sensor Application, *ACS Nano*. 5 (2011) 7992–8001.
doi:10.1021/nn202471f.
- [16] Z. Wang, C. Zhao, T. Han, Y. Zhang, S. Liu, T. Fei, G. Lu, T. Zhang, High-performance reduced graphene oxide-based room-temperature NO₂ sensors: A combined surface modification of SnO₂ nanoparticles and nitrogen doping approach, *Sens. Actuators B Chem.* 242 (2017) 269–279.
doi:10.1016/j.snb.2016.10.101.
- [17] Z. Wang, Z. Li, J. Sun, H. Zhang, W. Wang, W. Zheng, C. Wang, Improved Hydrogen Monitoring Properties Based on p-NiO/n-SnO₂ Heterojunction Composite Nanofibers, *J. Phys. Chem. C*. 114 (2010) 6100–6105.
doi:10.1021/jp9100202.
- [18] A. Yang, X. Tao, R. Wang, S. Lee, C. Surya, Room temperature gas sensing properties of SnO₂/multiwall-carbon-nanotube composite nanofibers, *Appl. Phys. Lett.* 91 (2007) 133110. doi:10.1063/1.2783479.
- [19] Q. Qi, T. Zhang, L. Liu, X. Zheng, Synthesis and toluene sensing properties of SnO₂ nanofibers, *Sens. Actuators B Chem.* 137 (2009) 471–475.
doi:10.1016/j.snb.2008.11.042.
- [20] P.A. Russo, N. Donato, S.G. Leonardi, S. Baek, D.E. Conte, G. Neri, N. Pinna, Room-Temperature Hydrogen Sensing with Heteronanostructures Based on Reduced Graphene Oxide and Tin Oxide, *Angew. Chem. Int. Ed.* 51 (2012) 11053–11057. doi:10.1002/anie.201204373.
- [21] C. Marichy, P.A. Russo, M. Latino, J.-P. Tessonier, M.-G. Willinger, N. Donato, G. Neri, N. Pinna, Tin dioxide–carbon heterostructures applied to gas sensing: structure-dependent properties and general sensing mechanism, *J. Phys. Chem. C*. 117 (2013) 19729–19739.

- [22] E.V. Iski, E.N. Yitamben, L. Gao, N.P. Guisinger, Graphene at the Atomic-Scale: Synthesis, Characterization, and Modification, *Adv. Funct. Mater.* 23 (2013) 2554–2564. doi:10.1002/adfm.201203421.
- [23] M.J. Allen, V.C. Tung, R.B. Kaner, Honeycomb Carbon: A Review of Graphene, *Chem. Rev.* 110 (2010) 132–145. doi:10.1021/cr900070d.
- [24] S. Wu, Q. He, C. Tan, Y. Wang, H. Zhang, Graphene-Based Electrochemical Sensors, *Small*. 9 (2013) 1160–1172.
- [25] T. Gan, S. Hu, Electrochemical sensors based on graphene materials, *Microchim. Acta.* 175 (2011) 1.
- [26] W. Yuan, G. Shi, Graphene-based gas sensors, *J. Mater. Chem. A.* 1 (2013) 10078. doi:10.1039/c3ta11774j.
- [27] D. Chen, H. Feng, J. Li, Graphene oxide: preparation, functionalization, and electrochemical applications, *Chem. Rev.* 112 (2012) 6027–6053.
- [28] S. Prezioso, F. Perrozzi, L. Giancaterini, C. Cantalini, E. Treossi, V. Palermo, M. Nardone, S. Santucci, L. Ottaviano, Graphene Oxide as a Practical Solution to High Sensitivity Gas Sensing, *J. Phys. Chem. C.* 117 (2013) 10683–10690. doi:10.1021/jp3085759.
- [29] Y. Zhu, S. Murali, W. Cai, X. Li, J.W. Suk, J.R. Potts, R.S. Ruoff, Graphene and Graphene Oxide: Synthesis, Properties, and Applications, *Adv. Mater.* 22 (2010) 3906–3924. doi:10.1002/adma.201001068.
- [30] S. Mao, S. Cui, G. Lu, K. Yu, Z. Wen, J. Chen, Tuning gas-sensing properties of reduced graphene oxide using tin oxide nanocrystals, *J. Mater. Chem.* 22 (2012) 11009–11013.
- [31] J.-H. Lee, A. Katoch, S.-W. Choi, J.-H. Kim, H.W. Kim, S.S. Kim, Extraordinary improvement of gas-sensing performances in SnO₂ nanofibers

- due to creation of local p–n heterojunctions by loading reduced graphene oxide nanosheets, *ACS Appl. Mater. Interfaces*. 7 (2015) 3101–3109.
- [32] S. Pei, H.-M. Cheng, The reduction of graphene oxide, *Carbon*. 50 (2012) 3210–3228.
- [33] S. Stankovich, D.A. Dikin, R.D. Piner, K.A. Kohlhaas, A. Kleinhammes, Y. Jia, Y. Wu, S.T. Nguyen, R.S. Ruoff, Synthesis of graphene-based nanosheets via chemical reduction of exfoliated graphite oxide, *Carbon*. 45 (2007) 1558–1565.
- [34] M.J. Fernandez-Merino, L. Guardia, J.I. Paredes, S. Villar-Rodil, P. Solis-Fernandez, A. Martinez-Alonso, J.M.D. Tascon, Vitamin C is an ideal substitute for hydrazine in the reduction of graphene oxide suspensions, *J. Phys. Chem. C*. 114 (2010) 6426–6432.
- [35] H.C. Schniepp, J.-L. Li, M.J. McAllister, H. Sai, M. Herrera-Alonso, D.H. Adamson, R.K. Prud'homme, R. Car, D.A. Saville, I.A. Aksay, Functionalized Single Graphene Sheets Derived from Splitting Graphite Oxide, *J. Phys. Chem. B*. 110 (2006) 8535–8539. doi:10.1021/jp060936f.
- [36] X. Wang, L. Zhi, K. Müllen, Transparent, Conductive Graphene Electrodes for Dye-Sensitized Solar Cells, *Nano Lett*. 8 (2008) 323–327. doi:10.1021/nl072838r.
- [37] R.K. Mishra, S.B. Upadhyay, A. Kushwaha, T.-H. Kim, G. Murali, R. Verma, M. Srivastava, J. Singh, P.P. Sahay, S. Hee Lee, SnO₂ quantum dots decorated on RGO: a superior sensitive, selective and reproducible performance for a H₂ and LPG sensor, *Nanoscale*. 7 (2015) 11971–11979. doi:10.1039/C5NR02837J.

- [38] D. Li, Y. Xia, Electrospinning of Nanofibers: Reinventing the Wheel?, *Adv. Mater.* 16 (2004) 1151–1170. doi:10.1002/adma.200400719.
- [39] C.J. Luo, S.D. Stoyanov, E. Stride, E. Pelan, M. Edirisinghe, Electrospinning versus fibre production methods: from specifics to technological convergence, *Chem. Soc. Rev.* 41 (2012) 4708. doi:10.1039/c2cs35083a.
- [40] J. Doshi, D.H. Reneker, Electrospinning process and applications of electrospun fibers, *J. Electrostat.* 35 (1995) 151–160.
- [41] A. Frenot, I.S. Chronakis, Polymer nanofibers assembled by electrospinning, *Curr. Opin. Colloid Interface Sci.* 8 (2003) 64–75.
- [42] Z.-M. Huang, Y.-Z. Zhang, M. Kotaki, S. Ramakrishna, A review on polymer nanofibers by electrospinning and their applications in nanocomposites, *Compos. Sci. Technol.* 63 (2003) 2223–2253. doi:10.1016/S0266-3538(03)00178-7.
- [43] F. Anton, Process and apparatus for preparing artificial threads, Google Patents, 1934. <https://www.google.com/patents/US1975504> (accessed April 1, 2017).
- [44] O. Jirsak, F. Sanetnik, D. Lukas, V. Kotek, L. Martinova, J. Chaloupek, A method of nanofibres production from a polymer solution using electrostatic spinning and a device for carrying out the method, WO2005024101 A1, 2005. <http://www.google.com/patents/WO2005024101A1> (accessed April 2, 2017).
- [45] C. Wang, Y. Li, G. Ding, X. Xie, M. Jiang, Preparation and characterization of graphene oxide/poly(vinyl alcohol) composite nanofibers via electrospinning, *J. Appl. Polym. Sci.* 127 (2013) 3026–3032. doi:10.1002/app.37656.

- [46] J. Wang, X. Wang, C. Xu, M. Zhang, X. Shang, Preparation of graphene/poly(vinyl alcohol) nanocomposites with enhanced mechanical properties and water resistance, *Polym. Int.* 60 (2011) 816–822. doi:10.1002/pi.3025.
- [47] L. Zhang, Z. Wang, C. Xu, Y. Li, J. Gao, W. Wang, Y. Liu, High strength graphene oxide/polyvinyl alcohol composite hydrogels, *J. Mater. Chem.* 21 (2011) 10399. doi:10.1039/c0jm04043f.
- [48] B.M. Yoo, H.J. Shin, H.W. Yoon, H.B. Park, Graphene and graphene oxide and their uses in barrier polymers: Review, *J. Appl. Polym. Sci.* 131 (2014) n/a-n/a. doi:10.1002/app.39628.
- [49] E. Zussman, X. Chen, W. Ding, L. Calabri, D.A. Dikin, J.P. Quintana, R.S. Ruoff, Mechanical and structural characterization of electrospun PAN-derived carbon nanofibers, *Carbon.* 43 (2005) 2175–2185. doi:10.1016/j.carbon.2005.03.031.
- [50] K.J. Lee, N. Shiratori, G.H. Lee, J. Miyawaki, I. Mochida, S.-H. Yoon, J. Jang, Activated carbon nanofiber produced from electrospun polyacrylonitrile nanofiber as a highly efficient formaldehyde adsorbent, *Carbon.* 48 (2010) 4248–4255. doi:10.1016/j.carbon.2010.07.034.
- [51] H.-I. Joh, H.K. Song, C.-H. Lee, J.-M. Yun, S.M. Jo, S. Lee, S.-I. Na, A.-T. Chien, S. Kumar, Preparation of porous carbon nanofibers derived from graphene oxide/polyacrylonitrile composites as electrochemical electrode materials, *Carbon.* 70 (2014) 308–312. doi:10.1016/j.carbon.2013.12.069.
- [52] W.S. Hummers Jr, R.E. Offeman, Preparation of graphitic oxide, *J. Am. Chem. Soc.* 80 (1958) 1339–1339.

- [53] H. Fong, I. Chun, D.H. Reneker, Beaded nanofibers formed during electrospinning, *Polymer*. 40 (1999) 4585–4592.
- [54] K.H. Lee, H.Y. Kim, H.J. Bang, Y.H. Jung, S.G. Lee, The change of bead morphology formed on electrospun polystyrene fibers, *Polymer*. 44 (2003) 4029–4034. doi:10.1016/S0032-3861(03)00345-8.
- [55] T. Lin, H. Wang, H. Wang, X. Wang, The charge effect of cationic surfactants on the elimination of fibre beads in the electrospinning of polystyrene, *Nanotechnology*. 15 (2004) 1375–1381. doi:10.1088/0957-4484/15/9/044.
- [56] J.M. Deitzel, J. Kleinmeyer, D.E.A. Harris, N.B. Tan, The effect of processing variables on the morphology of electrospun nanofibers and textiles, *Polymer*. 42 (2001) 261–272.
- [57] A.J. Guenther, S. Khombhongse, W. Liu, P. Dayal, D.H. Reneker, T. Kyu, Dynamics of Hollow Nanofiber Formation During Solidification Subjected to Solvent Evaporation, *Macromol. Theory Simul.* 15 (2006) 87–93. doi:10.1002/mats.200500034.
- [58] M. Wei, B. Kang, C. Sung, J. Mead, Core-Sheath Structure in Electrospun Nanofibers from Polymer Blends, *Macromol. Mater. Eng.* 291 (2006) 1307–1314. doi:10.1002/mame.200600284.
- [59] K. Zhang, X. Wang, Y. Yang, L. Wang, M. Zhu, B.S. Hsiao, B. Chu, Aligned and molecularly oriented semihollow ultrafine polymer fiber yarns by a facile method, *J. Polym. Sci. Part B Polym. Phys.* 48 (2010) 1118–1125. doi:10.1002/polb.22003.
- [60] K. Nayani, H. Katepalli, C.S. Sharma, A. Sharma, S. Patil, R. Venkataraghavan, Electrospinning Combined with Nonsolvent-Induced

- Phase Separation To Fabricate Highly Porous and Hollow Submicrometer Polymer Fibers, *Ind. Eng. Chem. Res.* 51 (2012) 1761–1766.
doi:10.1021/ie2009229.
- [61] X. Xia, X.J. Dong, Q.F. Wei, Y.B. Cai, K.Y. Lu, Formation mechanism of porous hollow SnO₂ nanofibers prepared by one-step electrospinning, *Express Polym. Lett.* 6 (2012) 169–176.
doi:10.3144/expresspolymlett.2012.18.
- [62] Y. Yin, R.M. Rioux, C.K. Erdonmez, S. Hughes, G.A. Somorjai, A.P. Alivisatos, Formation of hollow nanocrystals through the nanoscale Kirkendall effect, *Science*. 304 (2004) 711–714.
- [63] J. Liu, D. Xue, Thermal Oxidation Strategy towards Porous Metal Oxide Hollow Architectures, *Adv. Mater.* 20 (2008) 2622–2627.
doi:10.1002/adma.200800208.
- [64] J. Kong, Z. Liu, Z. Yang, H.R. Tan, S. Xiong, S.Y. Wong, X. Li, X. Lu, Carbon/SnO₂/carbon core/shell/shell hybrid nanofibers: tailored nanostructure for the anode of lithium ion batteries with high reversibility and rate capacity, *Nanoscale*. 4 (2012) 525–530. doi:10.1039/C1NR10962F.
- [65] H. Zhou, Z. Li, X. Niu, X. Xia, Q. Wei, The enhanced gas-sensing and photocatalytic performance of hollow and hollow core–shell SnO₂-based nanofibers induced by the Kirkendall effect, *Ceram. Int.* 42 (2016) 1817–1826. doi:10.1016/j.ceramint.2015.09.145.
- [66] M. Huang, Y. Zhang, F. Li, Z. Wang, Alamusi, N. Hu, Z. Wen, Q. Liu, Merging of Kirkendall Growth and Ostwald Ripening: CuO@MnO₂ Core-shell Architectures for Asymmetric Supercapacitors, *Sci. Rep.* 4 (2015).
doi:10.1038/srep04518.

- [67] L. Ji, M. Rao, H. Zheng, L. Zhang, Y. Li, W. Duan, J. Guo, E.J. Cairns, Y. Zhang, Graphene Oxide as a Sulfur Immobilizer in High Performance Lithium/Sulfur Cells, *J. Am. Chem. Soc.* 133 (2011) 18522–18525. doi:10.1021/ja206955k.
- [68] T.A. Pham, B.C. Choi, Y.T. Jeong, Facile covalent immobilization of cadmium sulfide quantum dots on graphene oxide nanosheets: preparation, characterization, and optical properties, *Nanotechnology*. 21 (2010) 465603. doi:10.1088/0957-4484/21/46/465603.
- [69] S. Sun, Y. Cao, J. Feng, P. Wu, Click chemistry as a route for the immobilization of well-defined polystyrene onto graphene sheets, *J. Mater. Chem.* 20 (2010) 5605. doi:10.1039/c0jm01269f.
- [70] X. Chen, Y. Dai, X. Wang, J. Guo, T. Liu, F. Li, Synthesis and characterization of Ag₃PO₄ immobilized with graphene oxide (GO) for enhanced photocatalytic activity and stability over 2,4-dichlorophenol under visible light irradiation, *J. Hazard. Mater.* 292 (2015) 9–18. doi:10.1016/j.jhazmat.2015.01.032.
- [71] F. Zhang, B. Zheng, J. Zhang, X. Huang, H. Liu, S. Guo, J. Zhang, Horseradish Peroxidase Immobilized on Graphene Oxide: Physical Properties and Applications in Phenolic Compound Removal, *J. Phys. Chem. C*. 114 (2010) 8469–8473. doi:10.1021/jp101073b.
- [72] Y. Xu, W. Hong, H. Bai, C. Li, G. Shi, Strong and ductile poly(vinyl alcohol)/graphene oxide composite films with a layered structure, *Carbon*. 47 (2009) 3538–3543. doi:10.1016/j.carbon.2009.08.022.
- [73] M. Yi, Z. Shen, X. Zhao, L. Liu, S. Liang, X. Zhang, Exploring few-layer graphene and graphene oxide as fillers to enhance the oxygen-atom

- corrosion resistance of composites, *Phys. Chem. Chem. Phys.* 16 (2014) 11162. doi:10.1039/c4cp00114a.
- [74] Y. Tan, Y. Song, Q. Zheng, Hydrogen bonding-driven rheological modulation of chemically reduced graphene oxide/poly(vinyl alcohol) suspensions and its application in electrospinning, *Nanoscale*. 4 (2012) 6997. doi:10.1039/c2nr32160b.
- [75] B. Wang, Z. Chen, J. Zhang, J. Cao, S. Wang, Q. Tian, M. Gao, Q. Xu, Fabrication of PVA/graphene oxide/TiO₂ composite nanofibers through electrospinning and interface sol–gel reaction: Effect of graphene oxide on PVA nanofibers and growth of TiO₂, *Colloids Surf. Physicochem. Eng. Asp.* 457 (2014) 318–325. doi:10.1016/j.colsurfa.2014.06.006.
- [76] P. Tan, J. Wen, Y. Hu, X. Tan, Adsorption of Cu²⁺ and Cd²⁺ from aqueous solution by novel electrospun poly(vinyl alcohol)/graphene oxide nanofibers, *RSC Adv.* 6 (2016) 79641–79650. doi:10.1039/C6RA18052C.
- [77] D. Luo, G. Zhang, J. Liu, X. Sun, Evaluation criteria for reduced graphene oxide, *J. Phys. Chem. C*. 115 (2011) 11327–11335.
- [78] J. Shen, Y. Hu, M. Shi, X. Lu, C. Qin, C. Li, M. Ye, Fast and facile preparation of graphene oxide and reduced graphene oxide nanoplatelets, *Chem. Mater.* 21 (2009) 3514–3520.

Chapter 5

Gas sensing measurement

5.1 Gas testing chamber

Actually there is no standard sensor electrode and gas testing chamber, therefore the sensor sensitivities and results could be varied from different designs. The gas sensor material would be coated on a prototype glass substrate by drop-drying method, later sputtered with gold electrodes of dimensions of 10 mm × 2 mm, which are separated by 5 mm on the glass surface as shown in Figure 5.1. While the gas testing chamber is homemade with an inlet connected with two mass flow controllers (Kellllhua), three feedthroughs of electrodes and an outlet connected to a vacuum pump. The schematic diagram of the gas testing chamber is shown in Figure 5.2. The mass flow controllers for the delivery of methane gas have been calibrated with a standard Alicat MFC. The methane gas was purchased from Hong Kong Oxygen with 99.9% in purity. The vacuum pump used is a mini portabele FY-1H Value vacuum pump with largest flow rate of about 30 L/min. Resistance measurement was delivered by four-point electrodes such that the noise from contact potentials could be minimized. The electrodes are connected to

the Keithley 2400 source-meter for data acquisition. During operation for 1% methane gas sensing, the mass flow controllers connected to the air end and methane end are adjusted to give flow rates of 10 L/min and 100 ml/min respectively. The two flow rates could be simply adjusted to enable the measurement of different methane gas concentration.

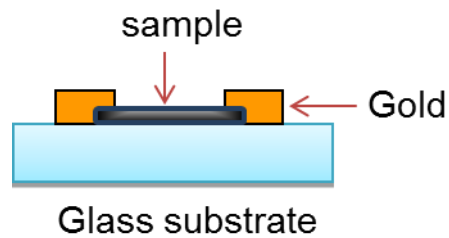


Figure 5.1 A schematic diagram of a prototype electrodes design.

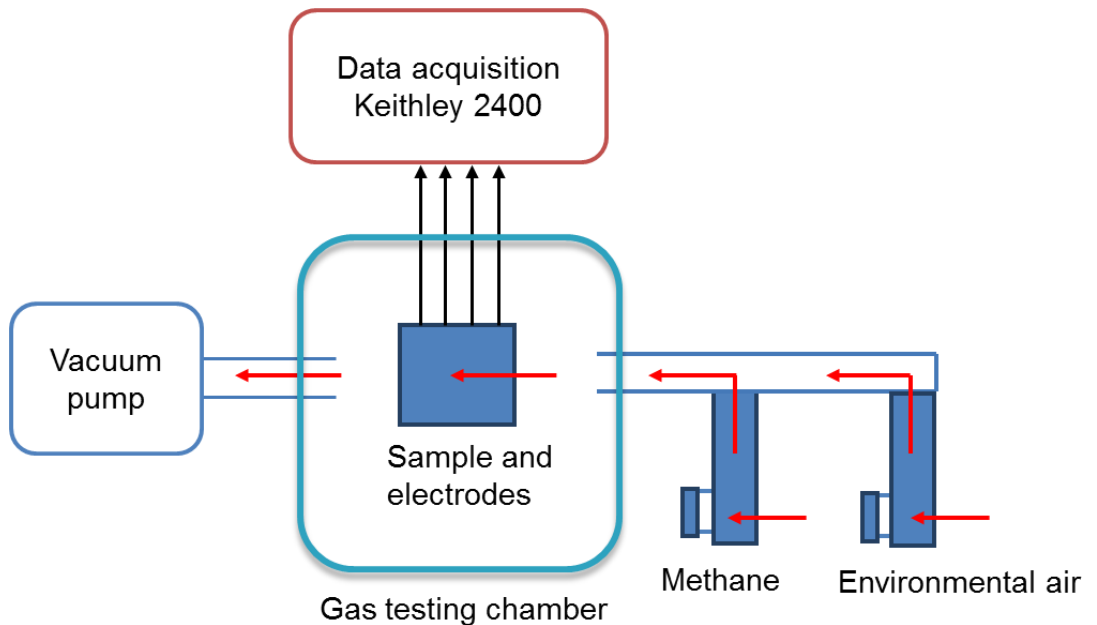


Figure 5.2 A schematic diagram of a homemade gas testing chamber and equipment setup.

5.2 Gas sensing measurement

There are two types of methane gas sensors which are developed by drop-drying method and electrospinning method. The electrical measurements of resistances and sensitivities towards methane are discussed as below.

5.2.1 Methane gas sensor by drop-drying method

5.2.1.1 Resistance measurement

The electrical measurements of the resistance of the GO, R(G), R(B), R(A), R(H) and their heterostructures with SnO₂ at room temperature are shown in Figure 5.3.

The GO, a p-type material, had the highest resistance in this group due to the abundance of oxygen functional groups, which extracted and bound electrons to the surface, enlarging the space charge layer to reduce surface conductivity [1].

Hence, resistance decreased for the increasing degree of reduction of the GO due to the removal of oxygen functional groups, which released the bound electrons back to the core. The resistances of the RGO were in descending order of R(G), R(B), R(A) and R(H), which is consistent with the results from Raman, FTIR and XRD. The incorporation of SnO₂ into RGO increased the resistance by about one or two orders of magnitude due to the p-n junction effect at the contact boundary between the p-type RGO and n-type SnO₂ [2,3]. SnO₂ is n-type due to the

introduction of free electrons at oxygen vacancy sites on the surface after annealing [4]. The n-type SnO₂ released its free electrons to the core and reduced the amount of free holes, which increased the resistance. The heterostructures were still p-type as a whole, as the number of free electrons released by SnO₂ was much less than the free holes in the RGO; oxygen in the air bound and extracted the free electrons at the vacancy defects of the SnO₂ surface, significantly decreasing the amount of electrons released back to the RGO core. Sensitivity measurements further confirmed that the heterostructures were p-type, as discussed in the next section. The larger increases of resistance in R(A)-SnO₂ and R(H)-SnO₂ (~two orders of magnitude) than in R(G)-SnO₂ and R(B)-SnO₂ (~one order of magnitude) could have been caused by the larger agglomerates of R(A) and R(H) with SnO₂, which resulted in more contact boundaries between RGO and SnO₂, thus strengthening the p-n junction effect.

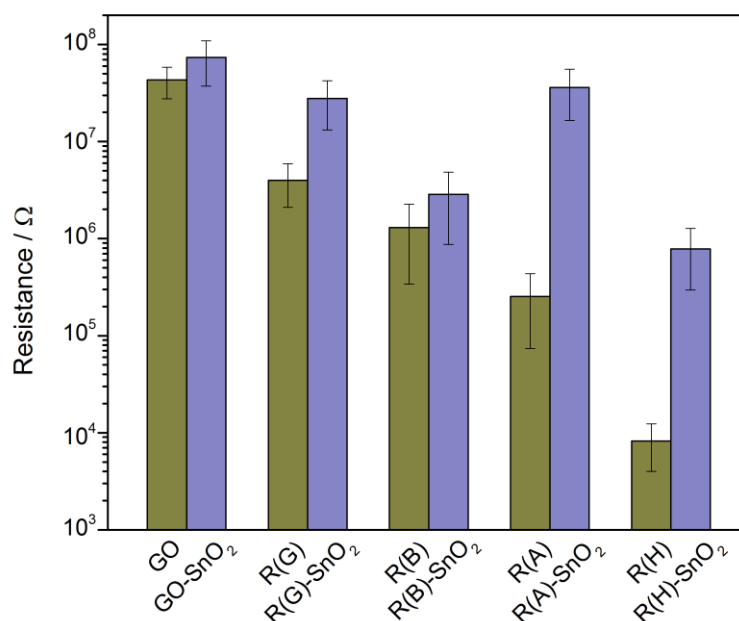


Figure 5.3 Resistance of GO, R(G), R(B), R(A), R(H) and their heterostructures with SnO₂ at room temperature.

5.2.1.2 Sensitivity measurement

The gas response, i.e., sensitivity, was measured in a homemade gas-testing chamber with a dynamic gas flow of 1% methane gas relative to the environmental air at room temperature. Sensitivity was defined as $(R_g - R_a)/R_a$, where R_g is the resistance of the sample when the chamber was filled with methane gas, while R_a is the resistance of the sample when the methane gas in the chamber was purged by environmental air. The sensitivity measurements of R(G), R(B), R(A) and R(H) and their heterostructures with SnO₂ towards methane at

room temperature are depicted in Figure 5.4. The sensitivities of all of the samples were positive due to the increase of resistance when the methane gas interacted with p-type samples. Methane is a reducing gas, which releases the bound electrons at the surface back to the core; hence, the number of holes in the RGO and RGO-SnO₂ decreased, increasing the resistance. R(G) had the highest sensitivity among the homostructures, as glucose had the weakest reducing power; most of the oxygen functional groups in R(G) remained for the methane gas to interact with. The sensitivity of R(G) was even higher than that of the GO, perhaps due to the residues of d-glucose remaining after reduction. After the reduction of the GO, D-glucose was oxidised to gluconic acid or the more stable ring form glucono delta-lactone, both of which contained oxygen functional groups that further enlarged the space charge layer at the surface; therefore, the sensitivity was further increased by any residues of D-glucose. R(A) had a lower resistance than R(B), as shown in Figure 5.3, so it was expected that R(A) would have a lower sensitivity than R(B). However, on the contrary, R(A) had a higher sensitivity than R(B), as shown in Figure 5.4, a finding attributed to the residues of L-ascorbic acid. Dehydroascorbic acid (DHA), which was formed by the oxidation of L-ascorbic acid after the reduction of the GO, also contained oxygen functional groups, thus causing an increase in sensitivity. Most of the ascorbic

acid was probably oxidised to DHA due to the high degree of reduction of R(A), as discussed previously. R(B) and R(H) had lower sensitivities than the other homostructures because the oxidative products of borohydride and hydrazine did not have oxygen functional groups to increase the sensitivity. R(H) had the lowest sensitivity of all, as hydrazine had the strongest reducing power; thus, most of the oxygen functional groups were removed, as discussed previously.

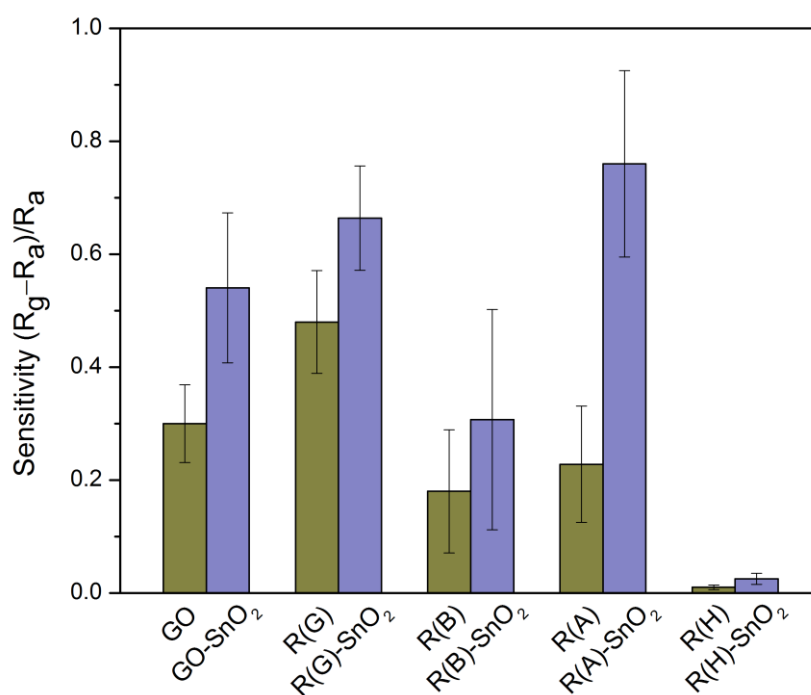


Figure 5.4 Sensitivity of GO, R(G), R(B), R(A), R(H) and their heterostructures with SnO₂ towards methane (1%) at room temperature.

The sensitivity of R(H) increased after the incorporation of SnO₂, as observed in all of the heterostructures, due to the p-n junction effect, which enlarged the space charge layer to increase the responsiveness. Methane gas typically releases electrons back to the core when interacting with the adsorbed oxygen at vacancy defect sites on the surface of SnO₂. The release of electrons back to the p-type RGO decreases the amount of holes, thus increasing the resistance and sensitivity. R(H)-SnO₂ did not show a comparable increase of sensitivity to the other heterostructures, possibly because the increase of the Schottky barrier by the p-n junction was not significant and the sensitivity was instead dominated by the high conductivity of R(H). The distinctive increase of sensitivity of R(A)-SnO₂ compared with R(A) was caused by the synergistic effect between DHA (from the oxidation of ascorbic acid) and SnO₂, which is discussed in the next chapter. Figure 5.5 (a) and (b) show the sensitivity against time for the homostructures and heterostructures towards methane of 1% at room temperature, respectively. Methane gas was forced out using environmental air when the sensitivity became saturated. The response time was defined as the time taken by the sensor to reach 90% of the saturated sensitivity. The response times of the gas sensors of the homostructures and their heterostructures were about 100–200 s. The resistance against time plot of R(A)-SnO₂ at different methane concentrations

and sensitivity against methane concentration are shown in Figure 5.6 (a) and (b) respectively.

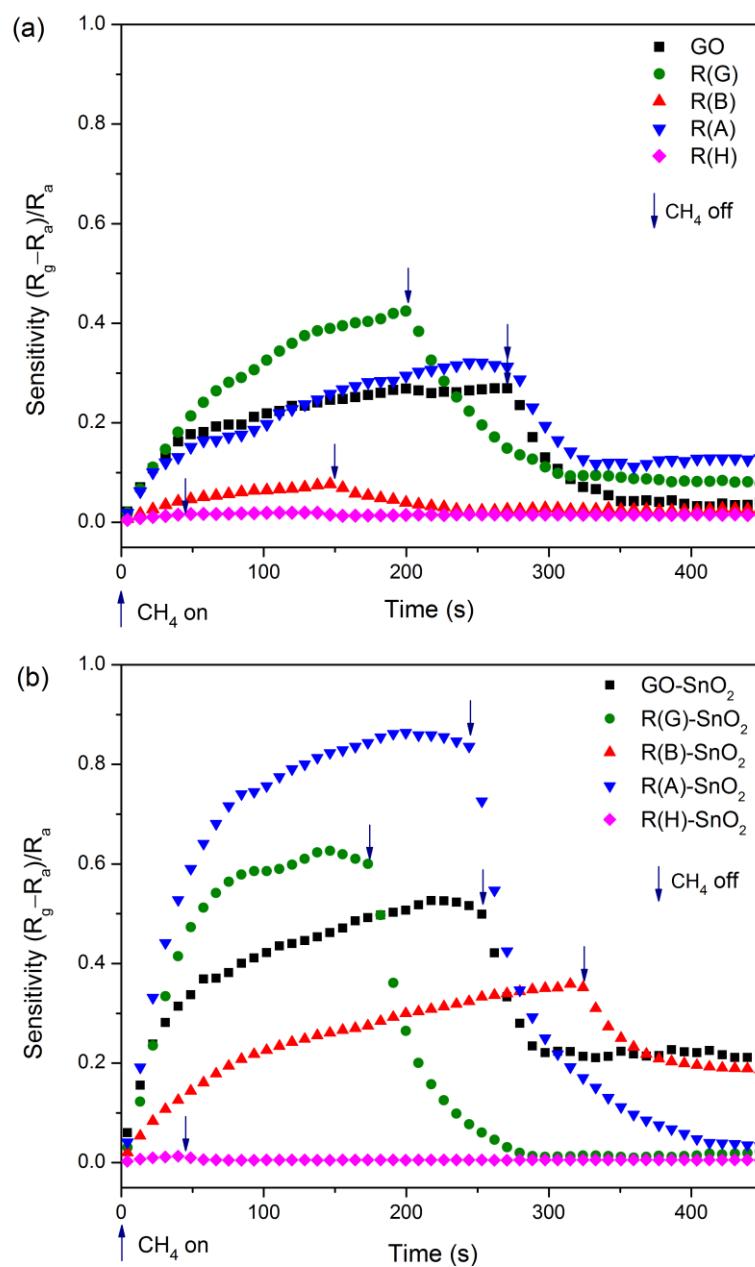


Figure 5.5 Sensitivity against time plot of (a) GO, R(G), R(B), R(A) and R(H);
 (b) GO-SnO₂, R(G)-SnO₂, R(B)-SnO₂, R(A)-SnO₂ and R(H)-SnO₂
 towards methane (1%) at room temperature.

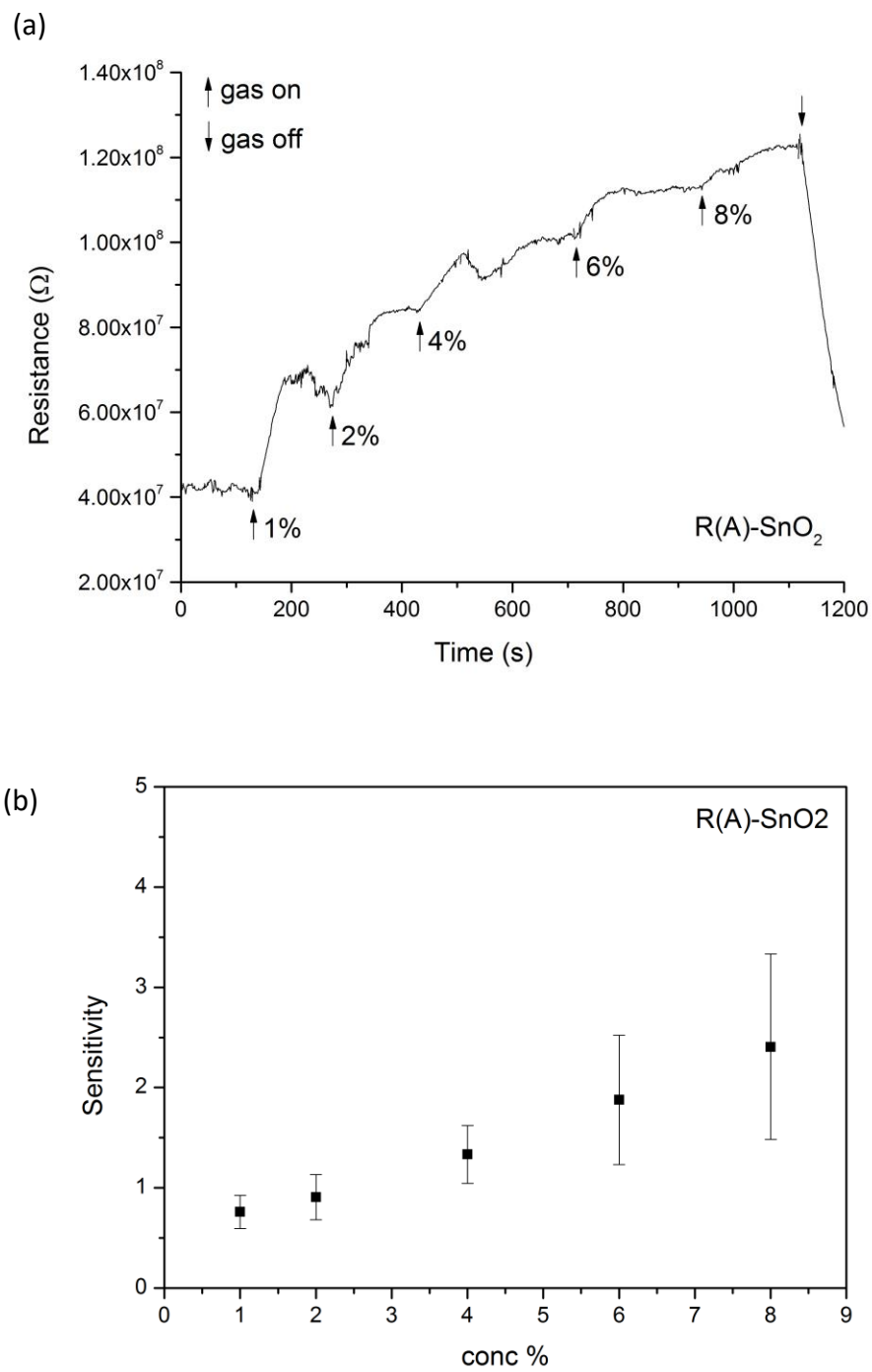


Figure 5.6 (a) Resistance against time plot at different methane concentration and (b) sensitivity against methane concentration of R(A)-SnO₂.

5.2.2 Methane gas sensor by electrospinning method

5.2.2.1 Resistance measurement

The resistances of the composite nanofiber PVA/SnO₂/GO with different GO contents carbonized at different temperatures were shown in Figure 5.7. The composite nanofiber PVA/SnO₂/GO was poorly conductive before carbonization when measured at room temperature. After carbonization, the resistance of the composite nanofiber decreased with increasing temperature. PVA and GO are p-typed materials due to the abundance of oxygen functional groups which extract electrons to surface which increases space charge layer to reduce surface conductivity [5]. After carbonization, PVA and GO were less p-typed as most oxygen functional groups were removed. The incorporation of SnO₂ to PVA/GO will increase the resistance due to the p-n junction effect at the contact boundary between the p-typed PVA/GO and the n-typed SnO₂ [6,7]. SnO₂ is n-typed material due to the introduction of free electrons at oxygen vacancy sites after carbonization [4,8]. The free electrons at oxygen vacancy sites were released to the p-typed PVA/GO core which reduces amount of free holes so that resistance increased. However, the composite nanofiber of PVA/SnO₂/GO was p-typed as oxygen in air would bind to some oxygen vacancy sites in SnO₂ to extract

electrons back to surface. Hence the electrons at core were much less than the free holes contributed by PVA and GO. The decrease of resistance with increasing temperatures of carbonization was ascribed to the following two reasons. Firstly the oxygen functional groups in PVA and GO were gradually removed and secondly the oxygen vacancy sites of SnO₂ increased with the crystallization of SnO₂ at higher temperatures of carbonization. Hence the amount of electrons released back to core increased which decreased the resistance of the composite nanofiber. The resistances were generally lower with increasing GO contents as observed from N0 to N4 for each carbonization temperature which could be due to the increased amount of amorphous carbon.

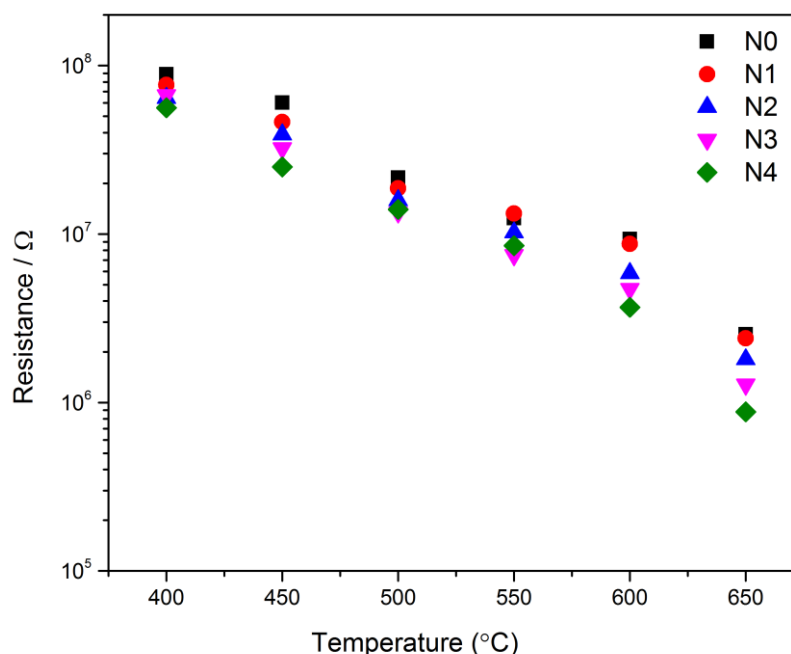


Figure 5.7 Resistances of the composite nanofibers PVA/SnO₂/GO with different GO contents carbonized at different temperatures.

5.2.2.2 Sensitivity measurement

The sensitivities of composite nanofiber of PVA/SnO₂/GO with different GO contents carbonized at different temperatures towards methane (1%) measured at room temperature were shown in Figure 5.8. Sensitivity was measured in a home-made gas chamber which is defined as $(R_g - R_a)/R_a$, where R_g is the resistance of the sample with methane gas filling into environmental air while R_a is the resistance of the sample when the methane gas in the chamber was purged by environmental air. Sensitivities of composite nanofibers at all carbonization temperatures were positive due to the increase of resistance when the reducing gas methane interacts with the p-typed composite nanofibers. Methane would repel the bound electrons at the surface of composite nanofiber back to p-typed core so resistance and sensitivity increased. Sensitivities of N1 to N4 firstly increased to maximum values at carbonization temperature of 550 °C, but then decreased afterwards. The increase of sensitivity from 400 to 550 °C was due to the increased crystallization of SnO₂ which increased more oxygen vacancy sites for gaseous interaction. The effect from the removal of oxygen functional groups of PVA and GO were less significant than the effect from increased crystallization of SnO₂ as most oxygen functional groups were removed around 400 - 450 °C as shown in TGA and FTIR spectra. Sensitivities decreased for carbonization higher

than 550 °C which could be due to the decreased amount of p-typed amorphous carbon with residual oxygen functional groups at higher carbonization temperatures, which lowering the p-n junction effect and sensitivity as some works reported that oxygen functional groups in GO were not completely removed even at 1100 °C [9–11].

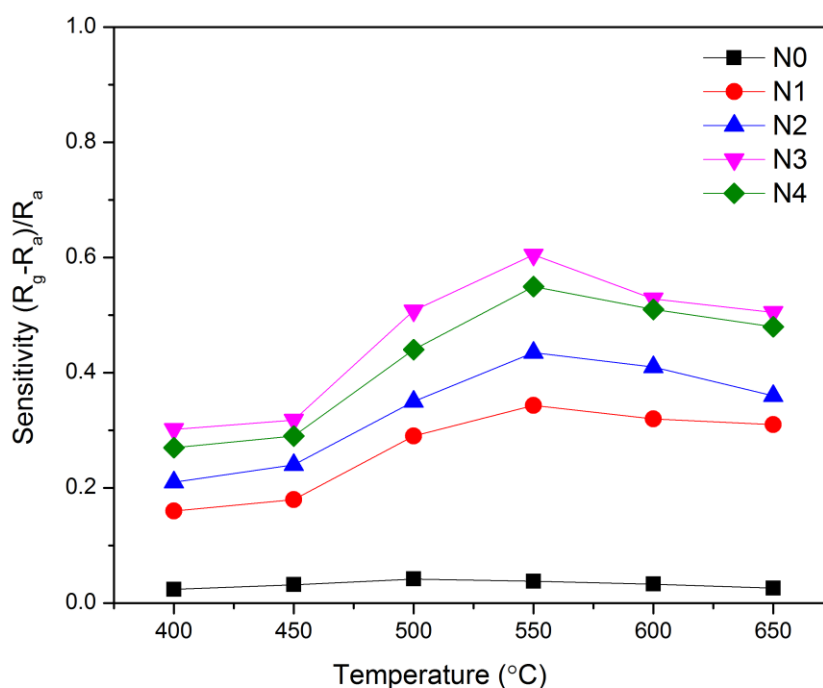


Figure 5.8 Sensitivities of the composite nanofibers PVA/SnO₂/GO with different GO contents carbonized at different temperatures towards methane (1%).

Representative resistance against time plots of the composite nanofibers PVA/SnO₂/GO at different carbonization temperatures towards methane (1%) at

room temperature are shown in Figure 5.9. While the representative resistance against time plots of the composite nanofibers PVA/SnO₂/GO with different GO contents at carbonization temperature of 550°C towards methane (1%) at room temperature are shown in Figure 5.10.

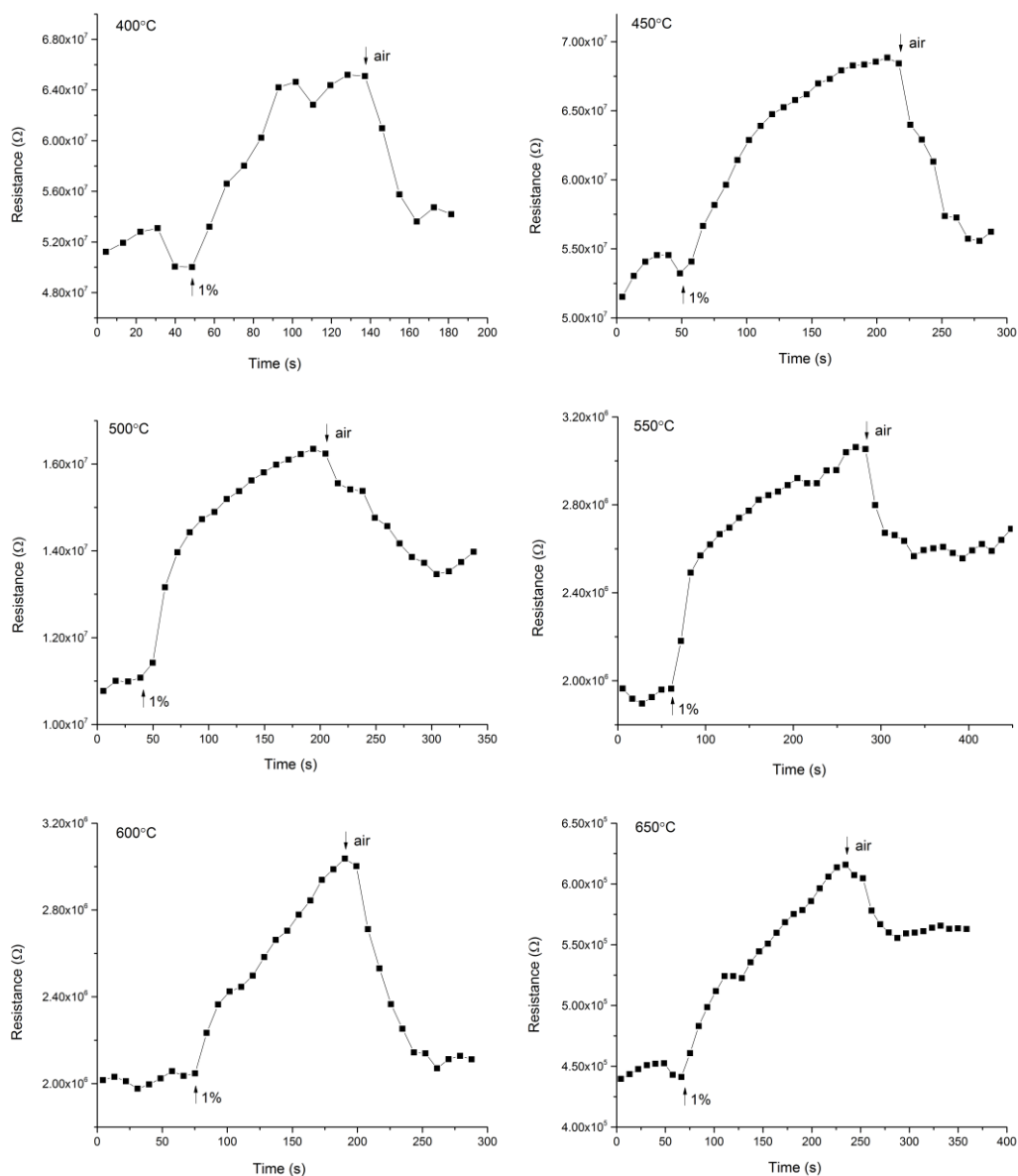


Figure 5.9 Representative resistance against time plots of the composite nanofibers PVA/SnO₂/GO at different carbonization temperatures towards methane (1%).

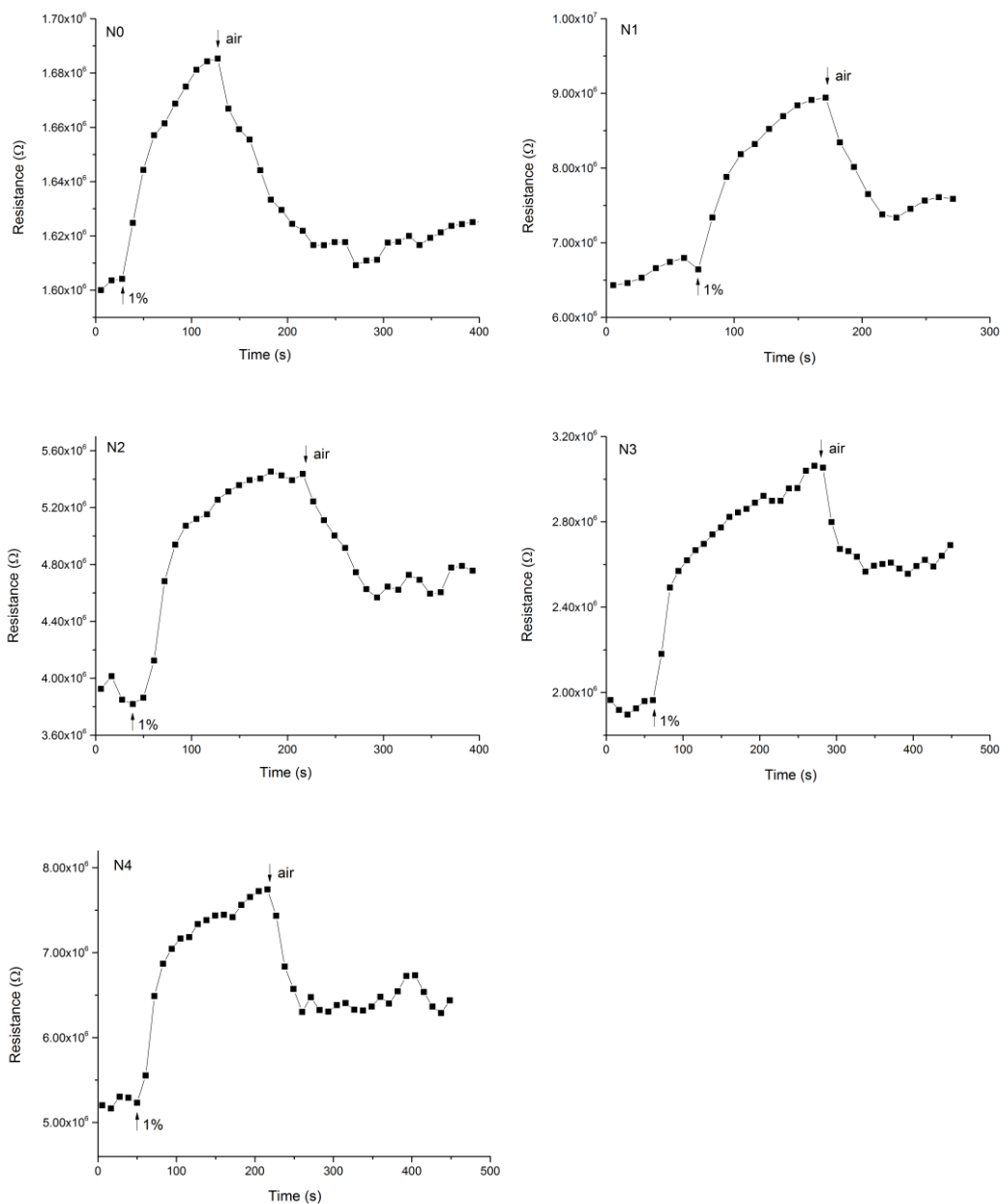


Figure 5.10 Representative resistance against time plots of the composite nanofibers PVA/SnO₂/GO with different GO contents at carbonization temperature of 550°C towards methane (1%).

The sensitivities of composite nanofibers of PVA/SnO₂/GO with different GO contents after carbonization at 550 °C towards methane (1%) measured at

room temperature were shown in Figure 5.11. The sensitivity of the composite nanofiber N0 without GO content was determined the lowest which could be due to the amorphous carbon form a thin-skinned layer to cover the shell of SnO₂ in the core-shell nanofiber structure as shown in TEM images. Firstly, the carbon skin layer shielded SnO₂ from contacting with gases for interaction and secondly it minimized the p-n junction effect by decreasing the contact boundary between the p-typed amorphous carbon and the n-typed SnO₂. The composite nanofibers of N1 to N4 with GO content had much higher sensitivities than N0 which could be due to the different nanofiber structures. The addition of GO completely changed the core-shell structure to the porous nanofiber structure as shown in TEM images. The porous structure would benefit gaseous interaction as well as increasing the p-n junction effect by increasing the contact boundary between amorphous carbon and SnO₂. Sensitivities increased with increasing GO content as observed from N1 to N3 which could be due to the increased amount of p-typed amorphous carbon after carbonization as confirmed by Raman and TGA spectra. The sensitivity decreased slightly from N3 to N4 could be due to two reasons. Firstly the large amount of carbon layer after carbonization in N4 shielded the gases from interacting with SnO₂ nanocrystallites beneath and secondly the p-n junction effect became saturated as more carbon layer would not increase the contact

boundary between amorphous carbon and SnO₂.

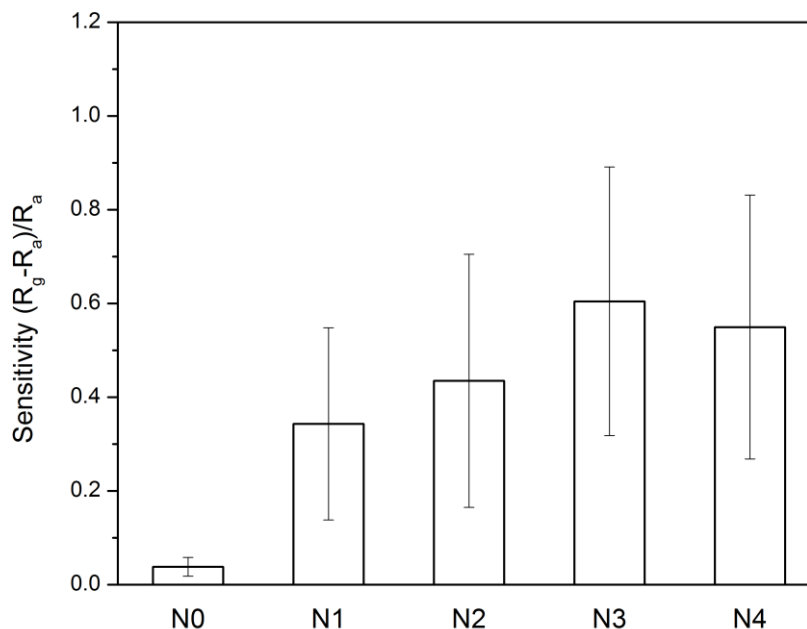


Figure 5.11 Sensitivities of the composite nanofibers PVA/SnO₂/GO with different GO contents after carbonization at 550 °C towards methane (1%).

The sensitivities of the composite nanofiber of N3 after carbonization at 550 °C towards methane at different concentrations were shown in Figure 5.12. The sensitivity increased from the lowest value of 15.1% at 1000 ppm to the highest value of 60.5% at 10000 ppm. The gas sensor was not saturated even at high concentration of methane from 6000-10000 ppm which is useful in high concentration application as most methane sensor was saturated at such

concentrations [12–15]. The resistance against time plot of the composite nanofiber of N3 after carbonization at 550 °C towards methane at different concentrations was shown in Figure 5.13. The response time was defined as the time taken by the sensor to reach 90% of the saturated sensitivity. The response time of the sensor was determined about 80 s.

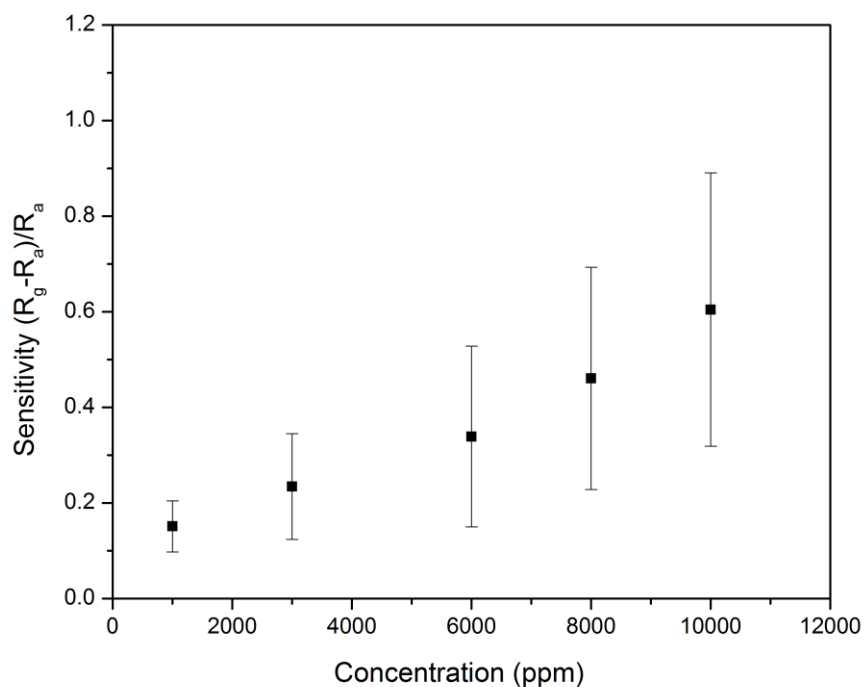


Figure 5.12 Sensitivities of the composite nanofiber of N3 after carbonization at 550 °C towards methane at different concentrations.

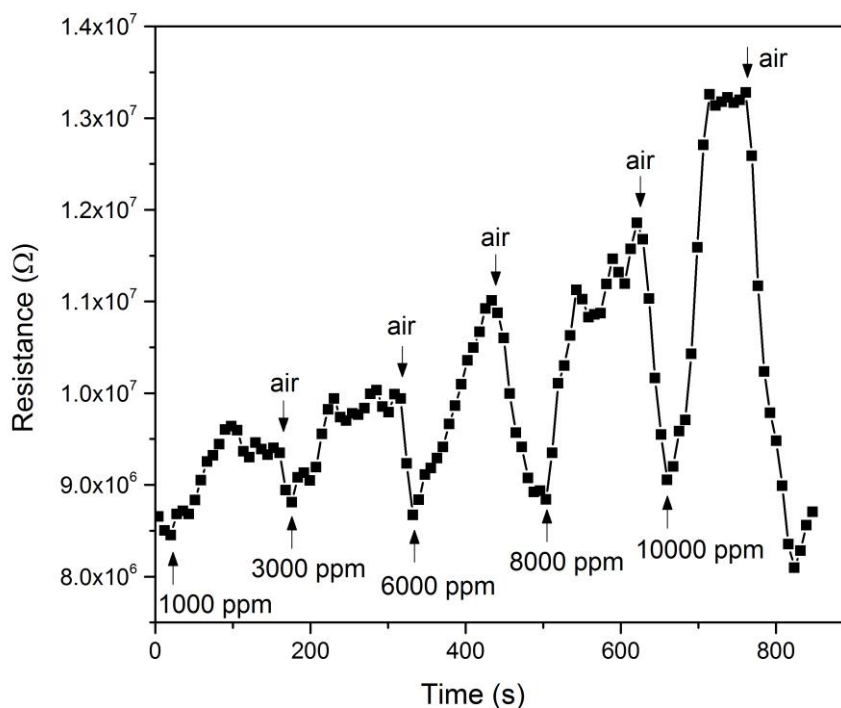


Figure 5.13 Resistance against time plot of the composite nanofiber of N3 after carbonization at 550 °C towards methane at different concentrations.

Table 5.1 summarizes the recent reports in the literature on room-temperature methane sensors compared with this work. Note that the sensing response and gas concentration are generally linear in log scale [16,17]; hence, it is clear that our highest-performing sensor, R(A)-SnO₂ from drop-drying method, exhibited much better sensitivity (76%) than the metal oxide gas sensors and was comparable with a CNT sensor [18]. While the composite nanofiber gas sensor of PVA/SnO₂/GO from electrospinning method was the third highest among. However, the

sensitivity of the CNT [43] sensor reached saturation near a methane concentration of 6,500 ppm, while the sensitivities of our sensors of R(A)/SnO₂ and PVA/SnO₂/GO nanofiber are not saturated at this concentration. Indeed, the sensitivity of R(A)/SnO₂ was found to increase up to 241% at 80000 ppm.

Table 5.1 Recent reports on room temperature methane sensors.

Sensing material	Technique	CH ₄ conc.	Sensitivity	Year
CNT and CNF [18]	Electrolysis	10,000 ppm	75%	2005
Pd/MWCNTs [19]	Chemical method	20,000 ppm	4.5%	2008
SnO ₂ nanorods [20]	Precipitation method	2,500 ppm	0.58%	2012
Graphene/PANI [21]	Chemical method	3,200 ppm	5%	2013
Pt/SWCNTs [22]	Electrochemical method	200 ppm	1.6%	2013
VO ₂ [23]	Pulsed dc sputtering	500 ppm	3.2% (50 °C)	2014
TiO ₂ /n-Si [24]	rf sputtering	1,000 ppm	16% (50°C)	2016
PbS colloidal nanocrystals [25]	Chemical method	50,000 ppm	47.6%	2016
Pd doped SnO ₂ /RGO [26]	Hydrothermal method	4,000 ppm	2.07%	2016
R(A)/SnO ₂	Chemical method	10,000 ppm	76%	Present work
PVA/SnO ₂ /GO nanofiber	Electrospinning method	10,000 ppm	60.5%	Present work

5.3 Conclusion

In this chapter, the methane gas sensing properties developed by drop drying and electrospinning methods were investigated. In drop-drying method, It was found that the resistances decreased for the increasing degree of reduction of GO due to the removal of oxygen functional groups. The resistances of the RGOs were found to decrease in order of R(G), R(B), R(A) and R(H). The incorporation of SnO₂ into RGOs increased the resistance by about one or two orders of magnitude due

to the p-n junction effect at the contact boundary between the p-type RGO and n-type SnO₂.

Sensitivities generally decreased with increasing the reduction levels of the RGOs due to the residues of the oxygen functional groups on RGO surfaces. Therefore, R(G) had the highest sensitivity while R(H) had the lowest one. On the contrary, R(A) with a higher reduction level had higher sensitivity than R(B) which could be due to the residues of the oxygen functional groups of dehydroascorbic acid after reduction. The sensitivities of all heterostructures with SnO₂ were higher than their homostructures due to the p-n junction effect. While R(A)-SnO₂ was found to have even higher sensitivity than R(G)-SnO₂ which could be due to the synergistic effect between dehydroascorbic acid and SnO₂. The synergistic effect would be studied by density functional theory calculations in the next chapter.

In electrospinning method, the resistances of the composite nanofiber of PVA/SnO₂/GO were found to decrease with increasing carbonization temperature and GO content. Increasing carbonization temperature would increase relative amount of conductive amorphous carbon produced after carbonization which

decreases resistance. While increasing the content of the comparatively more conductive GO would also decrease resistance.

The sensitivities of the composite nanofiber of N0 without GO content was determined the lowest which could be due to the thin-skinned layer of amorphous carbon which cover the surface of the core-shell nanofiber structure as the carbon skin layer had shielded SnO₂ from contacting with gases for interaction and also minimized the p-n junction effect by decreasing the contact boundary between the p-typed amorphous carbon and the n-typed SnO₂. The composite nanofibers of N1 to N4 with GO content had much higher sensitivities than N0 which could be due to the formation of porous nanofiber structures rather than the core-shell structure which benefit gaseous interaction as well as increasing the p-n junction effect by increasing the contact boundary between amorphous carbon and SnO₂. Sensitivity of N3 with GO content of 5 wt% was found to have the highest sensitivity of 60.5% at carbonization temperature of 550°C towards methane of 1%.

References:

- [1] D. Chen, H. Feng, J. Li, Graphene Oxide: Preparation, Functionalization, and Electrochemical Applications, *Chem. Rev.* 112 (2012) 6027–6053.
doi:10.1021/cr300115g.
- [2] S. Mao, S. Cui, G. Lu, K. Yu, Z. Wen, J. Chen, Tuning gas-sensing properties of reduced graphene oxide using tin oxide nanocrystals, *J. Mater. Chem.* 22 (2012) 11009. doi:10.1039/c2jm30378g.
- [3] J.-H. Lee, A. Katoch, S.-W. Choi, J.-H. Kim, H.W. Kim, S.S. Kim, Extraordinary Improvement of Gas-Sensing Performances in SnO₂ Nanofibers Due to Creation of Local *p* – *n* Heterojunctions by Loading Reduced Graphene Oxide Nanosheets, *ACS Appl. Mater. Interfaces.* 7 (2015) 3101–3109. doi:10.1021/am5071656.
- [4] V. Lantto, T.T. Rantala, T.S. Rantala, Atomistic understanding of semiconductor gas sensors, *J. Eur. Ceram. Soc.* 21 (2001) 1961–1965.
- [5] N. Yamazoe, New approaches for improving semiconductor gas sensors, *Sens. Actuators B Chem.* 5 (1991) 7–19.
- [6] S. Mao, S. Cui, G. Lu, K. Yu, Z. Wen, J. Chen, Tuning gas-sensing properties of reduced graphene oxide using tin oxide nanocrystals, *J. Mater. Chem.* 22 (2012) 11009–11013.

- [7] J.-H. Lee, A. Katoch, S.-W. Choi, J.-H. Kim, H.W. Kim, S.S. Kim, Extraordinary improvement of gas-sensing performances in SnO₂ nanofibers due to creation of local p–n heterojunctions by loading reduced graphene oxide nanosheets, *ACS Appl. Mater. Interfaces*. 7 (2015) 3101–3109.
- [8] J. Oviedo, M.J. Gillan, Energetics and structure of stoichiometric SnO₂ surfaces studied by first-principles calculations, *Surf. Sci.* 463 (2000) 93–101.
- [9] C. Mattevi, G. Eda, S. Agnoli, S. Miller, K.A. Mkhoyan, O. Celik, D. Mastrogiovanni, G. Granozzi, E. Garfunkel, M. Chhowalla, Evolution of Electrical, Chemical, and Structural Properties of Transparent and Conducting Chemically Derived Graphene Thin Films, *Adv. Funct. Mater.* 19 (2009) 2577–2583. doi:10.1002/adfm.200900166.
- [10] H.A. Becerril, J. Mao, Z. Liu, R.M. Stoltenberg, Z. Bao, Y. Chen, Evaluation of Solution-Processed Reduced Graphene Oxide Films as Transparent Conductors, *ACS Nano*. 2 (2008) 463–470. doi:10.1021/nn700375n.
- [11] S. Pei, H.-M. Cheng, The reduction of graphene oxide, *Carbon*. 50 (2012) 3210–3228.
- [12] P.K. Basu, S.K. Jana, H. Saha, S. Basu, Low temperature methane sensing by electrochemically grown and surface modified ZnO thin films, *Sens.*

-
- Actuators B Chem. 135 (2008) 81–88. doi:10.1016/j.snb.2008.07.021.
- [13] M. Penza, R. Rossi, M. Alvisi, D. Suriano, E. Serra, Pt-modified carbon nanotube networked layers for enhanced gas microsensors, *Thin Solid Films*. 520 (2011) 959–965. doi:10.1016/j.tsf.2011.04.178.
- [14] R.K. Roy, M.P. Chowdhury, A.K. Pal, Room temperature sensor based on carbon nanotubes and nanofibres for methane detection, *Vacuum*. 77 (2005) 223–229. doi:10.1016/j.vacuum.2004.08.023.
- [15] B.-K. Min, S.-D. Choi, Undoped and 0.1wt.% Ca-doped Pt-catalyzed SnO₂ sensors for CH₄ detection, *Sens. Actuators B Chem*. 108 (2005) 119–124. doi:10.1016/j.snb.2004.12.112.
- [16] H. Wang, Y. Qu, H. Chen, Z. Lin, K. Dai, Highly selective n-butanol gas sensor based on mesoporous SnO₂ prepared with hydrothermal treatment, *Sens. Actuators B Chem*. 201 (2014) 153–159.
- [17] J. Hu, F. Gao, Z. Zhao, S. Sang, P. Li, W. Zhang, X. Zhou, Y. Chen, Synthesis and characterization of Cobalt-doped ZnO microstructures for methane gas sensing, *Appl. Surf. Sci*. 363 (2016) 181–188. doi:10.1016/j.apsusc.2015.12.024.
- [18] R.K. Roy, M.P. Chowdhury, A.K. Pal, Room temperature sensor based on carbon nanotubes and nanofibres for methane detection, *Vacuum*. 77 (2005)

223–229. doi:10.1016/j.vacuum.2004.08.023.

- [19] Y. Li, H. Wang, Y. Chen, M. Yang, A multi-walled carbon nanotube/palladium nanocomposite prepared by a facile method for the detection of methane at room temperature, *Sens. Actuators B Chem.* 132 (2008) 155–158. doi:10.1016/j.snb.2008.01.034.
- [20] A. Biaggi-Labiosa, F. Solá, M. Lebrón-Colón, L.J. Evans, J.C. Xu, G. Hunter, G.M. Berger, J.M. González, A novel methane sensor based on porous SnO₂ nanorods: room temperature to high temperature detection, *Nanotechnology.* 23 (2012) 455501. doi:10.1088/0957-4484/23/45/455501.
- [21] Z. Wu, X. Chen, S. Zhu, Z. Zhou, Y. Yao, W. Quan, B. Liu, Room Temperature Methane Sensor Based on Graphene Nanosheets/Polyaniline Nanocomposite Thin Film, *IEEE Sens. J.* 13 (2013) 777–782. doi:10.1109/JSEN.2012.2227597.
- [22] E. Contes-de Jesus, D. Santiago, G. Casillas, A. Mayoral, C. Magen, M. José-Yacaman, J. Li, C.R. Cabrera, Platinum electrodeposition on unsupported single wall carbon nanotubes and its application as methane sensing material, *J. Electrochem. Soc.* 160 (2013) H98–H104.
- [23] A.K. Prasad, S. Amirthapandian, S. Dhara, S. Dash, N. Murali, A.K. Tyagi, Novel single phase vanadium dioxide nanostructured films for methane

- sensing near room temperature, *Sens. Actuators B Chem.* 191 (2014) 252–256. doi:10.1016/j.snb.2013.09.102.
- [24] B. Comert, N. Akin, M. Donmez, S. Saglam, S. Ozcelik, Titanium Dioxide Thin Films as Methane Gas Sensors, *IEEE Sens. J.* 16 (2016) 8890–8896. doi:10.1109/JSEN.2016.2619860.
- [25] A. Mosahebfard, H. Dehdashti Jahromi, M.H. Sheikhi, Highly Sensitive, Room Temperature Methane Gas Sensor Based on Lead Sulfide Colloidal Nanocrystals, *IEEE Sens. J.* 16 (2016) 4174–4179. doi:10.1109/JSEN.2016.2546966.
- [26] S. Nasresfahani, M.H. Sheikhi, M. Tohidi, A. Zarifkar, Methane gas detection at room temperature using Pd doped SnO₂/reduced graphene oxide nanocomposite, in: *Electr. Eng. ICEE 2016 24th Iran. Conf. On, IEEE, 2016*: pp. 1014–1018. <http://ieeexplore.ieee.org/abstract/document/7585669/> (accessed January 11, 2017).

Chapter 6

Density functional theory calculations

(DFT+U) analysis

6.1 Introduction

Section 5.2.1.2 states that the sensitivities of R(G) and R(A) were higher than that of the GO, as shown in Figure 5.4, because the residues of glucose and ascorbic acid contained oxygen functional groups to enlarge the space charge layer at the surface. As the sensitivity of R(G) was higher than R(A), we expected that the sensitivity of R(G)-SnO₂ would be higher than R(A)-SnO₂ in their heterostructures. However, we found that R(A)-SnO₂ had the highest increase of sensitivity, possibly due to the synergistic effect between DHA and SnO₂, as mentioned previously. To understand this effect more specifically, we performed DFT+U calculations on two systems: DHA-SnO₂ and Glucose-SnO₂. We did not consider borohydride and hydrazine systems in our calculations because the residues of borohydride and hydrazine after the reduction of the GO did not contain oxygen functional groups. As DFT calculations are quite demanding, we simplified our systems to include only the reducing agent and SnO₂ while

excluding the RGO surface and gases for simplicity. It is believed that the RGO surface has more p-type character in R(G) than in R(A). Hence, R(G) should have a stronger p-n junction effect with SnO₂, which would induce higher sensitivity than R(A). However, the p-n junction effect in R(G)-SnO₂ was evidently outweighed by the synergistic effect between DHA and SnO₂ in R(A)-SnO₂, which induced higher sensitivity in the latter.

The (110) plane of SnO₂ is widely simulated in DFT calculations, as it is the most stable surface with the lowest energy [1,2]. We observed that the (110) plane signal was the strongest peak in the XRD spectrum, as shown in Figure 3.5 (b). The main features of the structure of SnO₂ in the (110) plane are illustrated in Figure 6.1. Bulk SnO₂ has the rutile structure, such that each Sn is six-fold coordinated with O and each O is three-fold coordinated with Sn. However, due to the dangling bonds at the surface, there are two different lattice sites of Sn: Sn_{6c} (six-fold coordinated) and Sn_{5c} (five-fold coordinated). There are also two lattice sites of oxygen, i.e., ‘bridging oxygen’ and ‘in-plane oxygen’. The two oxygen sites have different vacancy formation energies and electronic states [3]. The bridging oxygen is more unstable, so it has smaller vacancy formation energy than in-plane oxygen. The oxygen vacancy defects are important in the formation of

the n-type SnO_2 and also serve as high-energy active sites for gas sensing. The DFT calculations of our model showed that DHA and glucose were adsorbed at different sites on the SnO_2 surface, which had a significant effect on the sensing mechanism.

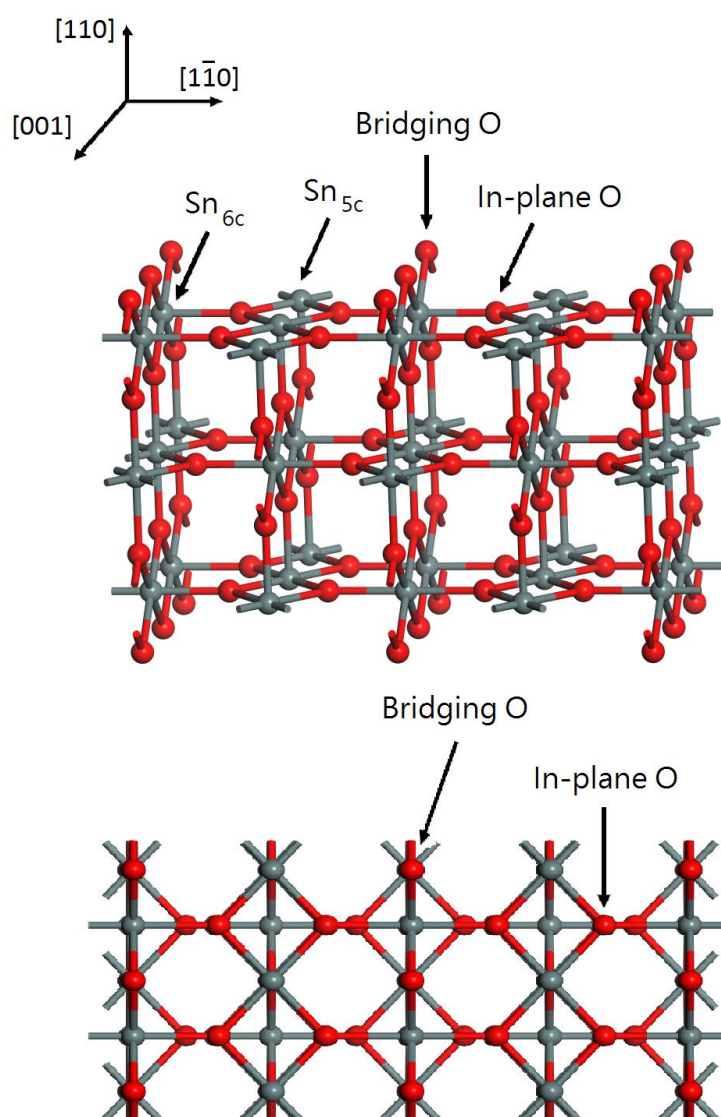


Figure 6.1 (110) plane of SnO_2 surface.

The CASTEP code was used to perform the DFT+U calculations [4] with the help of Dr. Bolong Huang. In this framework, we used the rotationally invariant (Anisimov-type) DFT+U functional [5] and self-consistently determined Hubbard U parameter for the pseudised O-2p orbitals, based on our new linear response method [6]. The self-consistently determined Hubbard U potential was applied with $U_p = 2.89$ eV, a consensus value [7–10] for many oxide materials. The PBE functional was chosen for the DFT+U calculations with a kinetic energy cutoff of 750 eV, and the valence electron states were expressed in a plane-wave basis set. The ensemble DFT (EDFT) method of Marzari et al. [11] was used for convergence. Reciprocal-space integration was performed using the special k-point $(\frac{1}{4}, \frac{1}{4}, 0)$ [12] with gamma-centre-off, which was self-consistently selected for total energy minimisation. With this special k-point, the total energy converged to less than 5.0×10^{-7} eV per atom. The Hellmann–Feynman forces on the atoms converged to less than 0.001 eV/Å. We used norm-conserving pseudopotentials generated using the OPIUM code in the Kleinman–Bylander projector form [13], and used the non-linear partial core correction [14] and a scalar relativistic averaging scheme [15] to average the spin–orbital coupling effect. For this treatment, we chose a similar non-linear core correction technique for correcting the valence–core charge density overlap in such elements. A

detailed discussion of this method was presented in previous work on a native point-defect study of CeO₂ [16,17]. The RRKJ method was chosen to optimise the pseudopotentials [18]. Prior to ab-initio predictions of the Hubbard U parameters for the orbitals, the geometries and lattice parameters of all of the SnO₂ (110) adsorption models were optimised using the PBE functional. This procedure reduced the computational cost and ensured the reliability of the Hubbard U value obtained by our self-consistent iterative calculations. We used this procedure before the Hubbard U determination, as DFT has been verified as reliable for the structural optimisation of compound solids with 4f or 5f orbitals [19], even with ultrasoft pseudopotentials. This may be due to the well-developed pseudopotential technique [16,17,19], as shown by the small difference between the DFT and DFT+U calculated lattice parameters [6,10,16,17,20]. Nevertheless, the U parameters had to be determined more carefully [6,10,16,17,20].

6.2 DHA-SnO₂ system

The structure of DHA is depicted in Figure 6.2, which shows that the three carbonyl groups in the five-membered ring could be easily delocalised when interacting with an electron donor [21]. The DFT calculations revealed two particularly stable models of the DHA-SnO₂ system: models 1 (dissociated

adsorption) and 2 (undissociated adsorption).

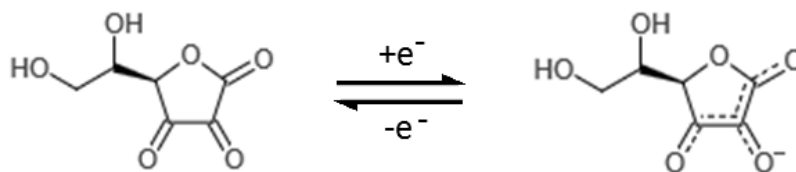


Figure 6.2 Dehydroascorbic acid (DHA) and delocalisation of the three carbonyl groups with an electron donor.

6.2.1 Model 1 (dissociated adsorption)

The HOMO and LUMO of DHA on the (110) plane of SnO₂ in model 1 are shown in Figure 6.3 (a) and (b), respectively. The formation energy E_{form} in the calculations was defined as $E_{\text{form}} = E_{\text{sys}} - \sum E_i$, where E_{sys} in model 1 is the energy of the whole system of DHA-SnO₂ and E_i comprises the isolated energies of DHA and SnO₂. The HOMO and LUMO of DHA were located at the five-membered ring of DHA, as shown in Figure 6.3 (a) and (b), respectively. The five-membered ring and the ‘tail’ of DHA were dissociated with a formation energy E_{form} of -14.25 eV. The negative E_{form} indicated that the dissociation of DHA was exothermic, such that the dissociated DHA was stably adsorbed on SnO₂. From the density of states (DOS) plot shown in Figure 6.3 (c), the HOMO and LUMO energies of -0.871 and 0.014 eV, respectively, were separated by a non-zero DOS

(the Fermi energy E_F is typically defined as 0); hence, there was no energy gap and hybridisation could occur easily, benefitting charge transfer. The five-membered ring was not adsorbed flat, but tilted from the plane, with carbonyl groups pointing downward towards the in-plane oxygen. This tilting might have been caused by the electron-donating property of the carbonyl groups, which were attracted towards the electron-withdrawing in-plane oxygen. The epoxy group in the ring was repelled upwards due to having the same electron-withdrawing nature as the in-plane oxygen. Other DFT calculations have reported that oxygen vacancies were mostly formed at the bridging oxygen sites rather than the in-plane oxygen sites [3], in which case the dissociated DHA would not block the formation of these vacancy sites for gas adsorption. The band gap energy of 1.951 eV, as shown in Figure 6.3 (c), was calculated using the second-lowest unoccupied energy level.

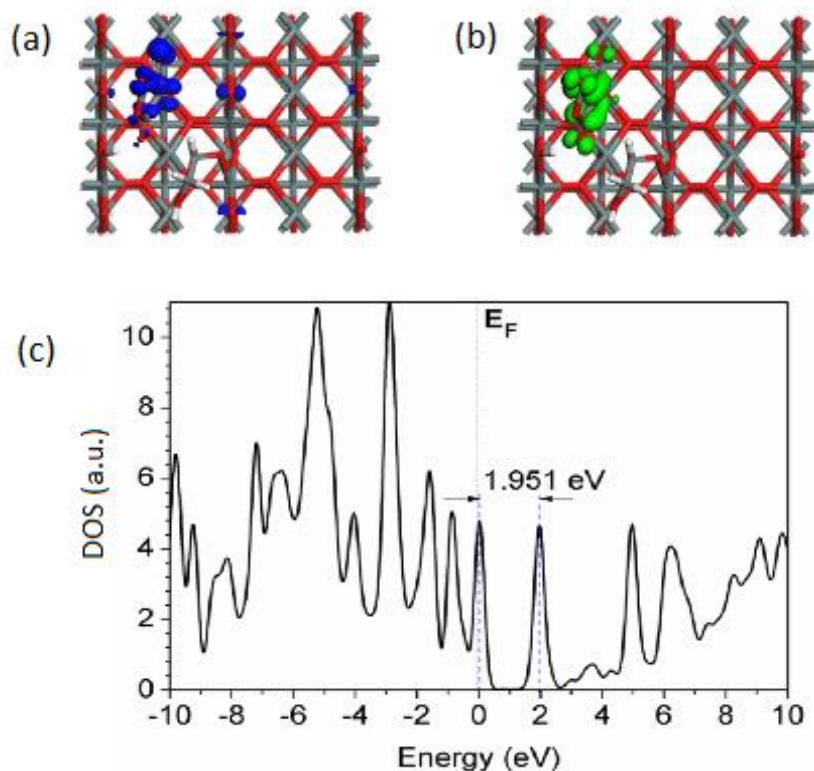


Figure 6.3 (a) HOMO (blue), (b) LUMO (green) and (c) DOS plot of DHA in model 1 (dissociated adsorption).

6.2.2 Model 2 (undissociated adsorption)

Model 2, where no dissociation occurred, was determined as the most stable form of DHA on SnO₂. The HOMO and LUMO were again located at the five-membered ring of DHA, as shown in Figure 6.4 (a) and (b), respectively. The formation energy E_{form} was determined as -12.87 eV, slightly less negative than that of model 1 (-14.25 eV). The negative E_{form} indicated that adsorption was again exothermic and favourable. Based on the DOS plot shown in Figure 6.4 (c),

the HOMO (-0.667 eV) and LUMO (0.595 eV) were separated by a small band gap of 1.262 eV. Hence, hybridisation occurred easily for this narrow band gap at room temperature, benefitting charge transfer. The lower band gap energy for DHA in this model could have been caused by the delocalisation of the three carbonyl groups, as shown in Figure 6.2. However, the DHA in model 2 was adsorbed flat on the SnO_2 surface, so that the electron-donating carbonyl groups could interact with the gas better than the downward-pointing carbonyl groups in model 1. Similarly, the adsorption position of DHA in model 2 was at the centre of the in-plane oxygen site, which would not block the bridging oxygen from forming vacancy defects, as observed in model 1. Hence, we attributed the synergistic effect between DHA and SnO_2 to the increased charge transfer from the delocalisation of the three carbonyl groups in the five-membered ring of DHA. As the electron-withdrawing in-plane oxygens were abundant on the SnO_2 surface, they induced greater charge transfer from the carbonyl groups in DHA when interacting with the reducing gas (methane). Delocalisation and charge transfer were not observed for the Glucose- SnO_2 system, which resulted in a lower sensitivity, as discussed in the next section.

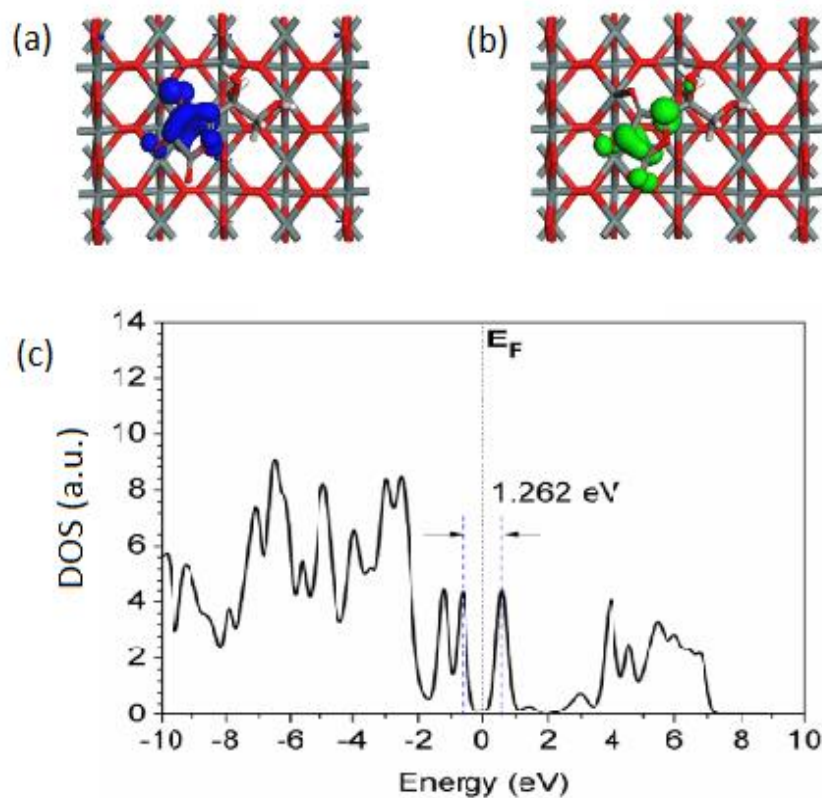


Figure 6.4 (a) HOMO (blue), (b) LUMO (green) and (c) DOS plot of DHA in model 2 (undissociated adsorption)

6.3 Glucose-SnO₂ system

We have shown that glucose was the weakest reducing agent among those tested, as indicated by the Raman, FTIR and XRD spectra in chapter 3. Hence, the residues of glucose mostly remained un-oxidised after the reduction of the GO, with only a small fraction oxidised to glucono delta-lactone. We performed DFT calculations for two models of the Glucose-SnO₂ system: models 3 (un-oxidised glucose-SnO₂) and 4 (glucono delta-lactone-SnO₂). The structures of d-glucose

(ring form) and glucono delta-lactone are depicted in Figure 6.5(a) and (b), respectively.

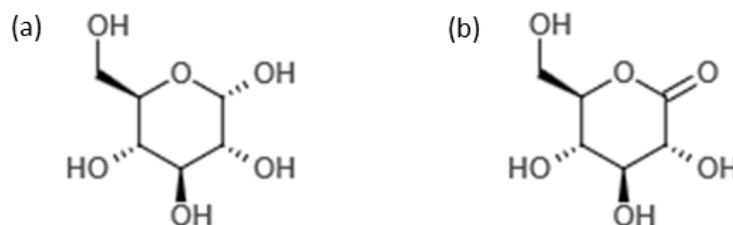


Figure 6.5 (a) D-glucose (ring form) and (b) glucono delta lactone

6.3.1 Model 3 (un-oxidised glucose-SnO₂)

Glucose and its derivative were modelled as the ring form in our DFT calculations, as this form was more stable than the chain form in non-aqueous states. The most stable adsorption state of D-glucose on SnO₂ was observed in model 3, with an E_{form} of -10.35 eV – less negative than that of the DHA system. The HOMO and LUMO were not close enough to allow hybridisation, as shown in Figure 6.6 (a) and (b), respectively. The band gap energy was determined as 5.410 eV, as shown in Figure 6.6 (c), confirming that the gap was too high for orbital hybridisation. (The small DOS around 2 eV was not identified as an effective LUMO state.) The less negative formation energy could have been caused by the adsorption site of glucose being atop the bridging oxygen rather than the in-plane oxygen. The attraction between glucose and bridging oxygen was evidently weaker than that

between DHA and in-plane oxygen. In addition, the glucose contained no electron-donating carbonyl group to share orbitals and electrons as in the case of DHA, again resulting in a higher band gap energy and decreased charge transfer. Furthermore, the position of the adsorption site of glucose atop the bridging oxygen blocked the formation of vacancy defects and thus lowered the gas sensitivity. Thus, both the unfavourable adsorption site and high band gap energy of glucose contributed to making the gas sensitivity lower than that of the DHA-SnO₂ system.

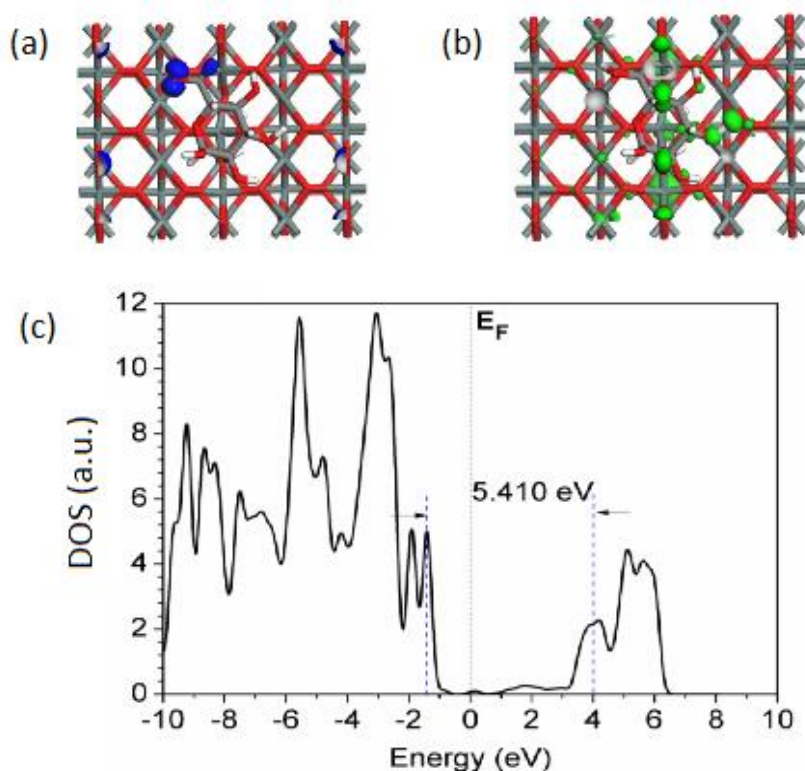


Figure 6.6 (a) HOMO (blue), (b) LUMO (green) and (c) DOS plot of glucose in model 3 (un-oxidised glucose-SnO₂).

6.3.2 Model 4 (glucono delta-lactone-SnO₂)

The HOMO and LUMO of model 4 (glucono delta-lactone- SnO₂) are shown in Figure 6.7 (a) and (b), respectively. The E_{form} of this system was determined as -9.46 eV, which was less negative than that of model 3 due to the electron-withdrawing epoxy group being atop the in-plane oxygen, leading to an unfavourable mutual repulsion. The HOMO and LUMO overlapped at the carbonyl group. The band gap energy was determined as 4.285 eV, as shown in Figure 6.7 (c), which was again too high for hybridisation at room temperature. Similar to the DHA-SnO₂ system, the adsorption site of glucono delta-lactone would not block the formation of vacancy defects at bridging oxygen sites, thus benefitting gas sensing. However, this model was of less practical relevance than model 3, as most of the glucose was not oxidised to glucono delta-lactone, as mentioned previously.

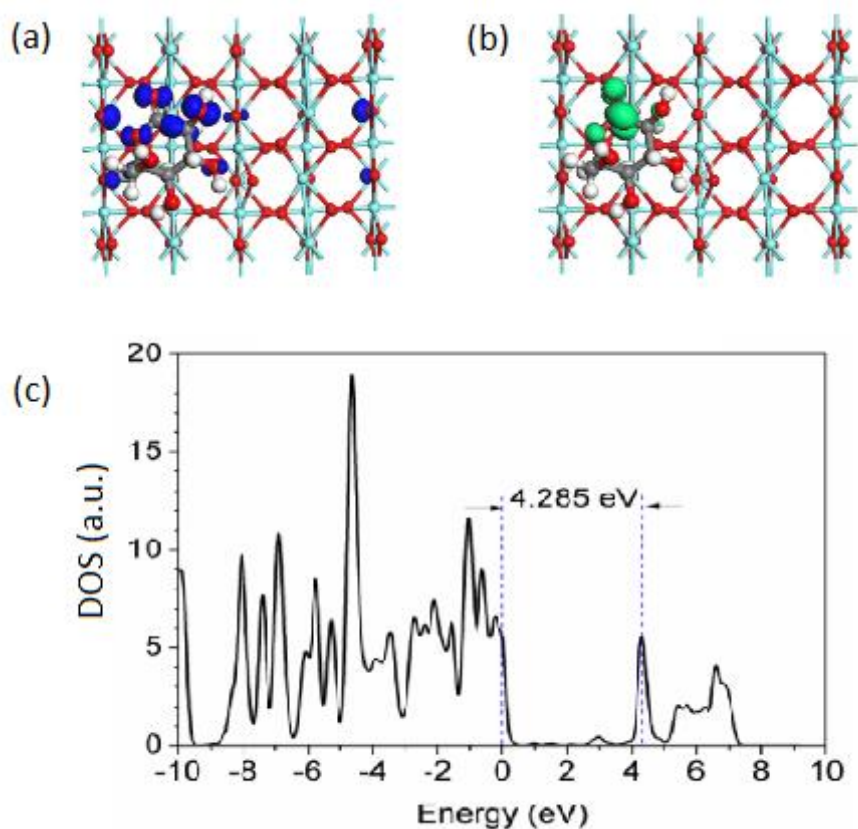


Figure 6.7 (a) HOMO (blue), (b) LUMO (green) and (c) DOS plot of glucono delta lactone in model 4 (glucono delta lactone-SnO₂).

6.4 Conclusion

In this chapter, the DFT+U calculations were applied in two systems such as DHA-SnO₂ system and glucose-SnO₂ system in order to study the higher sensitivity of R(A)-SnO₂ than that of R(G)-SnO₂. In DHA-SnO₂ system, model 1 (dissociated adsorption) was found to have the lowest formation energy of -14.25 eV with the dissociation of the five membered ring and the 'tail' of DHA. The

HOMO and LUMO of DHA were located at the five-membered ring of DHA which are close to having hybridization. The locations of HOMO and LUMO were atop the in-plane oxygen of SnO₂ surface which would not block the oxygen vacancy formation of SnO₂ at bridging oxygen sites. The DOS plot also show that the HOMO and LUMO were separated by a non-zero DOS indicating there was no energy gap and hybridisation could occur easily, benefitting charge transfer.

In model 2 (undissociated adsorption), it was found to be the most stable configurations in undissociated adsorption of DHA on SnO₂ surface with formation energy of -12.87 eV. The HOMO and LUMO were located in the five membered ring of DHA which are close to have hybridization. The band gap energy of 1.262 eV is small to allow hybridisation at room temperature, benefitting charge transfer. Similarly, the adsorption position of DHA in model 2 was atop the in-plane oxygen site which would not block the bridging oxygen from forming vacancy defects

In glucose- SnO₂ system, models 3 (un-oxidised glucose-SnO₂) and 4 (glucono delta-lactone-SnO₂) were studied with most stable configurations among. However, the effect of model 4 (glucono delta-lactone-SnO₂) was far less

significant than that of model 3 as most glucose was not oxidised to glucono delta-lactone due to its low reducing power. In models 3 (un-oxidised glucose-SnO₂), the formation energy was found to be -10.35 eV. However, the HOMO and LUMO were not close enough to allow hybridisation. In addition, the band gap energy was found to be 5.410 eV which is too high for hybridisation at room temperature. While the adsorption site of glucose was directly atop the bridging oxygen on SnO₂ which would block the formation of oxygen vacancies. Hence it was concluded that the better sensitivity of R(A)-SnO₂ than that of R(G)-SnO₂ was due to greater charge transfer in DHA-SnO₂ system and the more favourable adsorption site atop the in-plane oxygen rather than bridging oxygen.

References:

- [1] V. Lantto, T.T. Rantala, T.S. Rantala, Atomistic understanding of semiconductor gas sensors, *J. Eur. Ceram. Soc.* 21 (2001) 1961–1965.
- [2] J. Oviedo, M.J. Gillan, Energetics and structure of stoichiometric SnO₂ surfaces studied by first-principles calculations, *Surf. Sci.* 463 (2000) 93–101.
- [3] J. Oviedo, M.J. Gillan, The energetics and structure of oxygen vacancies on the SnO₂ (110) surface, *Surf. Sci.* 467 (2000) 35–48.
- [4] S.J. Clark, M.D. Segall, C.J. Pickard, P.J. Hasnip, M.I. Probert, K. Refson, M.C. Payne, First principles methods using CASTEP, *Z. Für Krist.-Cryst. Mater.* 220 (2005) 567–570.
- [5] V.I. Anisimov, F. Aryasetiawan, A.I. Lichtenstein, First-principles calculations of the electronic structure and spectra of strongly correlated systems: the LDA+U method, *J. Phys. Condens. Matter.* 9 (1997) 767.
- [6] B. Huang, 4f fine-structure levels as the dominant error in the electronic structures of binary lanthanide oxides, *J. Comput. Chem.* 37 (2016) 825–835.
- [7] S. Lany, A. Zunger, Polaronic hole localization and multiple hole binding of acceptors in oxide wide-gap semiconductors, *Phys. Rev. B.* 80 (2009) 085202.

-
- [8] S. Lany, A. Zunger, Generalized Koopmans density functional calculations reveal the deep acceptor state of N O in ZnO, *Phys. Rev. B.* 81 (2010) 205209.
- [9] B.J. Morgan, G.W. Watson, Intrinsic n-type defect formation in TiO₂: a comparison of rutile and anatase from GGA+ U calculations, *J. Phys. Chem. C.* 114 (2010) 2321–2328.
- [10] P.R. Keating, D.O. Scanlon, B.J. Morgan, N.M. Galea, G.W. Watson, Analysis of intrinsic defects in CeO₂ using a Koopmans-like GGA+ U approach, *J. Phys. Chem. C.* 116 (2012) 2443–2452.
- [11] N. Marzari, D. Vanderbilt, M.C. Payne, Ensemble density-functional theory for ab initio molecular dynamics of metals and finite-temperature insulators, *Phys. Rev. Lett.* 79 (1997) 1337.
- [12] M.I.J. Probert, M.C. Payne, Improving the convergence of defect calculations in supercells: An ab initio study of the neutral silicon vacancy, *Phys. Rev. B.* 67 (2003) 075204.
- [13] L. Kleinman, D.M. Bylander, Efficacious form for model pseudopotentials, *Phys. Rev. Lett.* 48 (1982) 1425.
- [14] S.G. Louie, S. Froyen, M.L. Cohen, Nonlinear ionic pseudopotentials in spin-density-functional calculations, *Phys. Rev. B.* 26 (1982) 1738.

-
- [15] I. Grinberg, N.J. Ramer, A.M. Rappe, Transferable relativistic dirac-slater pseudopotentials, *Phys. Rev. B.* 62 (2000) 2311.
- [16] B. Huang, R. Gillen, J. Robertson, Study of CeO₂ and its native defects by density functional theory with repulsive potential, *J. Phys. Chem. C.* 118 (2014) 24248–24256.
- [17] B. Huang, Superiority of DFT+ U with non-linear core correction for open-shell binary rare-earth metal oxides: a case study of native point defects in cerium oxides, *Philos. Mag.* 94 (2014) 3052–3071.
- [18] A.M. Rappe, K.M. Rabe, E. Kaxiras, J.D. Joannopoulos, Optimized pseudopotentials, *Phys. Rev. B.* 41 (1990) 1227.
- [19] C.J. Pickard, B. Winkler, R.K. Chen, M.C. Payne, M.H. Lee, J.S. Lin, J.A. White, V. Milman, D. Vanderbilt, Structural properties of lanthanide and actinide compounds within the plane wave pseudopotential approach, *Phys. Rev. Lett.* 85 (2000) 5122.
- [20] T. Zacherle, A. Schrieffer, R.A. De Souza, M. Martin, Ab initio analysis of the defect structure of ceria, *Phys. Rev. B.* 87 (2013) 134104.
- [21] J.R. Juhasz, L.F. Pisterzi, D.M. Gasparro, D.R. Almeida, I.G. Csizmadia, The effects of conformation on the acidity of ascorbic acid: a density functional study, *J. Mol. Struct. THEOCHEM.* 666 (2003) 401–407.

Chapter 7

Conclusions

Two types of methane gas sensors based on graphene related materials were developed by drop-dyeing and electrospinning methods. The sensors from each type were characterized and tested against methane gas for different concentrations. The sensing mechanisms for each type sensor were also explained. In the course of the study, several major conclusions have been drawn which made significant contributions to the relevant scientific areas. The major findings obtained from the experiments and simulation calculations are summarized as follows:

7.1 Methane gas sensor from drop-drying method

It was found that the degrees of reduction of the RGO were in ascending order of R(G), R(B), R(A) and R(H). The gas sensitivities of the homostructures were in ascending order of R(H), R(B), R(A), GO and R(G). The gas sensitivities of R(G) and R(A) were higher than those of R(B) and R(H) due to the residues of

glucose/glucono delta-lactone and DHA, respectively, on the RGO surface, which enlarged the space charge layer and thus improved the response.

The resistances of all the heterostructures with SnO₂ increased due to p-n junction effect. The sensitivities of the heterostructures were in ascending order of R(H)-SnO₂, R(B)-SnO₂, GO-SnO₂, R(G)-SnO₂ and R(A)-SnO₂. The highest sensitivity of R(A)-SnO₂ was found to be 76% at 10000 ppm methane concentration. The sensitivity of this sensor was not saturated and increased up to 241% at 80000 ppm.

The sensitivity of R(A)-SnO₂ was higher than that of R(G)-SnO₂ due to the synergistic effect between DHA and SnO₂, which induced greater charge transfer via orbital hybridisation at the carbonyl groups, and due to the more favourable adsorption site atop the in-plane oxygen. The fabrication method and sensing mechanisms of the highest sensitivity were superior to most of the current room-temperature methane-sensing technologies, with a higher sensitivity, a wider sensing range, a lower fabrication cost and a lower environmental impact. Moreover, the methane gas sensor by drop-drying method is facile, cheap and easily accessible in manufacturing which is much more convenient in mass

production than most other existing or potential commercial gas sensors in market and in research which require complicated and expensive methods.

7.2 Methane gas sensor from electrospinning method

The pure PVA nanofiber was found to have uniform, smooth, beadless structure with the smallest fiber diameter of 218 nm at 5 wt% PVA concentration in the precursor solution.

The resistances of the composite nanofiber of PVA/SnO₂/GO were successfully decreased by increasing carbonization temperature and GO content while retaining high sensitivity towards methane measured at room temperature. Sensitivity towards methane of 10000 ppm was determined to increase to the maximum value of 60.5% at carbonization temperature of 550 °C with GO content of 5 wt% (N3) with respect to PVA in precursor solution.

The sensitivities of the composite nanofiber of N0 without GO content was determined the lowest which could be due to the thin-skinned layer of amorphous carbon which cover the surface of the core-shell nanofiber structure as the carbon

skin layer had shielded SnO₂ from contacting with gases for interaction and also minimized the p-n junction effect by decreasing the contact boundary between the p-typed amorphous carbon and the n-typed SnO₂.

The addition of GO in the composite nanofiber completely changed the core-shell structure in N0 to the porous structures in N1 to N4. The porous nanofiber structure could benefit gaseous interaction by increasing the p-n junction effect and decreasing the shielding effect from the amorphous carbon layer. Sensitivity of N3 with GO content of 5 wt% was found to have the highest sensitivity of 60.5% at carbonization temperature of 550°C towards methane of 1%. The gas sensor was not saturated at high concentration of methane from 6000-10000 ppm which is useful in application of high concentration environment.

7.3 Future works and improvements

Although room temperature graphene based gas sensors have been developed and their sensing properties towards methane were investigated in the course of this study, there are still lots of rooms to improve such as the understanding of sensing mechanisms, sensitivity with other additives, different fabrication methods and

selectivity for different gases.

7.3.1 Improvement of understanding the sensing mechanisms

In GO or RGO, there are oxygen functional groups such as epoxy group (C-O-C), carboxylic group (COOH), hydroxyl group (C-OH) and carbonyl group (C=O) which reside on the surface. However, the understanding of the interactions of these oxygen functional groups with different gases is still in a preliminary stage. For example, the use of space charge layer or Schottky barrier concept in analogy with SnO₂ case to explain the change of resistance and sensitivity. However, the electron withdrawing properties of the epoxy, carboxylic and hydroxyl groups as well as the electron donating property of carbonyl group, which are not studied in detail such as electron affinities for these groups. In addition, the effects on resistance and sensitivity of the locations of these groups such as inside or at the edges of the basal plane of GO or RGO are not investigated. For example, epoxy and hydroxyl groups could be formed inside or at the edges of the basal plane but carboxylic and carbonyl groups are only formed at the edges of the basal plane. Hence the difference of the locations of these functional groups would have different effects on resistance and sensitivity with gases.

In addition, the detailed mechanisms of the interaction of methane with these oxygen functional groups on RGO or oxygen vacancies on SnO₂ are not studied. The explanations of the current mechanisms are mostly based on the reducing gas property of methane which releases the bound electrons on surface back to core. However, whether there are dissociations of methane into any molecular ions or chemical bonding formations with the oxygen functional groups or the oxygen vacancies are still unknown during the gaseous interactions unless provided with simulation calculations. Indeed, the sensing mechanisms of methane interactions reported by other works are only proposed by assumption without solid theoretical proofs so the full understandings of these mechanisms are important in designing the sensing materials.

7.3.2 Improvement of sensitivity with other additives

There are basically three materials used in our gas sensor fabrication such as GO, SnO₂ and PVA. Indeed, there are many other materials such as Pt, Pd, ZnO, CuO, TiO₂ or In₂O₃ which are reported to increase sensitivities with SnO₂ to different gases by either catalytic effect or synergistic effect. Hence, there are still lots of rooms to develop better gas sensor with incorporation of these materials into

optimal content.

7.3.3 Improvement by using different fabrication methods

In our study, thick film and nanofiber of graphene based gas sensors were studied; however there are drawbacks in these morphologies. For example, drop drying method resulted in thick film production of the sensing composites which is not benefitting in transducing gaseous interaction to electrical signals. Indeed, gaseous interaction would change the electron density or electric field on surface which could impose effect in electrical conduction in bulk region. Hence, it is expected that sensing composites in thin film would has much higher the electric field effect in electrical conduction in bulk region than thick film as electric field change at surface would be attenuated for increasing film thickness. Therefore, thin-film fabrication techniques like sputtering, CVD, PVD or thermal evaporation would be advantageous in gas sensing.

In the case of our nanofiber morphology, it is no doubt that 1D nanofiber has very good surface-to volume ratio in gas sensing, however, most nanofiber requires high temperature to anneal or carbonize for stabilization and refining

processes which also thermally reduces all oxygen functional groups on GO surface and decreases sensitivity afterwards. Hence it is expected another fabrication techniques which do not require such high temperature such as 3 dimensional graphene oxide hydrogel from cryogenic drying so as to preserve all oxygen functional groups. On the other hand, the fabrication procedure could be altered a little bit to firstly electrospin SnO₂ nanofiber, followed by annealing and then treated with GO suspension later which could also preserve oxygen functional groups on GO. However, the pristine nanofiber morphology would be greatly altered by the multi-step synthesis.

7.3.4 Improvement of selectivity for different gases

In this study, only methane gas sensing properties were investigated. Indeed, for a thorough study of methane gas sensor in ambient environment, other reducing gases or oxidizing gases should be investigated in order to resolve their responses from methane. Furthermore, a multi-array gas sensor of different sensing materials should be developed to complement different responses to different gases.